Universidade de Santiago de Compostela

Departamento de Física de Partículas

PRODUCTION AND CHARACTERIZATION OF THE ^{7}H RESONANCE

Manuel Caamaño Fresco

Under the direction of

Dolores Cortina Gil and Hervé Savajols

June 2006

To whom it may concern
(John Cage, "Silence")

Contents

List of Figures

List of Tables

Chapter 1

Study of Neutron-Rich Light Nuclei

One of the main goals in nuclear physics is to understand how nuclei are constructed, and what holds the nucleons inside. Although much effort is being made to provide a complete model describing all known nuclear species, at present we have a fragmented vision of the whole picture, with different descriptions for different areas of the nuclear chart.

Understanding the force that holds nucleons inside a nucleus is an important step in the process of creating a general description. Because the interactions between nucleons create particular structures, the study of nuclear structure is a primary source of information about nuclear interactions. For many years it was only possible to study stable nuclei, which were the basis for the nuclear models developed.

Recent developments in radioactive beam production open new opportunities in this field. We can now use systematic measurements of nuclei far from stability to test the predictions of existing models. In fact, the study of these areas of the nuclear chart has revealed new structures, such as extended wave functions for neutrons and protons classified as halos [Tan85][Han87], with Borromean behaviour [Zhu93], or new types of radioactivity such as two-proton emission [Bla05], that are not present in stable species. The existing shell model does not describe these structures, and new theoretical approaches are needed to understand new nuclear properties, such as predicted shells mixing up and causing parity inversions [Tal60], or the inhibition or appearance of magic numbers [Gui84][Ots01].

Localization of proton and neutron drip lines may provide direct information about the strength of the interaction between nucleons. Identification and char-

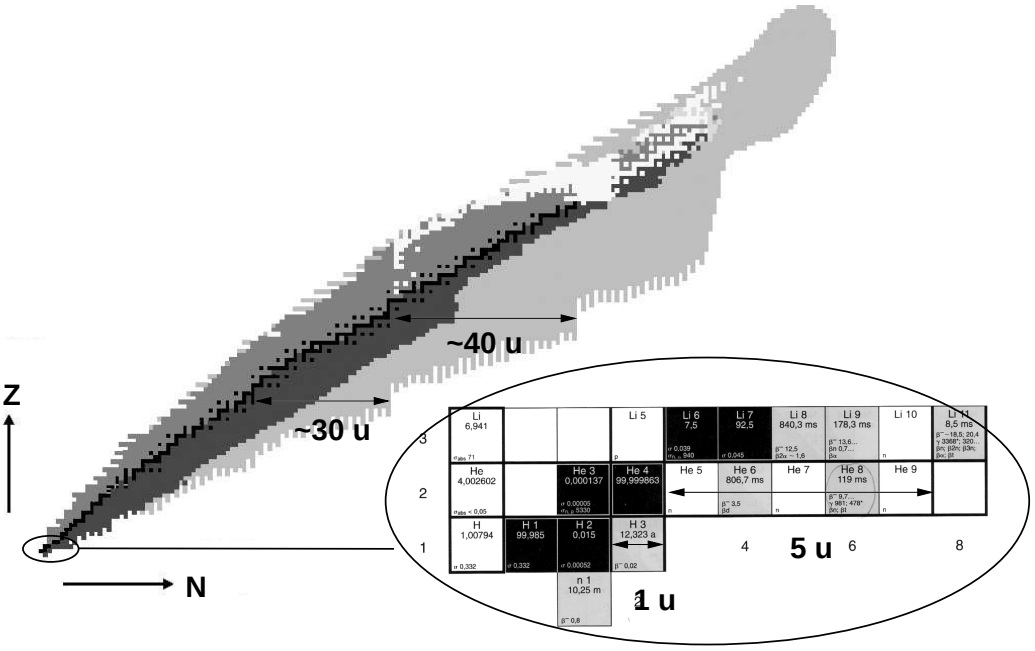

Figure 1.1: *Chart of the nuclides. Black squares represent the stable isotopes, dark-grey squares are the β^- unstable isotopes, grey squares are the β^+ unstable isotopes, white squares are those isotopes decaying by α emission, and light-grey stands for the expected region limited by the drip lines. Arrows mark the distance between the stable isotopes and the expected neutron drip line. We can see distances between 30-40 u of mass for middle-heavy isotopes. The ellipse zooms in on the region for very light isotopes, where the distance between stability and the drip line is reduced to a few mass units.*

acterization of resonant states beyond the drip lines is also a valuable source of information. With present technology, it is impossible to reach proton and/or neutron drip lines for medium-heavy isotopes (see Figure 1.1). However, the scenario changes for light nuclei, where the neutron drip line has already been reached up to Fluorine isotopes (Z=9)[Sak99]. The neutron drip line for Lithium (Z=3) is four nucleons away from the stable isotopes, the Helium (Z=2) isotopes reach the neutron drip line with five added nucleons, and the Hydrogen (Z=1) isotopes are separated from the drip line by only one neutron added to the last stable isotope.

Many experimental efforts have been made during the last decades to produce and study these exotic isotopes. Among the techniques used we can mention pick-up, transfer, or knock-out reactions, normally with inverse kinematics[1]. These experimental studies help to create adequate theoretical models for describing the

[1] where a relatively heavy projectile impinges on a light target.

properties of these extreme nuclear states.

In this work we focus mainly on the search and study of Hydrogen isotopes. These isotopes allow to perform the longest excursions beyond the drip line, representing the most exotic nuclei available. The search and study of Hydrogen resonance is one of the most stringent test for our knowledge about nuclei formation. In the next section we review the current state of experimental research and theoretical progress in this area, that connects directly with the motivations of our work.

1.1 The Quest of Heavy Hydrogen Isotopes: Historical Review and Present Status

This section is divided into two parts: the first describes theoretical approaches to understand the new properties of extremely neutron-rich light isotopes, and the second reviews experimental results[2].

1.1.1 Theoretical approaches

From the theoretical point of view, the case of light nuclei is particularly complex and interesting. Due to the number of nucleons involved, there are two general scenarios for these species: they can be seen as few-particle systems directly influenced by the nucleon-nucleon interaction or as many-body systems where inner structures dominate. Different approaches are used to describe of these nuclei. We can classify them in three groups: macroscopic, microscopic, and $ab-initio$ models.

The first attempt to describe these nuclei is to expand descriptions that have been proved useful in heavier isotopes. Macroscopic models work on the hypothesis of nuclei made of clusters of nucleons, considered, in general, without inner structure and punctual. Several cases of light nuclei are known to exhibit a cluster structure (^{6}He, ^{7}Be, etc.) and the arrangement of nucleons in each individual nucleus should be chosen taking into account its physical properties.

The main advantage of this approach is the relative simplicity of the systems. The problems arise with the description of the interactions between clusters, which may be unknown for some systems, difficulting the extraction of valuable predictions.

[2] an extensive review on the experimental studies of exotic nuclei can be found in references [Til92] and [Til02].

A general and obvious limitation of this approach is that not every nuclear system can be arranged in clusters.

An example of this is the application of the *transfer to the continuum method* to light unbound nuclei[Bla04]. In the case of nuclei that can be described as neutron-core systems,*spectroscopy in the continuum* allows to extract valuable information. However, these restrictions in its applications force this method to be useful as a tool for some nuclear systems, without possible extension to a general description of nuclear matter.

The evolution of the macroscopic view is the *microscopic* approach, where each individual nucleon inside the cluster is taken into account. The *cluster hypothesis* is normally done to simplify the treatment of systems with mass $A > 4$. The descriptions of these nuclei are based on a nucleon-nucleon interaction, which is in principle common to all nuclear systems. But this interaction is normally chosen among a collection of *effective* forces, depending on the model.

The description of the light nuclei under the microscopic approach is somewhat more realistic than with the macroscopic view, and allows to make predictions on the properties of these nuclei. The major problems concern again the necessity of using the cluster hypothesis, and the longer computing time needed for the calculations.

An example of the *microscopic cluster* approach can be found in reference [Des01] by P. Descouvemont and A. Kharbach, where the *generator coordinate method* is applied to the case of ^{5}H, and other light nuclei. The corresponding basis functions for the five-body Hamiltonian are defined in the three-cluster approximation: $\Phi_{\nu_1\nu_2\nu_3}(R_1, R_2, \alpha) = \mathscr{A}\phi_t^{\nu_1}\phi_n^{\nu_2}\phi_n^{\nu_3}$. The antisymmetrizer $\mathscr{A}$ operates on the corresponding wave functions, $\phi_t^{\nu_1}$, $\phi_n^{\nu_2}$, $\phi_n^{\nu_3}$, of the triton and neutrons with the ν_i spin projections. The wave functions are defined in the harmonic oscillator and centered on the generator coordinates R_1, R_2, and α, defined in Figure 1.2.

The system is then described as a linear combination of the basis states:

$$\Psi^{JM\pi} = \sum_{\nu_1\nu_2\nu_3} \int f^{J\pi}_{\nu_1\nu_2\nu_3}(R_1, R_2, \alpha) \times \Phi^{JM\pi}_{\nu_1\nu_2\nu_3}(R_1, R_2, \alpha) \mathrm{d}R_1 \mathrm{d}R_2 \mathrm{d}\alpha \qquad (1.1)$$

The solution is found in the generator function $f^{J\pi}$ which determines the contribution of each state of the basis depending on the Hamiltonian and the overlapping kernels in the Hill-Wheeler equation:

$$\sum_{\nu_1\nu_2\nu_3} \int f^{J\pi}_{\nu_1\nu_2\nu_3} \times \langle \Phi^{JM\pi}_{\nu'_1\nu'_2\nu'_3} | H - E | \Phi^{JM\pi}_{\nu_1\nu_2\nu_3} \rangle \mathrm{d}R_1 \mathrm{d}R_2 \mathrm{d}\alpha = 0 \qquad (1.2)$$

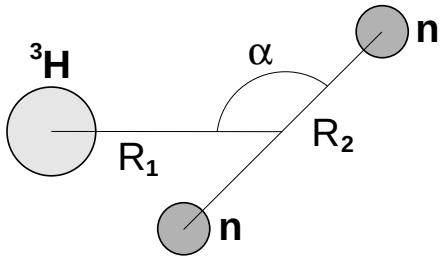

Figure 1.2: *Three-cluster structure arrangement for the ^5H system. R_1, R_2, and α are the generator coordinates.*

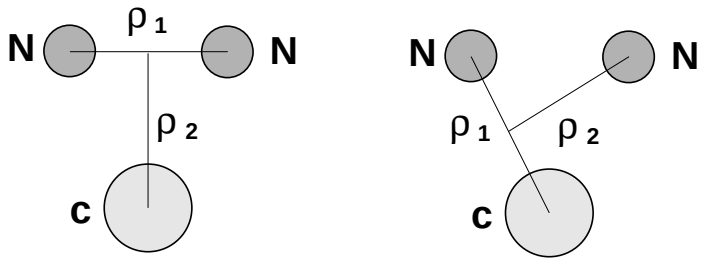

Figure 1.3: *The different Jacobi arrangements for a c+N+N three-cluster system are shown in the figure. The Jacobi coordinates are $\boldsymbol{\rho}_1$ and $\boldsymbol{\rho}_2$.*

Evaluation of the results of a microscopic model may depend on the particular nucleon-nucleon interaction. In this case Descouvemont and Kharbach performed the calculations for different descriptions of the nucleon-nucleon interaction[3], with results varying around 10 %. Finally, the predicted resonance energy for the ^{5}H is $E_R \approx 3$ MeV above the ^{3}H+2n threshold, with a neutron width of $\Gamma_0 \approx 1 - 4$ MeV.

A similar approach is the *microscopic multicluster model*, used for example in reference [Ara03] by K. Arai. In this work, different light isotopes, including the ^{5}H, are also described as cluster systems, but with a superposition of different configurations (see Figure 1.3).

[3]specifically the Minnesota [Tho77], a zero-range spin orbit [Bay81], and the Mertelmeier and Hofmann [Mer86] forces.

The wave function is expressed as a linear combination of all possible arrangements, obtained by applying the antisymmetrization operator $\mathscr{A}$ to the product of the cluster intrinsic wave functions, Φ^{μ}_{S},as:

$$\Psi^{JM\pi} = \sum_{\lambda} C_{\lambda} \mathscr{A}\{[\Phi^{\mu}_{S}[\Gamma_{l_1}(\nu_{k_1}, \boldsymbol{\rho}_1)...\Gamma_{l_{N-1}}(\nu_{k_{N-1}}, \boldsymbol{\rho}_{N-1})]_L]_{JM}\} \tag{1.3}$$

λ is a summary of the set of quantum numbers defining the state, $\{\mu, S, l_i, L, K\}$, with μ labelling the Jacobi arrangement, S the total spin, and l_i the angular momenta on the respective Jacobi coordinates $\boldsymbol{\rho}_i$, $K = (k_1, ..., k_{N-1})$ is the corresponding set of the basis. The size of the tempered Gaussian Γ_i is controlled by the parameter ν_{k_i}. The weighting coefficients C_{λ} are obtained by solving the A-nucleon Schrödinger equation[4]. The predictions for the ^{5}H case are a resonance energy of $E_R = 1.59$ MeV and a width of $\Gamma_0 = 2.48$ MeV.

Some of the recently developed approaches are *microscopic* $ab - initio$ treatments. In these models the nuclei is again described as a collection of individual nucleons, but there is no previous assumptions on cluster arrangement. The interaction between the nucleons is then more realistic. The properties of the system are extracted, as usual, from the solutions of the associated Schrödinger equation.

The $ab - initio$ descriptions are then more realistic than the previous ones, but they are not free of problems. The main disadvantage is their difficulty to predict the existence of resonances. This problem is not inherent to the $ab-inition$ descriptions and its expected to be overcome in future developments of these models. Another problem is the even longer computing time needed for extracting the solutions, which nowadays limits the application to masses with $A \leq 12$.

The *antisymmetrized molecular dynamics* (AMD) approach, combined with the *generator coordinate method* and a *stochastical variational* method by S. Aoyama and N. Itagaki in reference [Aoy04] is an example of an $ab - initio$ model. In this case the wave function of the system is antisymmetrized over the A constituent nucleons as:

$$\Psi = \mathscr{A}[(\psi_1\chi_1)(\psi_2\chi_2)...(\psi_A\chi_A)] \tag{1.4}$$

The wave function corresponding to each nucleon, $\psi_i\chi_i$, is built with the spin-isospin eigenfunction, χ_i, and a Gaussian, ψ_i, expressed as:

[4]again, the choice of the nucleon-nucleon interaction is important. In this work, Arai used versions of Minnesota and Reichstein-Tang [Rei70] forces.

$$\psi_i = \left(\frac{2\nu}{\pi}\right)^{\frac{3}{4}} \exp[-\nu(\boldsymbol{r} - \boldsymbol{z}_i/\sqrt{\nu})^2 + \boldsymbol{z}_i^2/2] \tag{1.5}$$

where $\boldsymbol{z}_i$ is a randomly generated complex parameter, whose imaginary part is optimized over selected states by using the *frictional cooling method*[Ono92] in AMD. The total wave function is built upon the basis formed with those Ψ_k distributions, generated with the *generator coordinate method*. Again, the solution is obtained by diagonalizing the Hamiltonian matrix[5], with results expected to converge for large numbers of trial basis functions. Aoyama and Itagaki applied the method to different Hydrogen isotopes, with binding energy predictions of $B \sim -6.5$ MeV for the ^{5}H, and $B \sim -1.5$ MeV for the ^{7}H.

Another $ab-initio$ approach to solving difficulties that arise with the few-body problem is to introduce hyperspherical coordinates, and to build a base where the wave function of the system is expanded on the basis of a shell model description [Tim04]. Basically, in the *hyperspherical functions method* ($HSFM$), the wave function of the A-body system is described using a single vector $\boldsymbol{\rho}$ which contains the $3A$-3 components of the A-1 Jacobi coordinates, as a function of the positions of each nucleon $\mathbf{r}_i$: $\boldsymbol{\xi}_i = \sqrt{i/(i+1)}(\Sigma_{j=1}^{i}\mathbf{r}_j - \mathbf{r}_{i+1})i^{-1}$. A hyperangular momentum K quantum number can be defined by applying multidimensional Laplacian. The radial and spherical contributions are then separated, and the solution of the Hamiltonian based on a harmonic oscillator can be obtained by the convergence of an expansion of the hyperspherical basis. However, this convergence is only obtained for $A < 5$. For heavier systems, the number of hyperspherical harmonics becomes very large [6] and the conclusions are extracted by extrapolating the behaviour of K. In the case of ^{7}H, Timofeyuk suggests a resonance at about 3 MeV above the ^{3}H+4n threshold[7].

Finally, we can mention the work from Navrátil *et al.* (see for example [Nav02]) based on *no core shell model* ($NCSM$) calculations. The use of an effective nucleon-nucleon interaction extracted from the solutions of Hamiltonians in two-body, three-body, (etc.) center of mass frame, allows to extend the calculation to a more realistic description of the interaction. The solution of the general Hamiltonian is expanded in serials of N, the many-body harmonic-oscillator excitation energy, up to a fixed N_{max}. Again, the solution corresponds to the convergence of the serial when $N_{max} \to \infty$. Up to now there is no application of this approach to the ^{7}H

[5] specifically, the authors used the Volkov potential [Vol65] for the nucleon-nucleon interaction, and the G3RS potential [Yam79] for the spin-orbit term

[6] modifications of the $HSFM$ intended to reach the convergence for heavier systems can be found in references [Bar03].

[7] in a previous reference [Tim02], the ^{7}H energy resonance was estimated around 6 MeV above the ^{3}H+4n threshold for the last calculated momentum K. However, the extrapolation for convergence in K led to a binding energy of -7.61 MeV, which is much closer to the result of the present work.

system, but the results concerning other light systems, as Helium or Lithium, seem very promising.

The different approaches mentioned are but a brief overview of the theoretical possibilities for describing these few-body systems, and by no means exhaustive. Common to all of them is the difficulty of choosing an appropriate description of the nucleon-nucleon interaction, which is for the most part independent of the model itself, and it may lead to different results. Concerning the specific case of ^{7}H, its nature as an unbound system makes difficult the description of its properties in the most of the models. In addition, there is no information about structure inside ^{7}H[8], which is esential for a good description in microscopic cluster models. Experimental studies of these nuclei should help to determine which descriptions are more accurate.

1.1.2 Experimental results

In this section we focus on the experimental results of the search for Hydrogen isotopes beyond the drip line performed during the last 40 years[9]. During this period the number of known Hydrogen resonances increased with experimental observations of ^{4}H, ^{5}H, and ^{6}H. Recent experimental evidences [Kor03] and the publication of theoretical predictions [Tim04][Aoy04] concerning the existence of a ^{7}H resonance have also increased interest in searching for this heavy isotope.

The search for heavy hydrogen isotopes has historically created controversy due to differing experimental results. The long-standing problem of the case of ^{4}H is no exception. Earliest results showed energies relative to the ^{3}H+n threshold ranging from 1.7 MeV [Sto66][10] up to 8 MeV [Mey79]. Further experimental studies were performed in order to shed light on this numbers. ^{4}H was also studied by investigating isobar analog states of ^{4}Li in p+^{3}He scattering [Til92]. Tilley *et al.* found two states in ^{4}H with 3.2 and 3.5 MeV, after R-matrix transformations between the two systems. There are still discrepancies about the characteristics of ^{4}H, but they seem to converge somehow. Different experiments in GSI [Mei03b] and Dubna [Sid04], again resulted in different values for the resonance energy and width (see Figure 1.4). The Dubna experiment was based on two transfer reactions to produce the resonance: ^{2}H(^{3}H,p)^{4}H and ^{3}H(^{3}H,^{2}H)^{4}H. The results from both reactions are consistent and closer to those from the ^{4}Li isobaric analog state study. The resonance energy is around 3 MeV and its width is larger than 4 MeV. The GSI

[8] for example Aoyama and Itagaki[Aoy04] propose two situations when a proton is added in a six neutron system: ^{3}H+n+n+n+n or p+^{2}n+^{2}n+^{2}n.

[9] see for example [Ade67] where hints of the existence of Hydrogen resonances were indirectly found on secondary channels in the study of Beryllium isotopes.

[10] as cited by Korhseninnikov in [Kor05].

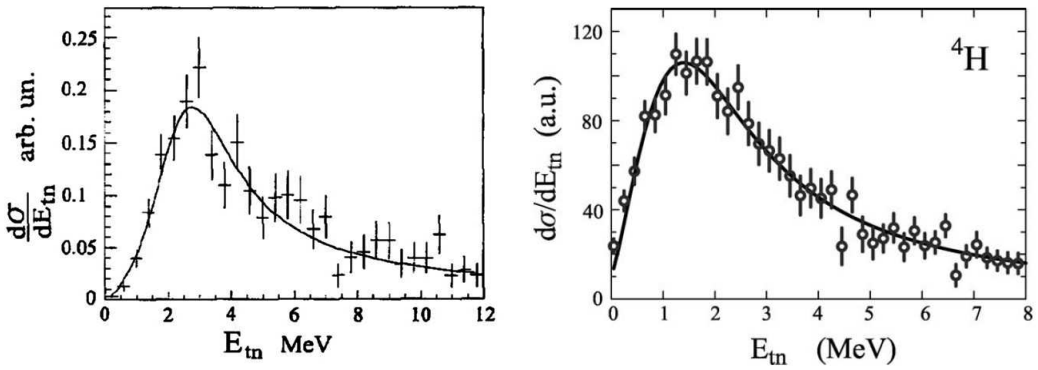

Figure 1.4: *^{3}H+n excitation energy spectrum calculated in two different experiments. Left panel corresponds to $^{2}H(^{3}H,p)^{4}H$ transfer reaction from reference [Sid04]. On the right panel is the resulting excitation energy from the knockout reaction $^{12}C(^{6}He,^{4}H+n+p)^{12}C$ in reference [Mei03b].*

experiment studied the ^{4}H state with proton knockout of a 240 MeV/u ^{6}He with a Carbon target. The ^{4}H state appears at about 1.5 MeV over the ^{3}H+n threshold, which clearly differs from previous results. Meister *et al.* explain the differences as the interference between potential and resonant scattering, which shifts the energy distribution and enforces a dependence on the reaction mechanism. Their final result for the ^{4}H resonance energy is 2.7 MeV with a resonance width of 3.3 MeV, which is closer to the previous results.

Another unclear scenario is that of the ^{5}H research, with different results arising from the different experimental approaches to this resonance. In this case, whether the resonance actually exists was controversial until recently, because of the many unsuccessful experiments in searching for the state. In the first attempt to characterize the resonance in the late 1960's [You68], Young *et al.* did not exclude the possibility of a phase space effect to explain the peak at 1.8 MeV over the ^{3}H+2n threshold. In later experiments similar difficulties were encountered in separating the ^{5}H production from other reaction channels, phase space effects, etc (see Figure 1.5 for a collection of results). The most recent experimental attempts range from transfer reactions to π^{-} absorption and their results can be divided into three groups[11]: experiments arguing that the ^{5}H ground state is around 2 MeV above the ^{3}H+2n threshold [Kor01][Gol03][Ste04][Gol05], a single measurement claiming the ground state to be at $\sim$3 MeV [Mei03a], and, finally, the description of the ^{5}H state as a broad structure with a center of gravity around 5 MeV [Gor03]. Not only is the position of the resonance unclear, but the width is also difficult to determine within the different approaches. The ^{5}H state is described as a broad resonance

[11] following the review of reference [Kor05].

of 5-6 MeV in some cases [Mei03a][Gor03], as a narrow resonance of around 1.5 MeV in others [Kor01][Ste04][Gol05], and, surprisingly, even as smaller than 0.5 MeV[Gol03][12], which is difficult to reconcile with theoretical predictions (see for example reference [Des01]). These differing results seem to be related to the different reaction mechanisms in the experimental studies. The use of transfer reactions leads to narrow low resonances as in [Kor01][Ste04] or [Gol05], while other techniques such as knockout [Mei03a], or π^- absorption [Gor03] find broader distributions at higher resonance energies. Among the reasons for these discrepancies are the difficulty of reconstructing the reactions, separating the interesting reaction channel from other possible ones, and properly describing the phase space contributions, which is especially complicated when interactions between the reaction products, such as n-n interaction, must be taken into account. More experimental effort is need to clarify the results.

The history of the ^{6}H resonance is somehow clearer than that of ^{5}H. Its existence was reported in the middle 1980's, even before the question about the existence of ^{5}H was resolved, with the ^{7}Li(^{7}Li,^{8}B)^{6}H reaction at 82 MeV [Ale84], and with ^{9}Be(^{11}B,^{14}O)^{6}H at 88 MeV [Bel86][13]. The extracted values for the energy and width of the resonance were $E_R = 2.7$ MeV and $\Gamma = 1.8$ MeV in [Ale84], and $E_R = 2.6$ MeV and $\Gamma = 1.3$ MeV in [Bel86], resulting in good agreement between both studies, with cross sections of the order of tenths of nb/sr. However, the reporting of ^{6}H before ^{5}H, along with apparent contradictions with the previous shell-model calculations led to a latter attempt to clarify the situation with the π double charge exchange (DCX) reaction ^{6}Li(π^-,π^+)X [Par90]. The authors chose the π DCX process due to its success in populating neutron-rich nuclei. In the end they reported no evidence for the formation of the ^{6}H resonance, which cast doubts upon the previous results. See Figure 1.6 for comparison of results from [Bel86] and [Par90].

These findings inspired theoretical works to explain the existence of these extremely unbalanced isotopes. A major interest at present is to find the heaviest of the hydrogen resonances. Recent theoretical works, along with experimental indications, point to the ^{7}H resonance as the heaviest Hydrogen system. The results from ^{5}H compared with He isotopes suggest that ^{7}H may exist as an unstable state near the ^{3}H+4n threshold, being the heaviest of the hydrogen chain, and the nuclear state with the most unbalanced neutron-proton ratio $N/Z = 6$. In reference [Kor05] ^{7}H is also predicted as a very narrow state, since the ^{7}H may decay into a unique five particle ^{3}H+n+n+n+n channel. The ^{7}H resonance was searched for but not characterized, although evidences of its existence had already been found.

[12] with the addition of another narrow state of ^{5}H at 2.7 MeV also reported in [Sid03], that disappears in the following studies of the same reaction at small center of mass angle [Gol04b] and [Gol05], perhaps transformed in a mixture of different ^{5}H states.

[13] in the same work searching for ^{4}H and ^{5}H was also performed. Remarkably enough, no evidence of ^{5}H levels was found.

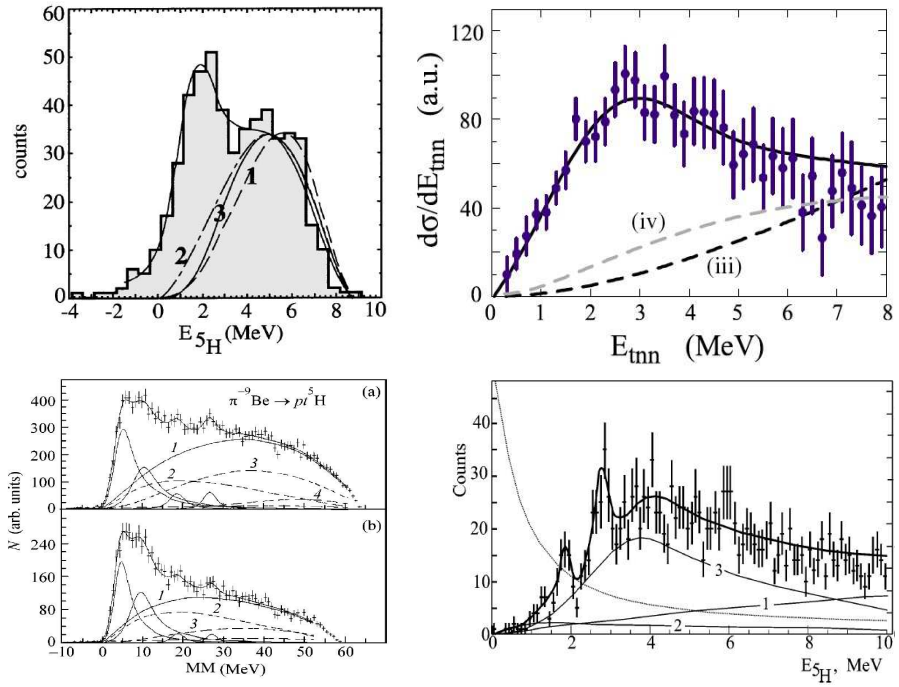

Figure 1.5: *Different experimental studies on ^5H. Left upper panel corresponds to the p(^{6}He,p p ^3H) reaction from reference [Kor01] with $E_R = 1.7$ MeV and $\Gamma = 1.9$ MeV. Right upper panel shows the t+n+n spectrum for the knockout reaction $^6He+^{12}C$ from [Mei03a] resulting in $E_R \simeq 3$ MeV and $FWHM \simeq 6$ MeV. The left bottom panels are the missing mass spectra for the π^- absorption reaction $^9Be(\pi^-,pt)^5H$, with different conditions on the momentum of undetected residual, from reference [Gor03]. The ^5H parametrization resulted in $E_R = 5.5$ MeV and $\Gamma = 5.4$ MeV. Finally the right bottom panel shows the ^5H energy spectrum from $^3H(^3H,p\ ^3H\ n)$, as measured in reference [Gol03]. The characteristics of the lower peak, identified as the ^5H ground state, are $E_R = 1.8$ MeV and $\Gamma \leq 0.5$ MeV. The numbered lines in the panels correspond to different phase space estimations for the different reaction channels.*

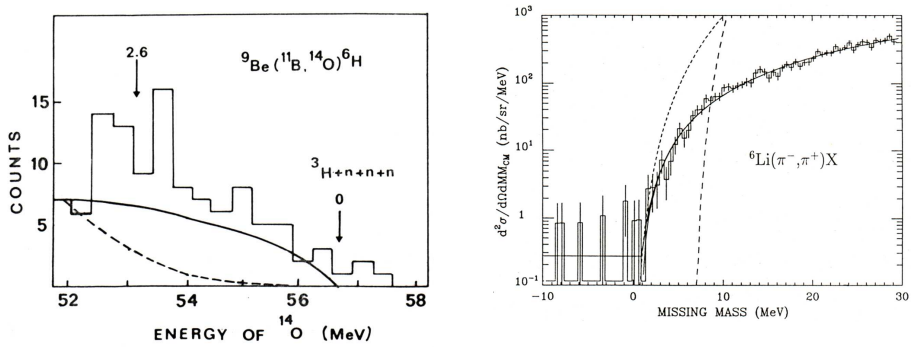

Figure 1.6: *Left panel: energy of the scattered ^{14}O in the $^9Be(^{11}B,^{14}O)^6H$ reaction from reference [Bel86]. The peak at ∼53 MeV is identified as the ^6H resonance at 2.6 MeV above the ^3H+3n threshold. Right panel: missing mass spectrum for the reaction $^6Li(\pi^-,\pi^+)X$ in reference [Par90]. The short-dashed line is the phase space distribution for ^3H+3n, the long-dashed line corresponds to the ^2H+4n phase space distribution. No peak was found that could be attributed to a ^6H resonance.*

Korsheninnikov *et al.* [Kor03] observed an enhancement in the cross section of the p(^{8}He,^{2}He)^{7}H reaction near the ^{3}H+4n threshold (see Figure 1.7), which cannot be explained by the different phase space contributions[14] checked by the authors. This was the first experimental information about the ^{7}H resonance. In a later work by Golovkov *et al.* [Gol04a] an attempt to detect directly the ^{7}H isotope was done. The ^{2}H(^{8}He,^{7}H)^{3}He transfer reaction used in this experiment revealed no trace of a ^{7}H state, and the authors set an upper lifetime limit of 1 ns, 3 nb/sr for the cross section, and a lower limit of 50-100 KeV for the resonance energy.

Our work follows in the path of these experimental studies and brings new data to confirm the existence of ^{7}H. Characterization of this resonance reveals it as the most exotic nuclear state ever studied, with the most unbalanced number of neutrons and protons. The extreme neutron excess creates a good scenario for further tests on the neutron-neutron interaction and consequently the nuclear interaction description. A new decay channel into five particles may be confirmed in latter studies and added to the list of new properties revealed by these nuclear states very far from stability. In addition, detailed studies of the structure and decay properties of ^{7}H may help to clarify the present debate [Mar02][Pie03] concerning the existence of a tetraneutron state[15] ^{4}n.

In the next pages we describe the experiment and analysis that leads to the confirmation of ^{7}H as a well-defined state. In this study we use a 15.4A MeV ^{8}He

[14] equivalent to include tetraneutron interaction, dineutron interaction, and no n-n interaction.
[15] within a possible cluster arrangement of ^{3}H+^{4}n in ^{7}H.

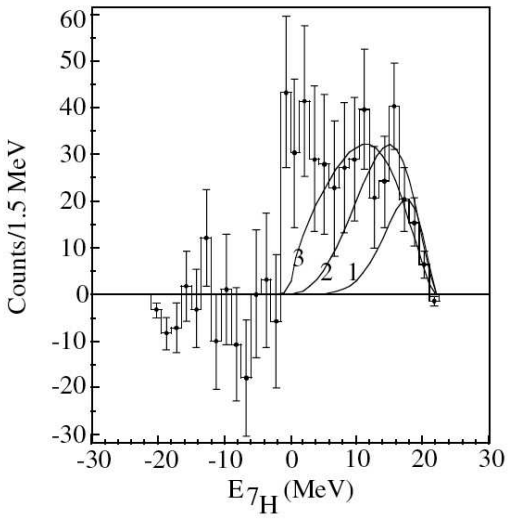

Figure 1.7: *Reconstructed energy spectrum of p(^{8}He,^{2}He)^{7}H reaction from reference [Kor03]. The curves show typical physical backgrounds: 3) two body, 2) three-body, and 1) five-body phase space contributions.*

beam impinging on a ^{12}C gas target to produce the ^{7}H resonance with proton transfer reactions between Helium and Carbon nuclei:

$$^{12}\mathrm{C}\ (\ ^{8}\mathrm{He},\ ^{7}\mathrm{H}\ )\ ^{13}\mathrm{N} \tag{1.6}$$

The experimental setup was placed in the GANIL facilities, which are described in the second chapter. The detectors used in the experiment are also described there, with special attention to the active target MAYA, where the reaction takes place and the products are identified. The chapter ends with a brief description of the associated logic and electronics.

The third chapter is devoted to the first stage of the data analysis. This includes the calibrations of the different detectors, and the translation of raw data into calculated data with the tracking of the reaction products trajectories and the determination of their ranges inside the detector, which allows us to calculate their energies. Finally, the determination of the target thickness and incident projectiles normalization are explained.

In the fourth chapter, the final step of the analysis begins with the identification of the ^{7}H reaction channel from among other possible channels by their distinct kinematics, and the calculation of the energy associated with the resonance. Once the ^{7}H events are identified, the resonance is characterized as a Breit-Wigner distribution, and the experimental production cross section is calculated.

Finally, the results are discussed in the fifth chapter.

Chapter 2

Experimental Setup

This chapter describes the experimental setup, located at the GANIL facilities, in Caen, France. The secondary beam required for the experiment was produced in the GANIL-Spiral installations, a specially designed facility that uses the ISOL method to produce radioactive beams. The main component of the detection setup was the MAYA detector, which was used as an active-target. The chapter begins with a brief overview on the GANIL-Spiral installations, where the experiment was performed. A detailed description of the detectors, especially the active-target MAYA appears in the second section. At the end of the chapter is an explanation of the electronics layout used during the experiment.

2.1 The GANIL-SPIRAL Facilities

GANIL (Grand Accelerateur National d'Ions Lourds)[Gan05] is a *Large European Facility* dedicated to the nuclear research since 1983. It consists of a beam production area where stable and radioactive beams are produced, and a modular experimental hall where the experiments are performed. See Figure 2.1 for a schematic view of the GANIL facilities.

Stable beams are produced and extracted from the *Electron Cyclotron Resonance* ion source (ECR4). They are accelerated in the *Compact Cyclotrons* C01, or C02, at around 0.5A MeV. The extracted beam is injected into two coupled *Separated Sector Cyclotrons* (CSS1 and CSS2) where it is accelerated, reaching typical average energies of 24A MeV and 96A MeV, respectively.

Radioactive beams are produced in two different ways depending on the desired

energy domain. Intermediate-energy radioactive beams are produced by the In-Flight separation technique [Viy79][Wes79], whereas low-energy radioactive beams are prepared with the *Isotope Separation On Line* (ISOL) [Vil95] technique. In the In-Flight method, the primary stable beam is directly extracted from CSS2 cyclotron and impinges on a thin production target, SISSI [Bar95]. The radioactive species are produced in fragmentation reactions, that leave the target in a narrow forward cone with velocities almost equal to those of the projectiles. The products are selected in flight in the α-spectrometer by means of their magnetic rigidity, and sent to the experimental areas.

The ISOL facility SPIRAL

The ISOL technique is used in the SPIRAL facility (Figure 2.2). In this method the primary beam impinges on a thick target where the radioactive species are created. The extraction is done in the *Electron Cyclotron Resonance Ion Source* (ECRIS) Nanogan III where the particles are also ionized in a permanent magnet at a charge/mass ratio of around 0.09 to 0.4, and accelerated with 7 to 34 kV. The *Low Energy Separator* selects the isotopes with a typical mass resolution of $\delta m/m = 4 \cdot 10^{-3}$. The selected species are injected into the *Cyclotron for Ions of Medium Energy* (CIME) where they are accelerated to energies between 1.7A MeV and 25A MeV, suitable for studying nuclear reactions around the Coulomb barrier and higher. Selections in mass, $\delta m/m = 5 \cdot 10^{-4}$, and charge, with $charge/mass = 0.1$ to 0.5, are nominaly achieved in the CIME device. The beam leaves the SPIRAL area through the α-spectrometer, where further magnetic rigidity selections are made before it is sent to the experimental areas.

The ^{8}He beam used in this ten-day experiment was produced with the ISOL technique in the SPIRAL area. A ^{13}C primary beam at 75A MeV impinged on the Carbon target, producing the radioactive species. After the extraction and the different selections, the resulting $^{8}He^{+2}$ at 15.4A MeV was delivered to the experimental area with an average intensity of around 10 kHz.

The energy loss spectrometer, SPEG

In this work the experimental setup was placed at the end of the *Energy Loss Spectrometer* (SPEG) [Bia89] (see Figure 2.3). Two main stages can be identified: the analysis beam line and the spectrometer, which are separated by a focal plane. In this experiment SPEG was used as a beam transport line, not as a spectrometer.

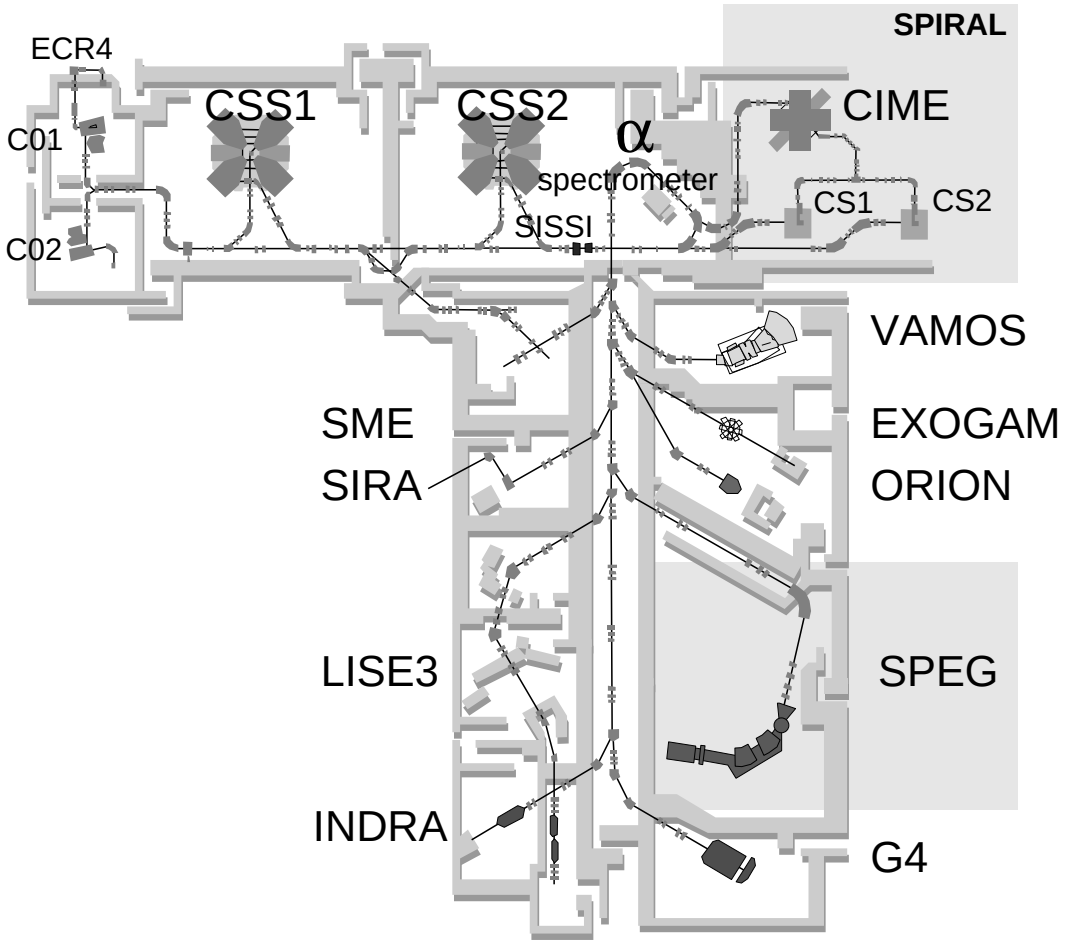

Figure 2.1: *GANIL facilities. The beam production area can be distinguished in the upper section, whereas the lower section corresponds to the experimental halls.*

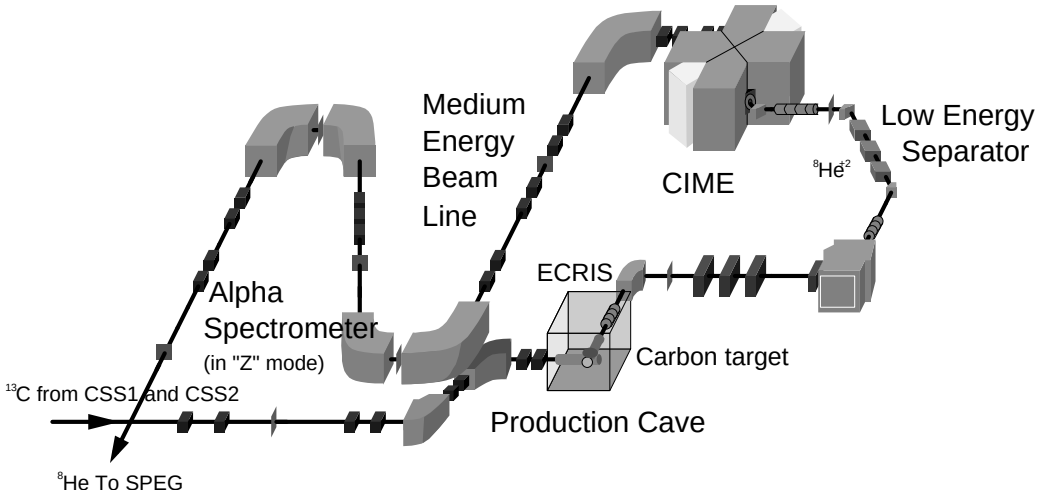

Figure 2.2: *View of the SPIRAL area. The* ^{13}C *primary beam impinges on a Carbon target. The radioactive species created are extracted and ionized, and then selected in a Low Energy Separator. The CIME cyclotron accelerates the selected* ^{8}He *isotopes to 15.4A MeV. The* α*-spectrometer makes a final selection by means of magnetic rigidity.*

The beam enters the spectrometer stage through a pair of slits and a quadrupole magnet, Q1. The spectrometer acceptance is controlled by the slits with a maximum angular acceptance of ± 2 deg. Two dipoles, D1 and D2 were used to drive the beam with great precision to the entrance of the detectors. The beam is again focused with a final quadrupole, Q2, before reaching the focal plane, 6.26 m after the last dipole. The spectrometer operates with a horizontal and vertical acceptance of ± 35 mrad and a solid angle of 4.9 msr. The ^{8}He at 15.4A MeV beam is $\sim$6 mm width at the entrance of MAYA, placed at the SPEG focal plane, with an emittance of $\varepsilon \simeq 10\ \pi$mm·mrad. The achromaticity of the beam line is assured with very small dispersions components. In the horizontal plane, the component $(x/\delta)^1$ is $\sim$0.1 cm/%, with an angular dispersion $(x/\theta)^2$ almost negligible. We can see the beam profile along the path inside SPEG in Figure 2.4.

2.2 Detectors

The detectors used in the experiment include a micro-channel plate detector for timing, four drift chambers placed before the focal plane that are used to monitor the beam, and the MAYA detector, based on the active-target concept, where the

[1] $(x/\delta) = \partial x/\partial(p/p_0 - 1)$ with x_0 as the reference trajectory.
[2] $(x/\theta) = \partial x/\partial\theta_0$ with θ_0 as the angle between particle and reference trajectories.

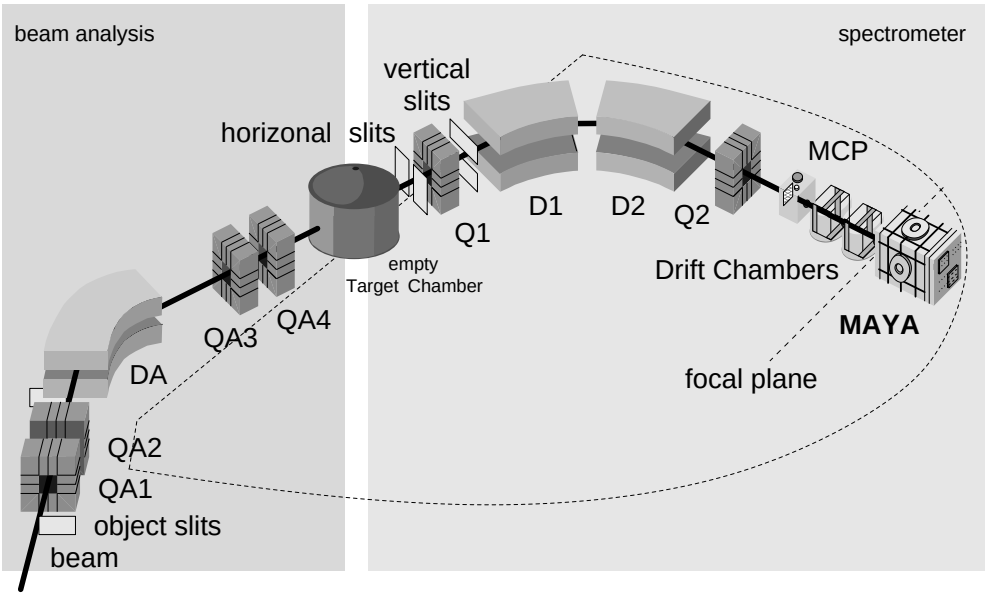

Figure 2.3: *Schematic view of the energy loss spectrometer SPEG, with the detection setup placed at the end of the line: Micro-channel plate (MCP), drift chambers, and MAYA with its entrance placed at the focal plane.*

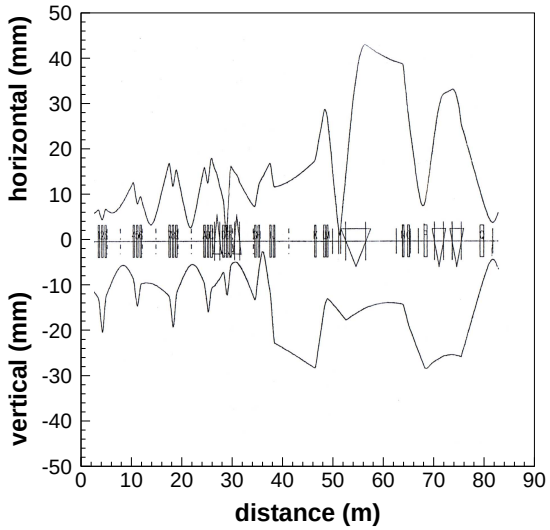

Figure 2.4: *Beam profile inside SPEG. The upper scale stands for the horizontal envelope. The downward scale marks the vertical envelope. The horizontal axis represents the distances between the different magnetic components in the beam line, starting at the α spectrometer and finishing in MAYA.*

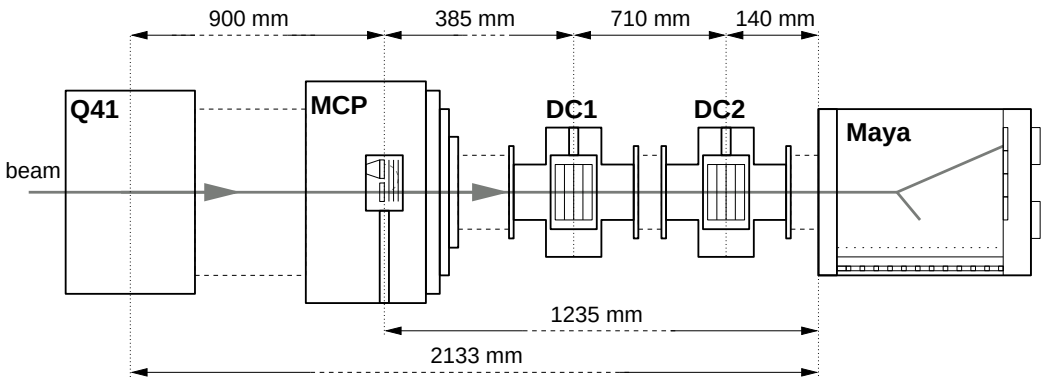

Figure 2.5: *Detailed view of the detectors used in the experiment, placed after the quadrupole Q41: the micro-channel plate detector MCP, the drift chambers DC, and the active target MAYA.*

reactions and the detection of the resulting products take place. The detection system is placed at the end of the SPEG line, as shown in Figure 2.3. Figure 2.5 indicates the distances between the detectors used.

2.2.1 Micro-channel plate detector

The basic design of this detector is presented in Figure 2.6. The beam enters the detector after passing through a thin 0.9 μm aluminized Mylar window. The interaction of the beam particles with the entrance window releases a certain number of electrons. Electric and magnetic fields are applied to accelerate and deviate the electrons to the micro-channel plate [Pan76], located over the entrance window.

The micro-channel plate consists of a metallic plate heavily perforated by μm diameter channels, with an electric field applied between both sides. The electrons interact with the channel walls and release more electrons, which in turn are accelerated by the electric field and interact again. At the end of this process there is a typical gain factor of 10^3 in the final number of electrons. The signal induced by the electron cloud that is released from the micro-channel plate is collected and sent to the acquisition system, with a time resolution of around 300 ps at Full Width Half Maximum (FWHM).

The energy loss and the angular straggling of the secondary 15.4A MeV ^{8}He beam in the Mylar foil are very small, around 15 keV and 150 μrad, resulting in a

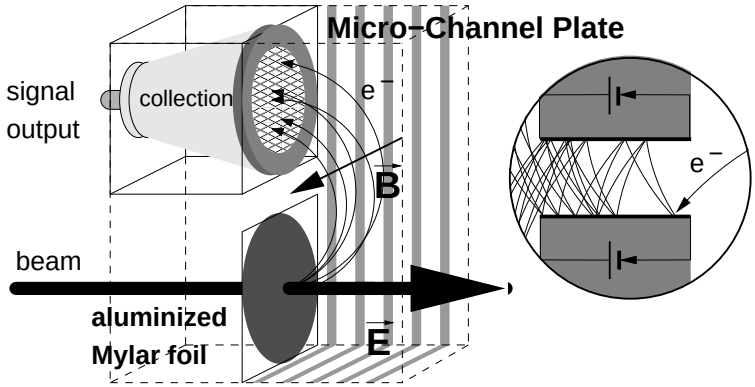

Figure 2.6: *Diagram of the micro-channel plate detector function. The circular panel illustrates the interaction of an electron inside a channel.*

virtually non-interactive detector.

2.2.2 Beam monitor drift chambers

Figure 2.7 gives a schematic view of one of the two monitoring drift chambers, which are placed 140 mm before the MAYA entrance and separated by 71 cm. A drift chamber has four $70\times70\times16$ mm^3 drift modules, each of which is filled with 20 mbar of isobutane, C_4H_{10}. A Frisch grid separates the drift zone from the amplification zone, which consists of an amplification wire and a lower cathode. The particles traversing the modules ionize the gas, creating ion, and electron clouds. An electric field of 500 V drive the electrons to the amplification zone. The drift velocity under these conditions is around 20 ns/mm, which results in a $\sim$1.4 μs total drift time. After being filtered through the Frisch grid [Fri89], the electrons are accelerated by the surronding field of the amplification wires with a voltage of 500 V, inducing a mirror charge in the cathode.

The orientation of each module is different, as seen in Figure 2.7. The difference in the drift times of the vertical modules determines the vertical position, and the horizontal position is determined by the difference in the drift times of the horizontal modules. The expected position resolution is around 200 μm in both dimensions. However, it should be pointed that the drift chambers operate primarily as beam

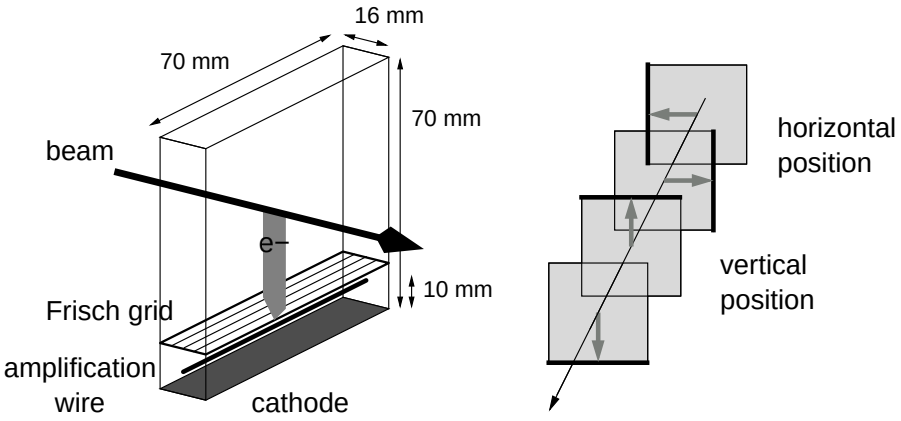

Figure 2.7: *Components of one of the drift chambers placed before the focal plane of the SPEG line. There are four modules: two for the horizontal position, with the cathodes on the right and the left sides; and two for the vertical position, with the cathodes on the upper and lower sides.*

monitors in this experiment, and not as position detectors.

Each drift chamber has two 1.5 μmm Mylar windows, and each of the four modules has two additional 0.9 μmm windows. At 15.4A MeV, the secondary ^{8}He beam loses 440 keV as it traverses the two drift chambers, with an angular straggling of 750 μrad. The total interaction of the beam with the micro-channel plate and the drift chambers results in an energy loss of 460 keV, and a total angular straggling of 760 μrad, leaving the secondary ^{8}He beam almost unaffected.

2.2.3 The active-target MAYA

Normally, radioactive beams are produced at lower intensities than stable beams. The typical production rate of the ^{8}He beam in this experiment was of the order of tenths of kHz, while the cross sections of the reactions of interest are frequently low, of the order of μb in our case. Increasing the detection effciency or the target thickness may help to minimize this problem, but an increase in the effective target thickness generally corresponds to a decrease in the final resolution. The active-target concept incorporates both solutions: the detector efficiency is increased to reach nominally up to 4π sr, and the effective target thickness is increased without losing resolution because detection occurs inside the target.

Active targets, such as bubble chambers, use part of the detection system as a reaction target. They were developed more than fifty years ago for use in high-energy physics. The archetype in the domain of secondary beams is the detector

IKAR [Dob83], used at GSI to study elastic scattering of exotic beams at relativistic energies. The use of IKAR was limited to H_2 at a pressure of 15 atm. Another example, the MSTPC [Miz99], was designed and built in Japan for detecting fusion and astrophysical nuclear reactions in the low-energy region. MSTPC is based on the working principle of a Time Projection Chamber. It uses a flash ADC readout for each cathode pad to measure the drift time, thus allowing three-dimensional tracking. Presently, there are new projects underway in the design and use of active targets: TRIUMF (Canada) [Tri05] in collaboration with the University of York (United Kingdom) is working on TACTIC [Rup05], a cylindrical ionization chamber developed to measure the differential cross sections of astrophysically relevant reactions covering a large angular region.

The MAYA detector [Gan02][Dem03][Mit03], developed at GANIL, is a gaseous active target for the low-energy domain. MAYA can be used with different types of gases, making it possible to study direct reactions with a wide variety of light gaseous targets. The MAYA detector is described in the next sections, with a detailed review of the signals it produces and an explanation of the particular conditions and settings used for this experiment.

General description of the MAYA detector

MAYA works essentially as an ionization chamber where the filling gas also serves as the target. Two main zones can be identified within the detector: the active zone where the reaction takes place, and the amplification zone where detection and readout occur. The volume of the active zone is $28\times26\times20$ cm^3, defined by a cathode plane at the top and the amplification zone at the bottom. The amplification zone consists of a Frisch grid in the upper part, an anode wire plane below that, and a segmented cathode in the lower part. The distances between these components can be adjusted to optimize resolution and amplification gain. The stainless-steel container of the detector, with a 1 cm in diameter Mylar window, was tested for gas pressures up to 3 atm. See Figure 2.8 for a schematic view of the detector.

The anode wires in the amplification zone run parallel to the beam axis. Their diameter can be modified to work with different beam and recoil particles ionization densities. The spacing of the wires should be smaller than the lateral straggling of the drift electrons in order to avoid digitalization of the induced charge. The anode wire plane is just above a lower cathode, which is segmented into 35×35 hexagonal pads, each of which measure 5 mm per side. The size of the pads was chosen to ensure position resolutions of the order of 1 % for ranges of 10 cm, thus maintaining a reasonable number of electronic channels. The hexagonal structure, with three symmetry axes, improves the reconstruction of trajectories, regardless of

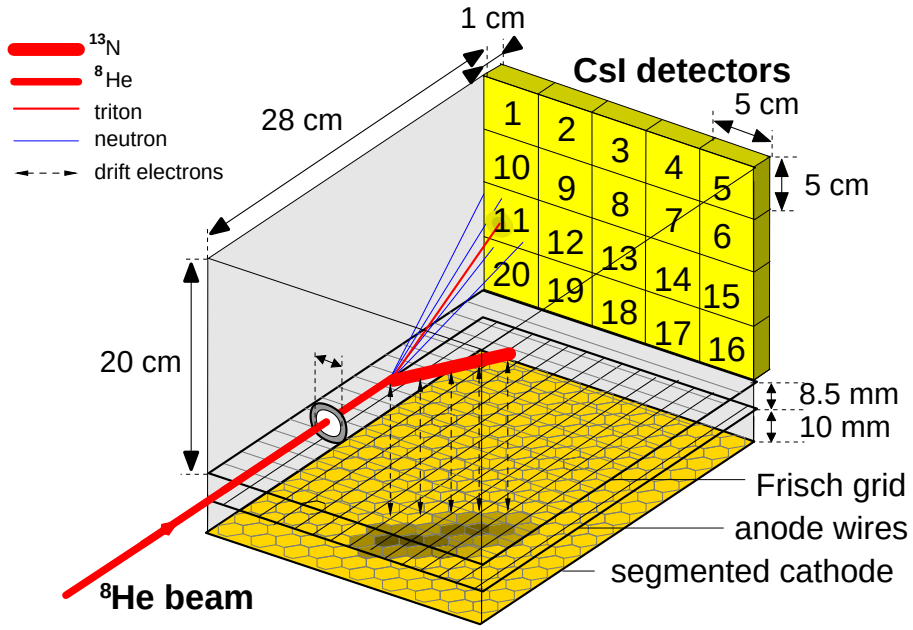

Figure 2.8: *The active target MAYA. Shown here is an example of the transfer reaction that creates the ^{7}H resonance.*

their directions. The pads are arranged in rows parallel to the proportional wires. Each set of wires corresponding to the same line of pads is connected to the same preamplifier. The distance between the cathode plane and the proportional wires determines the width of the induction pattern. The cathode plane is connected to a set of Gassiplex chips[3] [San94]. The signals induced in the pads are recorded and stored in the Gassiplex through a *Track & Hold* procedure, triggered by a signal from the wires, until they are sent to data acquisition.

In a typical event the beam enters MAYA through the Mylar window after traversing several monitor detectors and ionizes the filling gas. If a nucleus from the beam hits the nucleus of an atom in the gas a reaction takes place. The electrons from the atoms in the gas that have been ionized by the reaction products drift to the amplification zone by means of an electric field applied between the upper cathode and the proportional wires, while the Frisch grid is kept grounded. The induced charges in each cathode pad form a projected image of the particles trajectories. The homogeneity of the electric field is maintained by metallic strips covering the sides of the detector, except at the back, where they are replaced by field wires to reduce interaction with the forward escaping particles. The electric field can be set as high as 15 kV in the upper cathode, and 5 kV in the proportional wires, depending mainly on the pressure and the detection energy threshold of the

[3] 16 analogical multiplexed channel ASICs developed at CERN.

specific particles.

Direct kinematics generates scattered particles in a large energy domain. High energy light particles cannot be stopped in a reasonable gas volume and pressure, and escape from the active volume. The escaping particles are stopped and identified in twenty $5\times5\times1$ cm^3 Cesium-Iodide (CsI) crystal detectors, arranged in five columns and four rows which covers the exit face of the detector.

The CsI crystal detectors are inorganic scintillators sensitive to the interaction with ionizing particles. The constant pattern distribution of the atoms in a crystal creates bands of energy where electrons excited by the ionizing particle are promoted. The following deexcitation of these electrons releases light pulses that can be characterized with two components. The fastest one is sensitive to the mass and charge of the particle, and is used to identify the stopped particle.

The scattered light particles detected in the CsI wall trigger the acquisition, whereas the beam particles that do not react in the gas go towards a Nordic Gold (89 % Cu-5 % Al-5 % Zn-1 % Sn) stopper 22 mm in diameter, and 5 mm thick. ^{8}He projectiles at 15.4A MeV are fully stopped in 1 mm.

Event signals from MAYA

Event signals recorded from MAYA allow a complete reconstruction of the reaction kinematics that take place in the filling gas. The primary information comes from the tracking of the particles involved in the reaction through the charge projection induced in the segmented cathode, from the measured drift time and from the identification in the CsI detectors[4].

The interaction of the beam particles and the reaction products with the filling gas results in the ionization of the atoms in the gas. The released electrons drift from the point of ionization in the particle trajectory to the proportional wires, guided by the electric field applied in the gas volume. The electrons cross the Frisch grid before reaching the proportional wires in order to make the electronic cloud signal independent on its position from the ionizing track. As they approach the anode plane, the electrons are accelerated by means of the field gradient existing around the wires. The accelerated electrons ionize the surrounding gas, creating positive ions which drift toward the cathode pads below them. This process is depicted in Figure 2.9. The image charge induced by the movement of the positive ions is collected and recorded individually by each pad. The charge collected in the wires

[4]because drift time and charge data are collected MAYA is normally defined as a Charge-Time Projection Chamber.

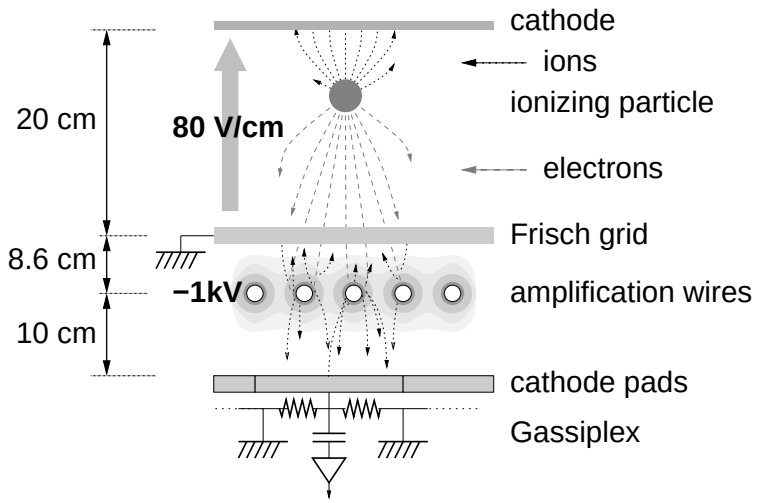

Figure 2.9: *Functioning mode of a drift chamber. The ionizing particle releases electrons from the atoms in the filling gas, which are driven through the Frisch grid to the amplification wires by means of an electric field. Further ionization of the gas surrounding the wires induces a signal in the cathode pads, which is recorded by the Gassiplex chips.*

is also recorded, producing the timing for the *Track & Hold* procedure in the pads, and the drift time stop, which has already been started by another signal, typically a Fast Trigger signal.

Depending on the reaction kinematics and the MAYA settings, the recoil and scattered particles can either be stopped inside the filling gas or escape toward the CsI wall, where they are stopped and their energy is measured.

Experimental settings for MAYA

The experimental settings are specific for each experiment. The main goal of this work is to study the ^{7}H resonance produced in transfer reactions between a ^{8}He beam, at 15.4A MeV, and a ^{12}C target. A plot of the kinematics of this transfer reaction (Figure 2.10) shows the different recoil and scattered energies. It should be noted that the ^{7}H scattered particle is unbound and it decays into triton and four neutrons in less than 1 ns [Gol04a], making the direct detection of ^{7}H impossible with this experimental setup.

MAYA was filled with isobutane, C_4H_{10}, a standard detection gas. This mixture contains the ^{12}C nuclei that are needed as target. The gas pressure is mainly determined by the energies of the particles involved in the reaction. According to the

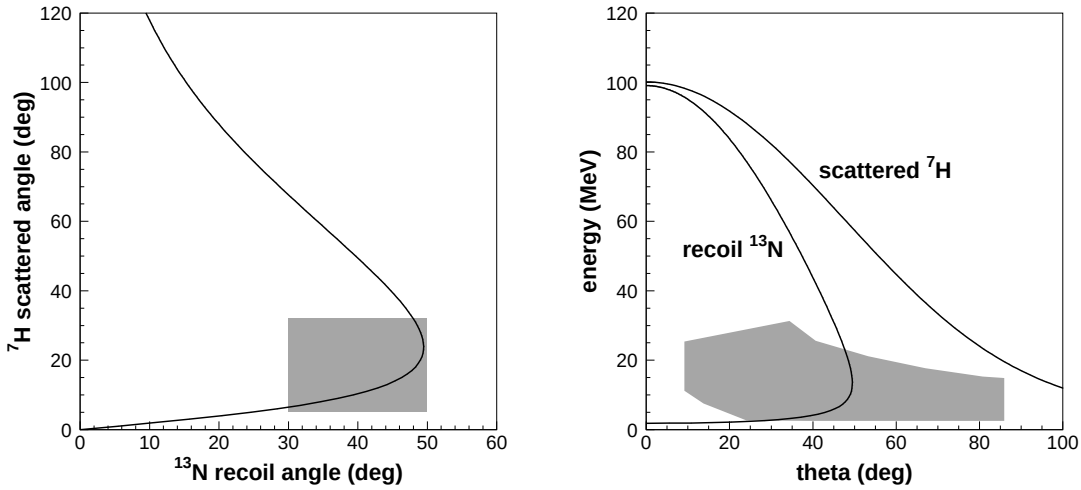

Figure 2.10: *Kinematics of the* ^{12}C(^{8}He,^{7}H)^{13}N *reaction. Left panel: angle with respect to the beam axis in the laboratory frame for the recoil* ^{13}N *and the scattered* ^{7}H*. Right panel: relation between energy and angle in the laboratory frame for both recoil and scattered particles. The grey areas represent the regions covered by MAYA.*

classic Bethe-Bloch formula [Zie99][Bet30][Blo33], the energy loss ($\frac{\mathrm{d}E}{\mathrm{d}s}$) of a charged particle moving through matter is a function of its charge (Z_p), mass (A_p), and velocity β, and of the charge (Z_t) and density (N_t) of the surrounding matter, in first approximation:

$$\frac{\mathrm{d}E}{\mathrm{d}x} = 4\pi \frac{Z_p^2 e^4}{A_p m_e \beta^2} Z_t N_t ln\left(\frac{m_e \beta^3}{Z_p e^2 \omega}\right) \tag{2.1}$$

with m_e, and e, being the electron mass and charge.

A particle stops when it loses all its initial energy, E_i. This happens at a given distance, defined as the particle range, R. Assuming the energy loss generally depends on the mass, charge, and energy of the particle, the range in a given matter can be expressed as:

$$\int_{E_i}^{0} E \ \mathrm{d}E \propto \int_{0}^{R} A_p Z_p^2 \ \mathrm{d}x \qquad \rightarrow \qquad R \propto \frac{E_i^2}{A_p Z_p^2} \tag{2.2}$$

Two experimental scenarios can be described depending on the different recoil and scattered particle energies (see Figure 2.10).

In the first scenario, the gas pressure is set high enough to stop the tritium, coming from the decay of the ^{7}H resonance, inside the MAYA detector. A typical reaction may produce a recoil ^{13}N at ∼0.5A MeV, and a tritium at ∼13A MeV. At 20 atm of isobutane the tritium stops in ∼10 cm, while the range of the recoil ^{13}N within this pressure would be around 130 μm, which is too short to be measured within 5 mm cathode pads. The reaction is reconstructed with the information carried by the ^{7}H resonance decay products: the tritiumn and the four neutrons. All of which need to be detected for an accurate reconstruction.

In the other scenario, the gas pressure is set low enough to stop the recoil ^{13}N within a reasonable range. The scattered tritium and the neutrons leave the detector, thus the main source of information is the energy and angle of ^{13}N. This scenario is much more convenient, since the information carried by the ^{13}N comes directly from the formation of the ^{7}H resonance without any intermediate reaction or decay. Moreover, if the pressure is adjusted to stop ^{13}N at energies of ∼10 MeV [5] the ^{7}H decay products move in forward angles (see Figure 2.10), allowing the detection of the triton in the CsI wall. In this scenario neither the ^{8}He beam nor the scattered triton leave enough energy to be detected in the segmented cathode. This scenario seemed best suited to our purposes and was used for this experiment.

In order to enlarge the energy domain of ^{13}N, two different gas pressures were used during the experiment: 26 and 30 mbar. The resulting thickness of the target-detector under these conditions is $3.2{\cdot}10^{19}$ ^{12}C atoms/cm^2 for 30 mbar, and $3.0{\cdot}10^{19}$ ^{12}C atoms/cm^2 for 26 mbar. Figure 2.11 shows the relation between energy and range, calculated with the SRIM code [Zie99][Sri05], as well as the mean energy loss of ^{13}N, and the tritium for both pressures.

Another critical parameter to determined is the amplification needed to induce a signal that could be distinguished above the noise level of the recoil particle ionization in the segmented cathode. The applied electric field and the geometry of the amplification wires along with the distances between the amplification plane, the segmented cathode, and the Frisch grid, determine the signal amplification for a given pressure. The energy deposition profile along the ∼80 mm path of ^{13}N at a typical energy of 0.5A MeV, is shown in Figure 2.12. Ideally, the amplification should be as high as possible, but with an applied electric field lower than ∼1200 V to avoid producing discharges inside the detector[6]. The Figure 2.13 shows a calculation of the expected amplification performed with the Garfield code [Ven91],

[5] with 30 mbar a ∼10 MeV Nitrogen stops in ∼10 cm.

[6] a high electric field can overcome the dielectric resistance of the gas and connect anode and cathode with producing a local shortcut

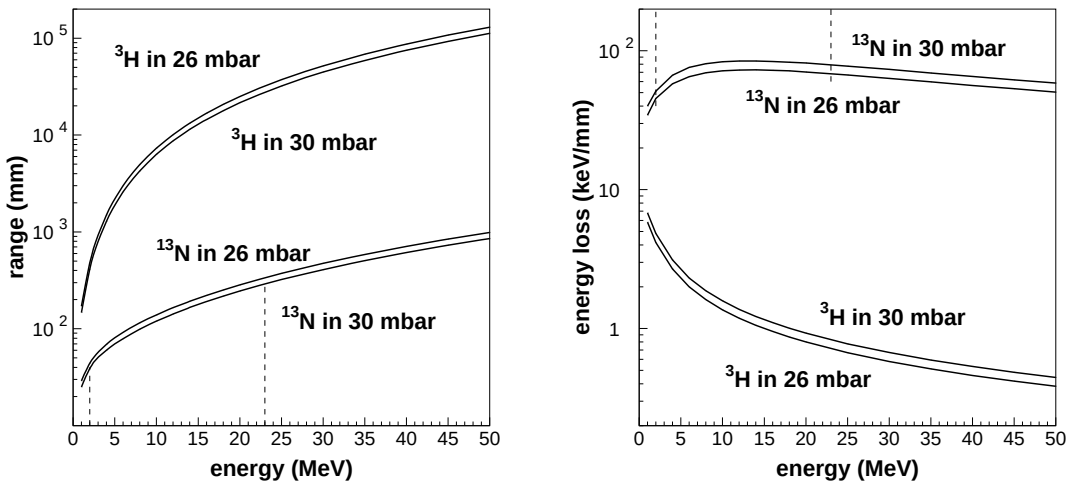

Figure 2.11: *Left panel: tritium and* ^{13}N *ranges versus their energy, at both pressures used in the experiment. Right panel: mean energy loss versus the total energy for both particles. The dashed lines mark the interval of energy detected in MAYA.*

with the following geometry: the anode wires were 10 μm in diameter; the Frisch grid and the anode wires were separated by 8.6 mm; and the distance between the segmented cathode and the anode wires was 10 mm. The electric field applied in the amplification wires was ∼1160 V for 30 mbar, and ∼1030 V for 26 mbar. The electric field between the upper cathode and the Frisch grid was set to 80 V/cm throughout the experiment. The measured drift velocity under these conditions was 48±3 mm/μs.

2.3 Electronics

This section provides a brief description of the electronics for the present experimental setup, which can be divided into four blocks according to the source of the signal: the monitoring drift chambers, the CsI detectors, the anode wires, and the cathode pads. The trigger signals are handled by the *Ganil Master Trigger* (GMT) module [Bou01]. Upon receiving a trigger, it generates a *Fast Trigger Analysis* (FTA) signal which starts the data readout for the time corresponding with the *Dead Time* (DT), also controlled by the GMT.

The drift chamber detectors (DC) are used to check the dimensions and center-

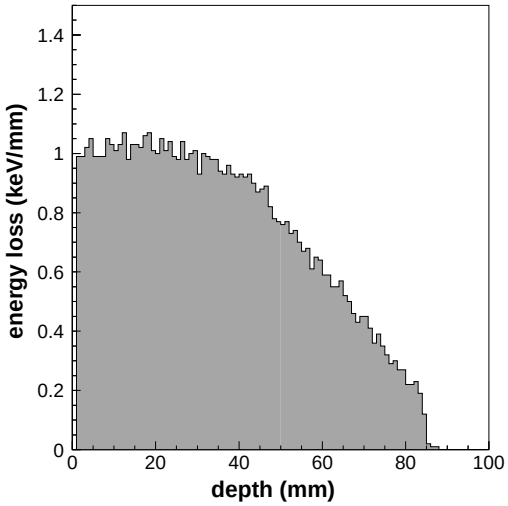

Figure 2.12: *Profile of energy loss for* ^{13}N *at 0.5A MeV, in 30 mbar of isobutane.*

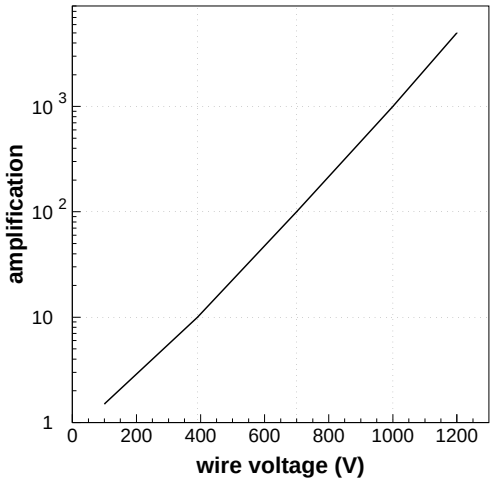

Figure 2.13: *Amplification of the anode wires estimated with the Garfield code, for the final geometry. The gas was set to 25 mbar of isobutane.*

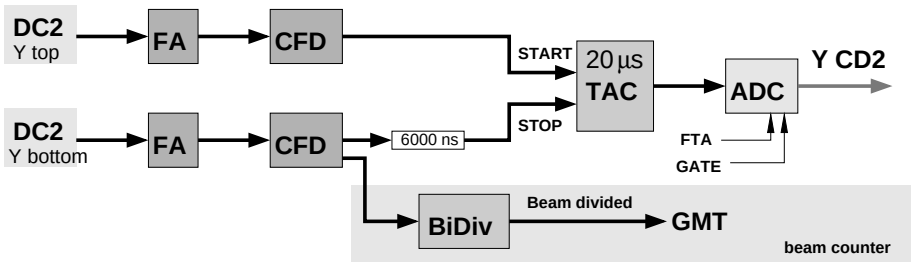

Figure 2.14: *Electronics of the monitoring drift chambers. For simplicity only the measurement of the vertical coordinate in the last drift chamber is shown.*

ing of the beam. Signals from the vertical and horizontal modules are amplified in a *Fast Amplifier* (FA) unit, and filtered in a *Constant Fraction Discriminator* (CFD), before being sent to a *Time to Amplitude Converter* (TAC). The resulting signal is coded in an *Analog to Digital Converter* (ADC) and sent to the acquisition.

In this experiment, the main task of these two detectors was to quantify the number of particles that reach MAYA, making it possible to determmine the absolute cross section. For this purpose, signals from the last module are sent to the *Binary Divider* (BiDiv) module, which functions as a proportional counter sending a trigger signal to the acquisition when a certain number of particles are detected. Figure 2.14 shows a diagram of the electronic setup for the last two modules.

The signals from the CsI detectors are used for triggering the acquisition and identifying the scattered particles stopped in any of the crystals. Each signal is integrated to give a number proportional to the total energy of the stopped particle. The light output from these crystal detectors can be separated into two main components with different characteristic times [Kno89], the fastest of which is sensitive to the charge and mass of the incident particle. In order to extract the information related to the nature of the particle, the signal, previously amplified in a $Pre-Amplifier$ (PA) coupled to the photomultiplier at the back of each crystal, is differentiated in a *Spectroscopic Amplifier* (SA), which is designed as the CsI *Fast Signal*. The SA also produces a *Slow Signal*, which is proportional to the energy deposited in the CsI crystal. Both signals are coded in an ADC and recorded in the acquisition system [Par02].

The *Fast Signal* also works as a trigger. There are two different trigger signals, depending on which detector has fired: The CsI-beam trigger signal is fired by the central detectors, # 8 or # 13 (labelled as in Figure 2.8). The remaining detectors fire the CsI-out (out of beam) trigger signal. Both signals are sent to the GMT.

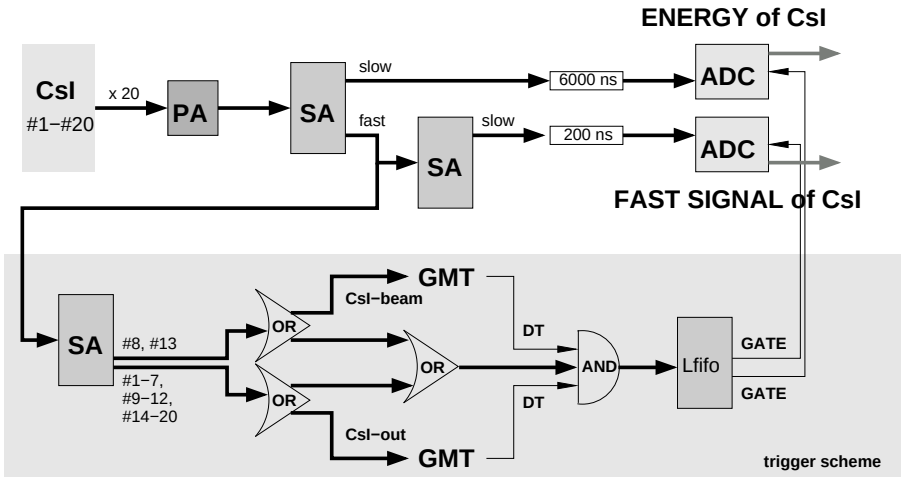

Figure 2.15: *Electronic layout of the twenty CsI detectors. The electronics associated with the acquisition trigger are highlighted in gray.*

Figure 2.15 shows the electronics associated with the particle identification and with the trigger.

Two observables are measured in the anode wires: the charge collected in the wires corresponding to each row of pads, and the drift time from the ionizing path. The pre-amplified signal from each wire is split into two signals: The charge measurement, which corresponds to the energy collected in the wire, is treated in an SA and sent to the acquisition through an ADC module.

The other signal provides the drift time measurement. This signal is amplified in a FA and filtered in a *Constant Fraction* (CF) module, before being sent as the stop signal to a *Time to Digital Converter* (TDC) where the drift time is measured and coded. The drift time start is the FTA signal fired by the CsI trigger.

The fast signal from the anode wires is also used for triggering the readout of the charge collected in the pads. A delayed signal from the *CAEN Readout for Analog Multiplexed Signals* (C-RAMS) module begins the delivery of the multiplexed data from the pads to the acquisition, 10 μs after the trigger. An *Inhibit* signal prevents the arrival of any other trigger signal during the readout process. See Figure 2.16 for a schematic view of the anode wires electronics.

The Gassiplex chips measure the charge induced in the pads by the amplification wires located just above them (see Section 2.2.3), and send the signal to the C-RAMS in multiplexed mode. The induced charge arrives to each pad in a pulsed form (after a certain rising time, the induction reaches its highest value and then decays to the pedestal value) and is measured by the Gassiplex chips with a *Track & Hold*

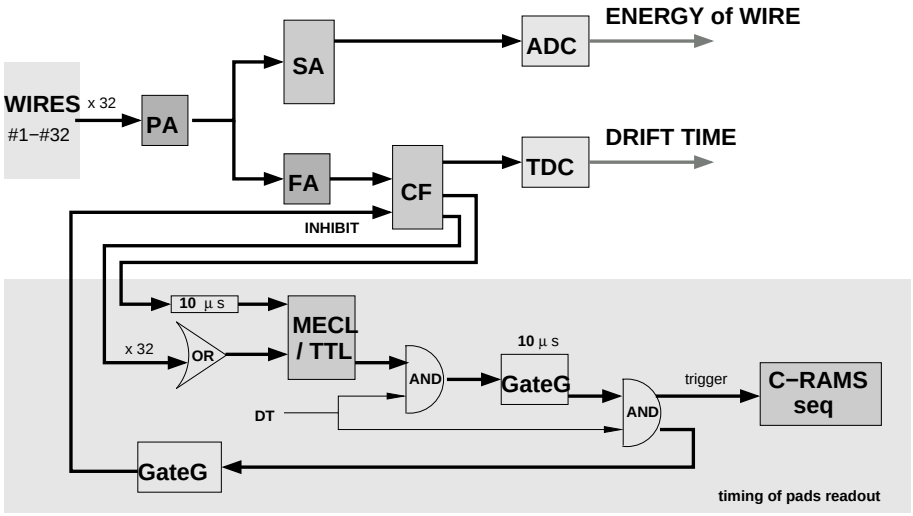

Figure 2.16: *Anode wires electronics. Drift time and collected energy are measured. The signal from the wires also starts the reading of the signals sent by the pads.*

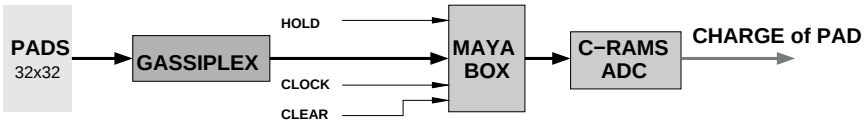

Figure 2.17: *Electronic scheme of the cathode pads. The 32×32 cathode pads send the signal recorded in the Gassiplex chips to the C-RAMS ADC.*

procedure. The measurement starts with a signal from the C-RAMS sequencer, triggered by the anode wires signal. The maximum amplitude of the charge induced in each pad is recorded when a *Track* signal, also triggered by the corresponding wire, arrives. The measuring gate is tuned in a specific module (MAYA Box) to be synchronized with the maximum induction. The Gassiplex chips store these numbers during the *Hold* time, and send them to the acquisition when they are requested by the C-RAMS sequencer. The electronics layout can be seen in Figure 2.17.

Chapter 3

Data Analysis

This chapter explains the experimental data analysis, beginning with the treatment of the raw data in Section 3.1. After they have been calibrated, the signals from the cathode pads and wires provide the physical observables needed to study the reaction of interest.

The interesting events are selected from among the possible reaction channels by applying different filters that verify the ocurrence of a binary reaction in which the recoil particle is stopped in the gas and a light particle is detected in the CsI wall. The drift chambers provide the number of incident projectiles, which makes it possible to monitor the ^{8}He beam intensity.

Section 3.2 describes the first-level of treatment of the calculated data, which includes the angle and energy of the recoil product[1]. These parameters are determined using the projected image from the charge induced by the recoil particle in the segmented cathode (see Section 2.2.3). The projected parameters are corrected by the reaction plane angle, which is determined from the drift time. Finally, Section 3.3 provides the calculation of the normalization to the number of projectiles and the target thickness, and gives an estimation of the detection efficiency of MAYA.

[1]information recovered from the recoil particle is used to unambiguously characterize the ^{7}H resonance, and is described in the next chapter.

3.1 Raw Data

The different signals coming from the detectors are recorded in the GANIL data acquisition. They are the raw data used to extract information about the reaction. The signals and calibration procedures are described in the following subsections.

3.1.1 Cathode pads calibration

The signals coming from each of the cathode pads are calibrated, by means of a pulse generator that simulates a charge induction from the wire, to give the same response when the same charge is induced. The timing of the $Track$ & $Hold$ procedure is the same as during the experiment (see Section 2.3). This process is repeated with different attenuation values applied to the first signal, which reproduce different inducing charges. A total of six signals were used in the calibration, along with an additional measurement that had no input signal, to establish the pedestal point. Figure 3.1 shows the input signals and the calibrated response for one of the pads. The calibration function was: $Epad(i,j) = (Qpad(i,j) - Q_o(i,j)) \times A(i,j)$, where $Qpad(i,j)$ and $Epad(i,j)$ are the raw and calibrated values for the pad in row i, column j[2], and $Q_o(i,j)$ and $A(i,j)$ are the pedestal value and the slope. This function allows for the detection of induced charges close to the pedestal. The response of the pads is proportional to the energy deposited in them.

3.1.2 Drift chambers

Each drift chamber is formed by four modules. The last module of the second drift chamber sends a trigger signal to the acquisition when a fixed number of projectiles (reduced by a division factor) has been detected. These triggers are sent to the acquisition and recovered in the analysis. The detector efficiency is checked by comparing the total number of events detected with the number of events detected in the first module of the first drift chamber. Relative efficiency during this experiment was estimated at 85 ± 1 %. The number of incident projectiles is obtained by multiplying the number of triggers by the division factor, and correcting the result with the estimated detector efficiency (see Section 3.3).

[2] rows are parallel to the beam direction, columns are perpendicular. See Figure 3.7.

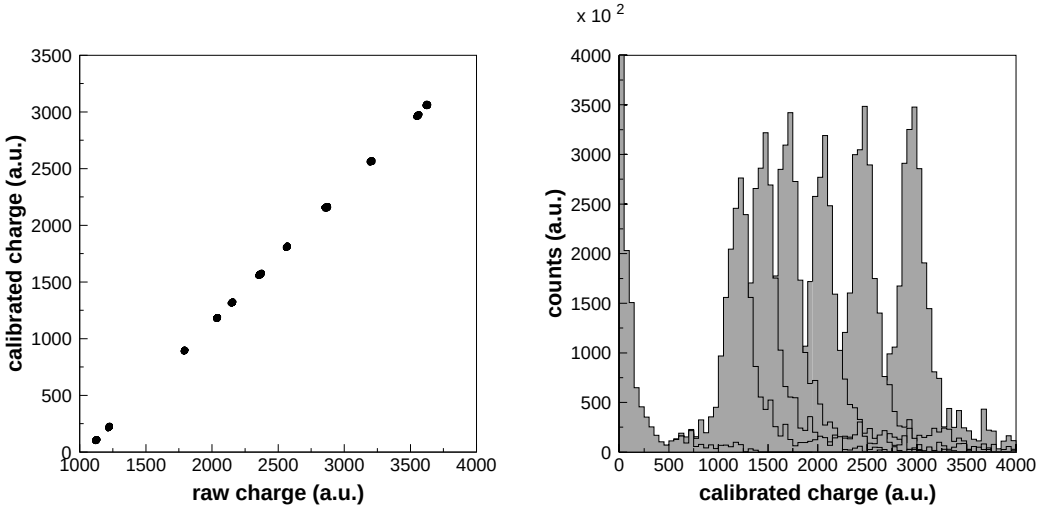

Figure 3.1: *Left panel: calibration of one of the cathode pads. Right panel: responses of the 32×32 pads for different input signals, calibrated to 1250, 1500, 1750, 2100, 2500, and 3000 arbitrary units.*

3.1.3 MAYA drift time calibration

The anode wires of MAYA send two signals to the acquisition: one is proportional to the charge collected in each wire ($Efil$) and the other is proportional to the drift time ($Tfil$). The $Efil$ signal is only used for cross-checking in the present analysis. The $Tfil$ signal is used for calculating the drift time of the electronic cloud created by the ionizing particle. This time is measured with TAC modules (see Section 2.3) that have been calibrated with a Time Calibrator (see Figure 3.2). The drift velocity is evaluated from the calibrated drift time. The beam particles enter MAYA through a Mylar window that is longitudinally centered 100 mm above the anode wires. Every reaction inside MAYA has its vertex in the path of the beam projectile, so ionization always begins over the central wires. Figure 3.3 shows the measured drift time in wire # 18 (located in the center region). The resulting drift velocity is 48±3 mm/μs for both pressures. The MAYA settings for the ^{8}He beam correspond to reduced fields of 2700 Vcm^{-1}atm^{-1} for 30 mbar, and 3100 Vcm^{-1}atm^{-1} for 26 mbar. See Figure 3.4 for a comparison of the resulting values and previous measurements (see reference [Pei84]).

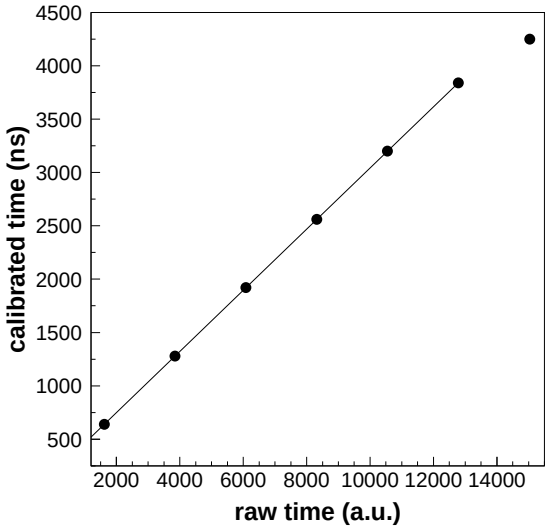

Figure 3.2: *Calibration of one of the TAC modules. Each input time has an integer multiplication factor of 640 ns.*

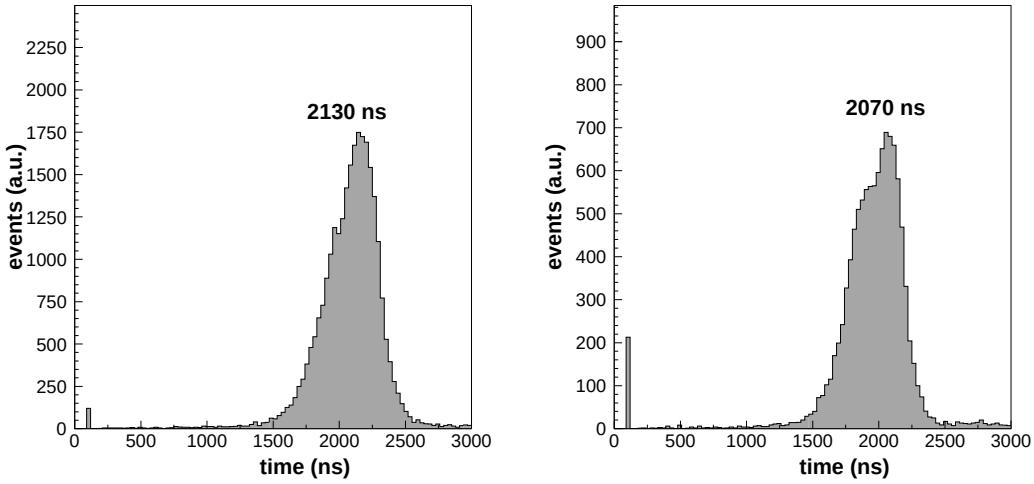

Figure 3.3: *Measured drift time in wire # 18 for 30 mbar (the left panel) and 26 mbar (right panel) of pressure.*

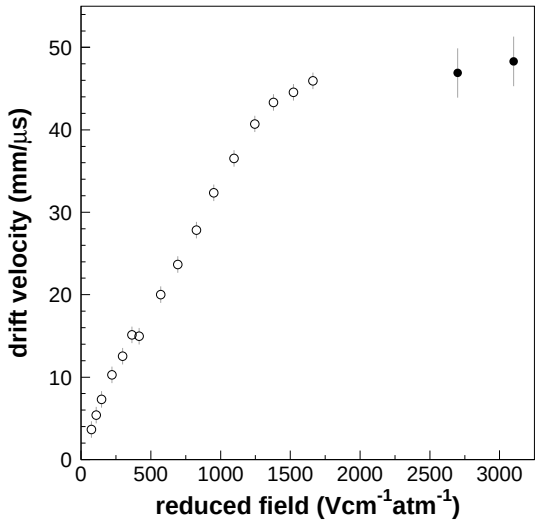

Figure 3.4: *Different drift velocity measurements for different reduced fields in isobutane from reference [Pei84]. The black points correspond to the values calculated in this experiment.*

3.1.4 CsI detectors

The relatively high-energy light particles that are produced in the different reactions leave the active volume of MAYA and are stopped in the CsI detectors at the back of MAYA. These detectors send two signals to the acquisition: $ECsI$ (Energy of CsI) which is proportional to the total energy deposited in the detector, and $FCsI$ (Fast signal of CsI), which is sensitive to the nature of the particle (see Section 2.3). The correlation between both quantities can be observed in Figure 3.5 for CsI # 8, where the lines corresponding to each type of particle appear clearly. Two main groups can be distinguished that correspond to different nuclear charges: the isotopes with Z=2 form the first set of lines, with the steepest slope, while the lower lines correspond to the Z=1 isotopes. The lines corresponding to Z=2 isotopes seem to have different slopes, while the Z=1 lines have the same slope but different offsets[3]. The coordinates were changed to create a better separation between the different lines inside each group: the $FCsI$ axis was traded with either the slope for the Z=2 lines, or the offset in the lines of Z=1 isotopes. Figure 3.6 shows the new identification obtained with the change of coordinates.

The ^{8}He line can be identified as the most populated one in the Z=2 set. Lines for

[3]this effect is due to the fixed size of the integration window in the electronics for the fast signal

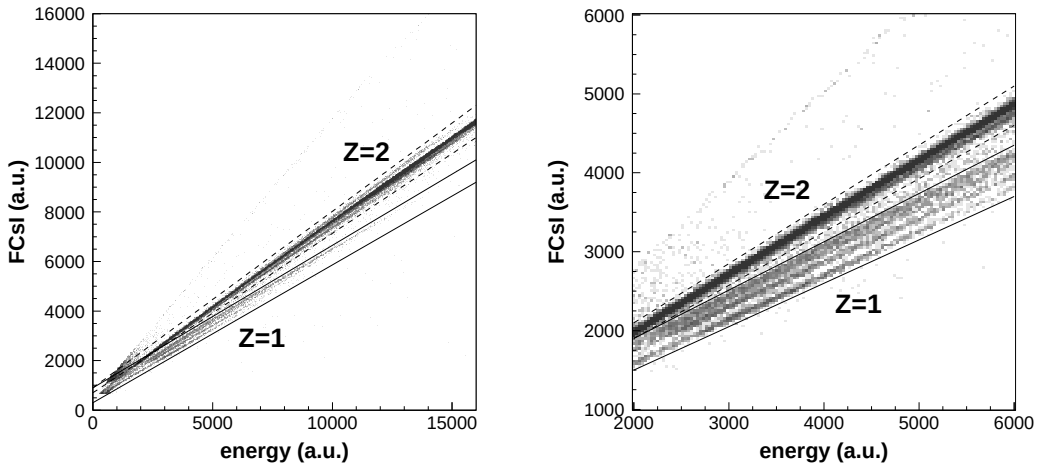

Figure 3.5: *Light particle identification with CsI. The right panel is a magnified area of the left panel. The dashed lines mark the Z=2 isotope region and the solid lines correspond to the Z=1 region.*

^{6}He and ^{4}He are also visible. ^{7}He, and ^{5}He isotopes do not appear in the histogram because even if they are produced, they do not live long enough to reach the CsI detectors[4] [Eks99]. An indication of Lithium isotopes line can also be distinguished at the limit of the detection capability. The Z=1 group is built with the three stable Hydrogen isotopes: tritium, deuterium, and protons. The fourth line corresponds to background noise, mainly β particles.

The scattered particles in the CsI detectors are identified before the ^{12}C(^{8}He,^{7}H)^{13}N reaction can be selected, with the ^{7}H resonance decaying into a tritium and four neutrons. The events selected are those in with only one particle (in this case a tritium) hits the CsI wall.

3.2 Calculated Data

In this work, ^{7}H resonance is characterized by the kinematics of the transfer reaction in which it is produced. For any given reaction there is a unique relation between the energy and the angle of the particles involved (see Figure 2.10). The energy and angle of the recoil product ^{13}N, stopped inside MAYA, provide the information needed to characterize the reaction. The procedure for obtaining these two observables from

[4] $\tau(^{7}\text{He})\sim10^{-21}$ s, $\tau(^{5}\text{He})\sim10^{-18}$ s.

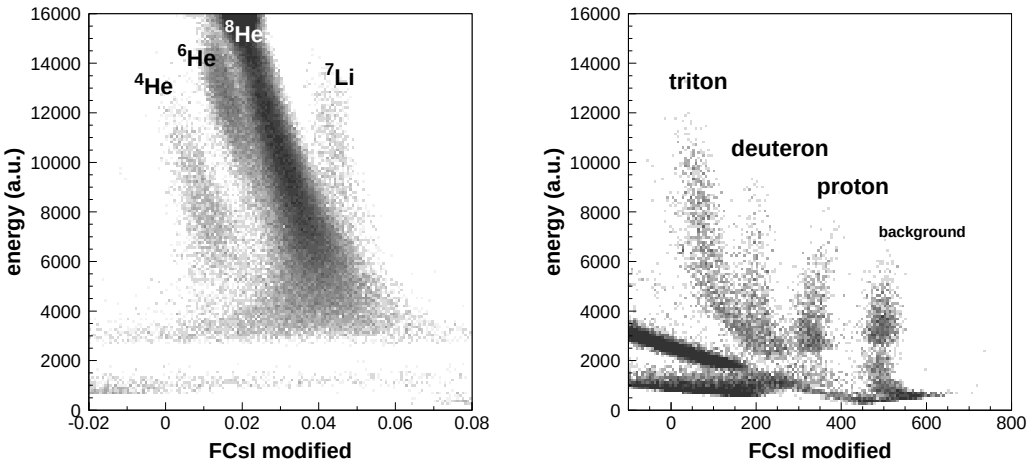

Figure 3.6: *Identification lines in CsI detector # 8 after changing the coordinate system. The left panel corresponds to the Z=2 isotopes, and the right panel corresponds to the Z=1 isotopes.*

the experimental data is described in this section.

MAYA facilitates complete tracking of the particles that stop inside its active volume. The projection of these trajectories in the segmented cathode provides the information for calculating the projected range (R_{2d}) and the projected angle with respect to the beam axis (θ_{2d}). R_{2d} and θ_{2d} are translated into the particle range (R) and angle (θ) with the help of the reaction plane angle (ϕ), which is obtained from the drift distances measured in the anode wires. Finally, the energy of the recoil product is extracted from the relation between energy and range, as seen in Figure 2.11.

Here it is useful to explain some conventions used in the rest of this chapter. The projection plane in MAYA, defined by the segmented cathode, is divided in two areas by the beam axis: the left side includes the first 17 rows of pads, and the right side includes rows # 18 to # 32. Each pad is labelled (i, j) according to its position, with i as the row number and j the column number. The columns are numbered from the entrance of MAYA. These conventions are illustrated in Figure 3.7.

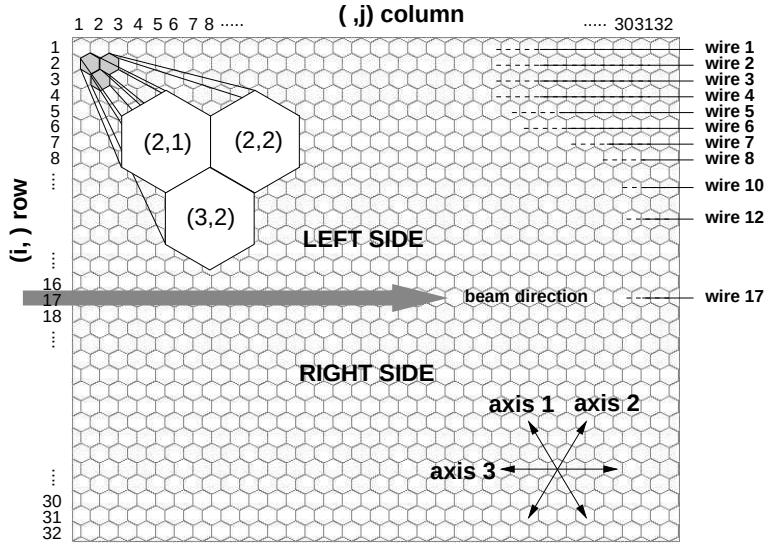

Figure 3.7: *Conventions used in the text for different elements in the cathode plane of MAYA.*

3.2.1 Determining the reaction plane

The ^{12}C(^{8}He,^{7}H)^{13}N reaction leaves only one recoil particle in MAYA: the ^{13}N isotope. Since this is a binary reaction, the scattered and the recoil particles define a reaction plane. The angle of this reaction plane (ϕ) can be determined from either of the two particles.

Each reaction product goes in a different direction, to the right and left of the projectile direction, according the principle of total momentum conservation. In the present experimental setup, only the recoil particle induces a signal in the segmented cathode, so its projection is either on the right or left side of the cathode plane and its drift time is measured only in the wires of the corresponding side. A new filter for data analysis[5] is created by selecting those events with signals from the wires of only one side of the cathode plane, and with reasonable associated drift times.

The drift $Tfil_i$ times measured in each i row are translated into distances using the calculated drift velocity of the electronic cloud, $V_{drift} = 48$ mm/μs. The drift distance increases perpendicular to the beam axis by a factor $\tan\phi$. Knowing the distance between the wires, i.e. between the rows of pads to be $\Delta x = 7.73$ mm, the angle ϕ is calculated:

[5]expressed as $[(\#\text{wires}_{\text{right}} > 2) \wedge (\#\text{wires}_{\text{left}} < 2)] \vee [(\#\text{wires}_{\text{left}} > 2) \wedge (\#\text{wires}_{\text{right}} < 2)]$ in Table 3.1.

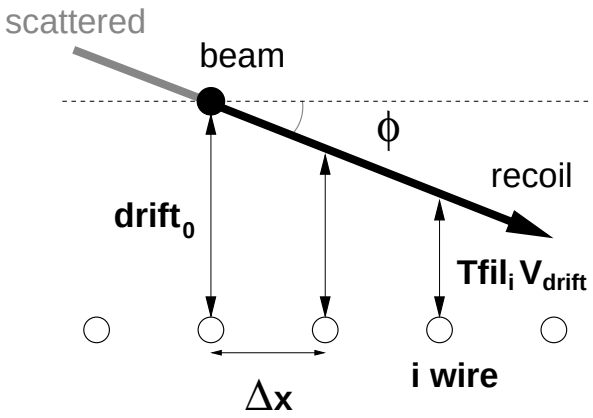

Figure 3.8: *Front view of a reaction in MAYA. Electrons drift from the ionizing recoil path down to the anode wires. The reaction plane angle ϕ is obtained from their arrival times.*

$$Tfil_i \cdot V_{drift} = \tan\phi \cdot i \cdot \Delta x + drift_o \tag{3.1}$$

where $drift_o$ is the offset time corresponding to the reaction point. Figure 3.8 illustrates this process.

The reduced χ^2 calculation determines the goodness of the fit:

$$\chi^2 = \sum_{i=1}^{n} \left(\frac{Dfil_i - D_i}{\epsilon_i} \right)^2 \frac{1}{n-2} \tag{3.2}$$

with

$$Dfil_i = Tfil_i \cdot V_{drift} \quad \text{and} \quad \epsilon_i = 0.1 Dfil_i \tag{3.3}$$

where n is the number of fired wires. $Dfil_i$ and D_i are the calculated and fitted drift distance for each i wire. The uncertainty ϵ_i is established as 10 % of $Dfil_i$ due to the uncertainty in V_{drift} (see Section 3.1).

If the reduced χ^2 associated with the fit is larger than 2, we exclude those points where the difference between $Dfil_i$ and D_i is two times larger than the corresponding ϵ_i. The fitting process is repeated until χ^2 is lower than 2. In addition, those events with less than three points at the end of the process are rejected.

The uncertainty associated with the resulting ϕ angle, $d\phi$, is calculated from the uncertainty of the fitted slope, $d\tan\phi$ (see Equation A.4 in Appendix A.1). Determining the ϕ angle from projected times is very inaccurate for angles close to 90 deg. In order to avoid these events a new filter is applied: only events with ϕ less than 60 deg are accepted for further analysis[6][7].

3.2.2 Calculation of the recoil angle

Calculation of the θ angle, associated with the recoil particle direction respective to the beam direction, is used to reconstruct the kinematics of the reaction.

When the electronic cloud created by the ionizing particle reaches the anode wire it ionizes the surrounding gas. The positive ions drift to the cathode and induce a mirror charge in the pads. The distribution of this charge created by a point source can be expressed as [End81]:

$$\sigma(x,y) = \frac{-Q}{2\pi}\sum_{n=0}^{\infty}\frac{(2n+1)L}{[(2n+1)^2L^2+x^2+y^2]^{3/2}} \tag{3.4}$$

where Q is the total charge, L is the gap distance between the anode wire and the cathode plane, and x, y expresses the position in this plane.

Figure 3.9 shows the shape of the charge distribution along one axis in the cathode plane, calculated with the experimental settings used in this work. The convolution of the charge distribution with the size of the pads expresses the individual charges deposited in each pad. A projection of the particle trajectory can be obtained by mapping the individual charges in the cathode.

The first step in reconstructing the trajectory is to find the maxima of the charge deposited. A maximum is defined as the highest charge with two non-zero neighbouring charges. The search is performed along each of the three symmetry axes in the hexagonal pads, and the number of maxima is recorded and stored. Those events with more than one maximum in each axis row can be related to more than one trajectory inside MAYA, and they are rejected. The axis with the largest number of maxima is chosen. Figure 3.10 illustrates this process.

The positions of the pads with the maximum charges are a rough estimation

[6] $|\phi| < 60$ deg in Table 3.1.

[7] with this cut ranges of 20 cm and 50 deg within the ^{7}H kinematics are assured to not leave the detector through the roof or the ground.

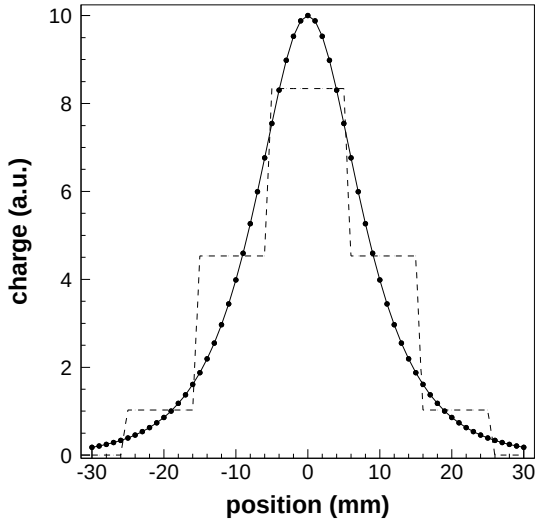

Figure 3.9: *The charge distribution produced by a point source along one dimension, according to Formula 3.4, is represented with connected points. The dashed line represents the corresponding charge collected in five pads placed below the induction point.*

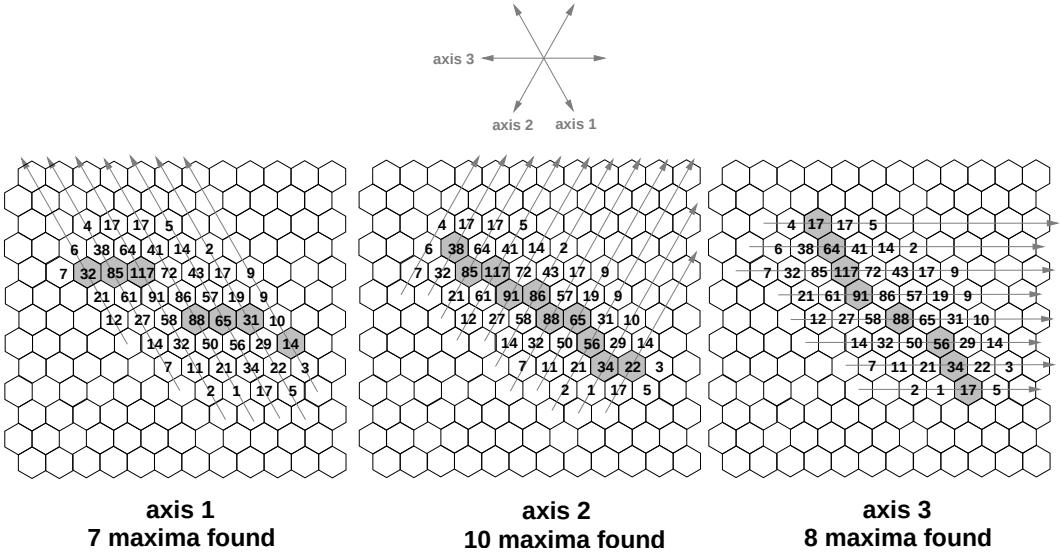

Figure 3.10: *Review of the search for maxima of charges in the cathode plane along the three axes of symmetry. The axis that yields the largest number of maxima is associated with the recoil trajectory.*

of the intersection points of the chosen symmetry axis with the real trajectory of the particle. In order to refine these points, the charge distribution centroid is calculated which, in principle, to the position of the induction point. A modified version [Dem03] of the *Hyperbolic Secant Squared* (SECHS) formula [Lau95] is used:

$$\Delta_R = \frac{w}{2} \cdot \frac{ln\left(\frac{1+a_1}{1-a_1}\right)}{ln\left(a_2 + \sqrt{a_2^2 - 1}\right)} \tag{3.5}$$

with

$$a_1 = \frac{\sqrt{\frac{Q_0}{Q_+}} - \sqrt{\frac{Q_0}{Q_-}}}{2 \cdot \sinh a_2} \quad \text{and} \quad a_2 = \frac{1}{2}\left(\sqrt{\frac{Q_0}{Q_+}} + \sqrt{\frac{Q_0}{Q_-}}\right) \tag{3.6}$$

The position of the centroid is then estimated to be a certain distance Δ_R from the center of the pad with the maximum charge Q_0. Q_+ and Q_- are the charges of the right and left neighbouring pads, and $w = 8.66$ mm is the width of the pad. Previous experiments [Dem03] with MAYA using the same configuration reported a centroid position resolution of ~ 0.3 mm. The centroid calculation uncertainty in this work is estimated to be within 1 mm[8]. The difference is mainly due to the different pressure and amplification conditions in the MAYA setup (see Section 2.2.3).

Once the charge centroid positions[9] are calculated, a fit is done using the iterative process, which is based on the χ^2 value (see Section 3.2.1), to obtain the projected direction of the particle. The χ^2 evaluation is also used for discriminating between symmetry axes with the same number of maximum charges found. The projected angle θ_{2d} is defined by the projected direction of the particle with respect to the anode wires. The direction of the anode wires corresponds to the beam direction with a precision of 0.38 deg[10]. Those events with the projected θ_{2d} angle lower than 5 deg are rejected[11]. This limit is established as the minimum angle for a $\sim$15 cm maximum range with at least three fired wires, which are needed in order to calculate the reaction plane ϕ angle.

The calculated direction is a projection of the θ angle of the particle in the cathode plane. The value of θ depends on the projected θ_{2d} angle and the reaction plane angle ϕ:

[8] based on the minimum value that allowed a fit for most data trajectories, using the χ^2 iterative method.

[9] i.e. the intersection points of the symmetry axis with the trajectory of the particle.

[10] the error in the beam alignment was checked with a 15.4A MeV ^{16}O beam.

[11] $|theta_{2d}| \geq 5$ deg in Table 3.1.

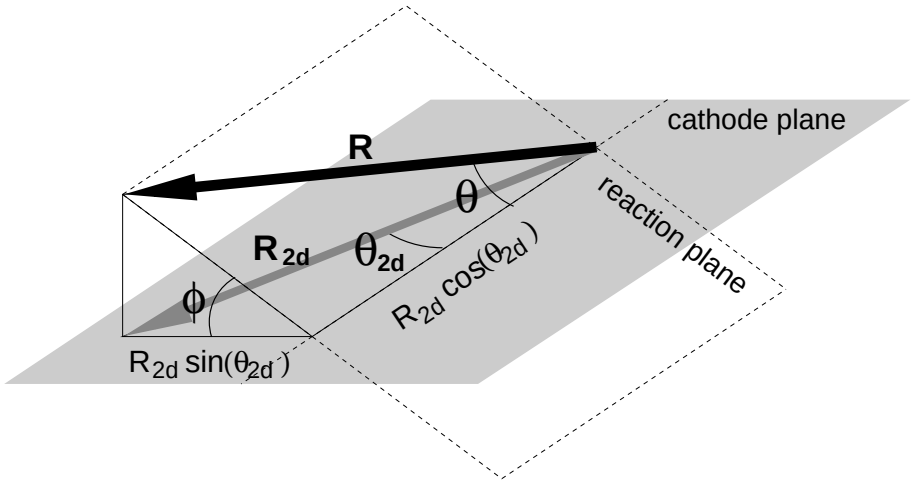

Figure 3.11: *Relation between the projected angle θ_{2d}, the real θ, and the ϕ angle of the reaction plane. The range R and its projection R_{2d} are also depicted*

$$\theta = \text{abs}\left[\arctan\left(\tan\theta_{2d}\sqrt{1+\tan^2\phi}\right)\right] \tag{3.7}$$

Figure 3.11 shows the relation between these magnitudes.

The estimated uncertainty for the θ angle calculation depends on the goodness of the fit of the projected trajectory, $d\theta_{2d}$, the uncertainty of the ϕ angle and the uncertainty of the angle of the projectile direction, $d\theta_{beam} = 0.38$ deg (see Equation A.5 in Appendix A.1).

3.2.3 Calculation of the recoil energy

There is a unique relation between the range of a specific isotope in a specific gas and its energy. Consequently, the energy of the recoil particle can be determined from its range in the filling gas of MAYA.

The cathode pads collect induction charges proportional to the energy loss in the gas above them, making a projection of the particle path. The projected range of the particle can be defined as the distance between the beginning and the end of the charge deposition along the path of the particle. The cathode pads receive the charge deposition after the amplification in the anode wires. The induced charge profile is then the convolution between the energy loss and the distribution of the

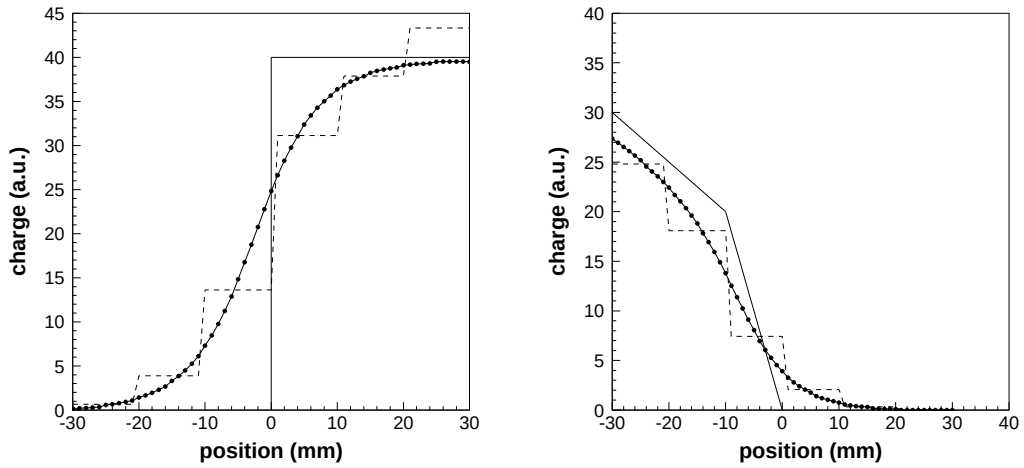

Figure 3.12: *Starting (left panel) and end (right panel) points of the inducted charge from an ionizing particle in the gas. The solid lines represent the expected energy loss of the particle. The connected points are the convolution of the energy loss distribution with the induction of a point charge. The dashed lines are the charge profile collected in the pads.*

induction by a point charge (see Equation 3.4). The resulting profile is depicted in Figure 3.12.

The geometry of the pads and the distribution of the induction charge modify the charge profile, especially at the beginning and the end of the trajectory. These points are determined within the geometry of the cathode pads by means of the charge profile. This profile is meant to be a numerical function of the deposited charge, integrated in fixed steps along the projected trajectory of the particle. The width of each step is the distance between two consecutive intersection points of the projected path with the selected axis of symmetry, as defined in Section 3.2.2. The step width for the different axes is then:

$$\delta_{axis\ 3} = \frac{\Delta y_3}{\sin\theta_{2d}} \qquad \delta_{axis\ 1,2} = \frac{\Delta x_{1,2}}{\cos\theta_{2d}(1+\frac{\tan\theta_{2d}}{\tan 60^o})} \tag{3.8}$$

with $\Delta y_3 = 7.7$ mm, and $\Delta x_{1,2} = 8.7$ mm being the distance between the centers of two consecutive pads (see Figure 3.13).

At each step along the projected trajectory, the charges[12] along the selected axis

[12]more specifically, three charges on the left and three on the right side are added to the charge

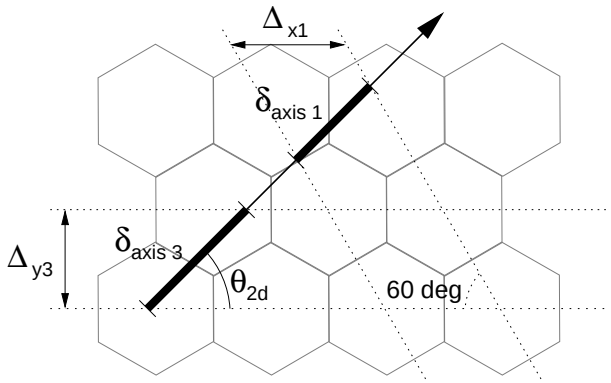

Figure 3.13: *Graphical view of the δ_{axis} calculation along axis 1 and 3.*

are summed (see Figure 3.14).

The starting and ending point positions of the path were determined using the Center of Gravity (CoG) method of the numerical derivatives, evaluated at the beginning and end of the charge profile, respectively (see Figure 3.15).

The starting point position[13] is determined using the first three components:

$$Pos_{vertex} = \frac{pos_1 + pos_2}{2} + CoG_{vertex} \tag{3.9}$$

with pos_i as the position of the i^{th} component of the charge profile, and

$$CoG_{vertex} = \frac{\delta q_0 - \delta q_2}{\delta q_0 + \delta q_1 + \delta q_2} \qquad \text{with} \qquad \delta q_i = q_{i+1} - q_i \tag{3.10}$$

where q_i is the charge in the i^{th} component of the charge profile, and $q_0 = 0$.

The CoG of the ending point is calculated with the last two components of the charge profile $q_{second-last}$ and q_{last}:

$$Pos_{range} = Pos_{last} + \frac{\Delta x_{axis}}{2} CoG_{range} \tag{3.11}$$

placed in the intersection between the axis and the trajectory.

[13]corresponding to the vertex of the reaction.

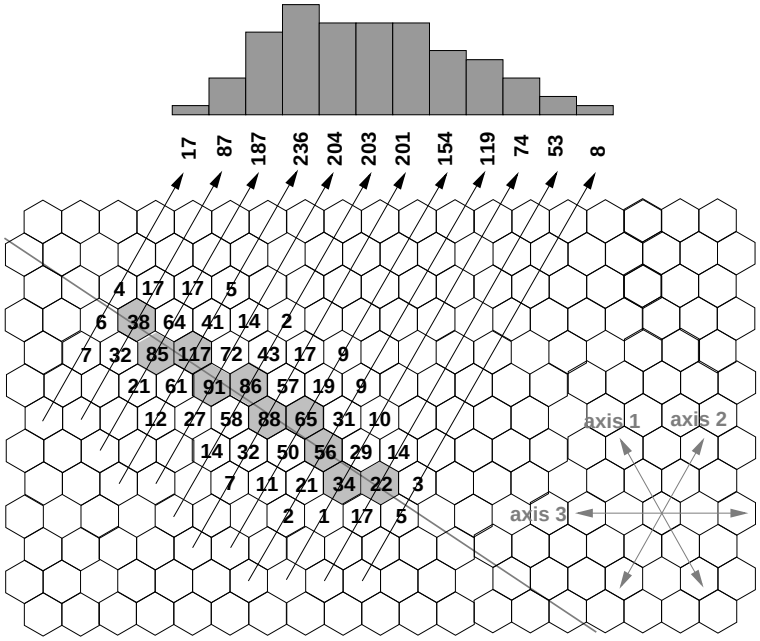

Figure 3.14: *Charge profile computation. The numbers represent the collected charge in each pad. Grey pads correspond to maximum charges.*

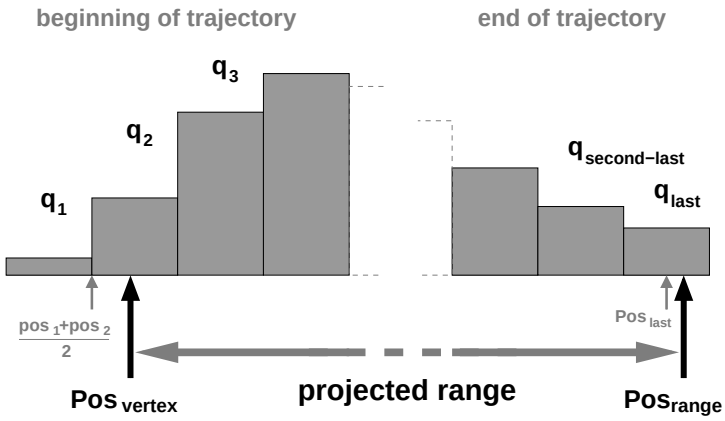

Figure 3.15: *Projected range calculated as the distance between the position of the reaction vertex (Pos_{vertex}) and the end position (Pos_{range}). Both positions are estimated with the first and last charges in the calculated charge profile.*

with

$$CoG_{range} = \frac{\delta q_{last} - \delta q_{second-last}}{\delta q_{second-last} + \delta q_{last}} \tag{3.12}$$

When tested with simulated events, these formulas provided a resolution of ∼1 mm in the starting and ending point positions. The projected range is calculated as the distance between these points:

$$R_{2d} = \text{abs}[Pos_{range} - Pos_{vertex}] \tag{3.13}$$

and the resulting associated resolution is $dR_{2d} = \sqrt{1^2 + 1^2}$ mm. Projected ranges lower than 5 mm are rejected in our analysis, as well as those events with projected ranges reaching the detector edges[14].

The range is extracted from the projected range and the measured θ_{2d} and ϕ angles (see Figure 3.11) with:

$$R = R_{2d}\sqrt{1 + \tan^2\phi \sin^2\theta_{2d}} \tag{3.14}$$

The associated error for the range calculation depends on the error of the ϕ and θ_{2d} calculations and on the projected range (R_{2d}) determination (see Appendix A.1).

The translation from range to energy is calculated with the TRIM code[Zie99][Sri05]. The range and energy of ^{13}N isotopes given by TRIM are plotted in Figure 3.16. The code predictions are then fitted to a second-order polynomial function, which makes it possible to establish the parameters for ^{13}N isobutane at 30 mbar and 26 mbar as:

$$E = -2.70 + 12.00 \cdot 10^{-2}(R) - 1.04 \cdot 10^{-4}(R)^2 \quad \text{for 30 mbar} \tag{3.15}$$
$$E = -2.67 + 10.25 \cdot 10^{-2}(R) - 0.79 \cdot 10^{-4}(R)^2 \quad \text{for 26 mbar} \tag{3.16}$$

Finally, the uncertainty associated with the energy calculation is determined as a function of the pressure uncertainty, which is estimated at 10 %, and the precision of the TRIM code, which is around ∼3 % [Zie99]. See Appendix A.1 for calculation details.

[14] ($R_{2d} \geq 5$ mm) ∧ (not reaching the limits of the cathode plane) in Table 3.1.

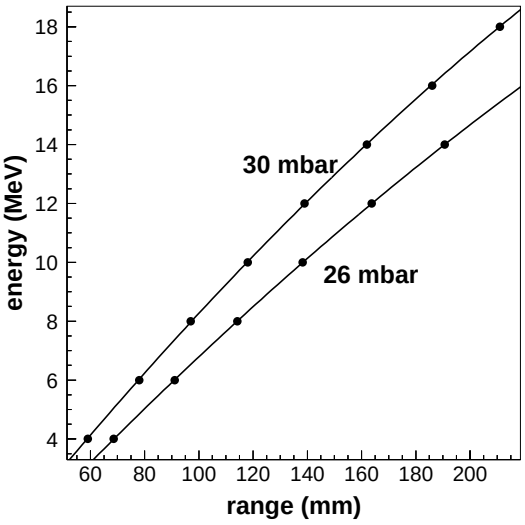

Figure 3.16: *Energy of the ^{13}N plotted versus range calculated with the TRIM code for the two pressures used in the experiment.*

3.2.4 Detection efficiency

The detection efficiency expresses the probability of that an experimental setup will detect a certain event. In our case, the positive detection of an event indicates a fully reconstructed reaction in which the drift time was correctly measured, the amplification wires signal worked well, and the trajectory was properly fitted in the cathode pads. For our purposes, the detection efficiency for a binary reaction is defined as:

$$\varepsilon_{detection} = \frac{N_{reconstructed}}{N_{CsI+3\ wires}} \tag{3.17}$$

$N_{reconstructed}$ is the number of fully reconstructed events, and $N_{CsI+3\ wires}$ the number of events where one particle was detected in the CsI wall and at least three wires fired. This definition does not take into account those events with failures in the CsI and/or in the wires. Failures in the CsI detectors are assumed to be relatively rare for the energies studied in this experiment. Failures in the wires are very rare, and very likely never occur in more than one wire at a time.

The detection efficiency $\varepsilon_{detection}$ was computed for all stored data, and for each CsI detector separately. The result was not constant for all the CsI, revealing a

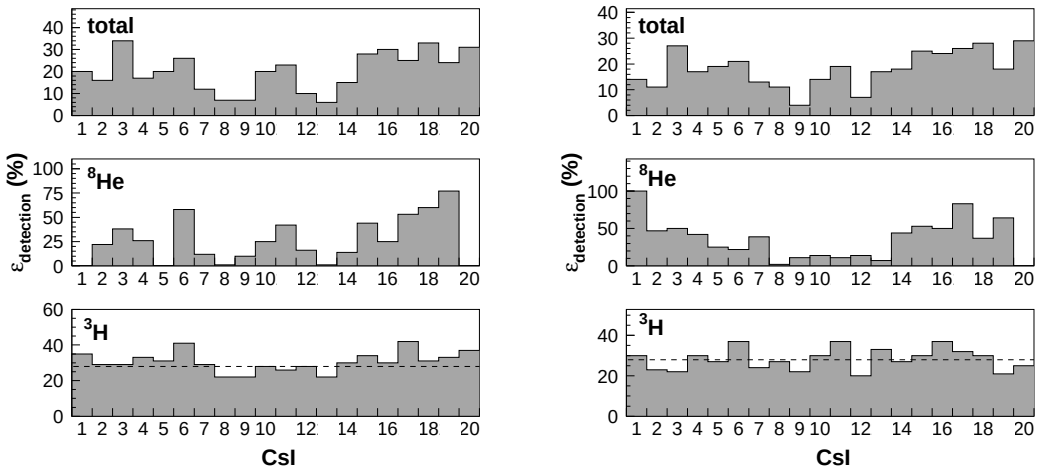

Figure 3.17: *$\varepsilon_{detection}$ efficiency for each fired CsI calculated for the 30 mbar setup in the left panels, and for the 26 mbar setup in the right panels. The upper panels show the calculation with no selection of particles detected in the CsI, the central panels correspond to calculation where ^{8}He particles were selected and the lower panels represent calculations where events with one tritium detected in the CsI were selected. The dashed lines mark the resulting $\varepsilon_{detection}$ value.*

possible kinematic angular dependence, that changes when the contribution from the different particles detected in the CsI is separated. The efficiency $\varepsilon_{detection}$ calculated for those events where ^{8}He is detected in the CsI wall is highly dependent on the position of the CsI detector, but when $\varepsilon_{detection}$ is calculated for those events with a triton detected in the CsI wall the dependence smoothly vanishes and the curve becomes almost flat (see Figure 3.17).

The $\varepsilon_{detection}$ calculation for the two pressures of the filling gas used in MAYA reveals any dependence on the pressure. For events with tritium detected in the CsI wall, which are the events of interest in this study, the detection efficiency was calculated to be $\varepsilon_{detection} = 28 \pm 0.3$ %. All the geometrical filters described in previous sections are included in the reconstruction, which decreases the final value of the efficiency. This decrease is primarly due to the rejection of those events with a reaction plane angle $|\phi|$ greater than 60 deg, which means a reduction of $\varepsilon_\phi \simeq 67$ %, if we assume an isotropic distribution of ϕ.

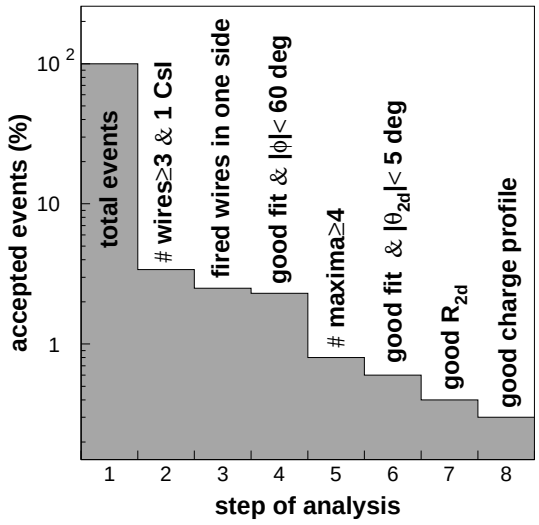

Figure 3.18: *Percentage of accepted events in the analysis after each filter is applied. Notice the logarithmic scale. For explanation of the filters see Table 3.1.*

Review of the analysis filters

The detection efficiency $\varepsilon_{detection}$ is strongly affected by the filters applied during the data analysis, which have been explained in this chapter. Table 3.1 summarizes the main filters used and Figure 3.18 shows how the number of accepted events is reduced as the analysis progresses[15].

3.3 Normalization to Target Thickness and Incident Projectiles

The probability that a given reaction occurs is valuable information for characterizing the reaction. The number of detected reactions is corrected with the detection efficiency, and normalized to the number of nuclei in the target and incident projectiles in order to obtain the associated cross-section. This makes the study less dependent on the experimental conditions and makes it possible to compare the results with other experimental setups.

[15]the percentage of accepated events is calculated respect to the total number of events recorded, therefore is not a measurement of the detection efficiency

analysis step	*filter*
CsI wall	only one particle detected
anode wires	$\#\text{wires}_{\text{total}} \geq 3$ $[(\#\text{wires}_{\text{right}} > 2) \wedge (\#\text{wires}_{\text{left}} < 2)] \vee [(\#\text{wires}_{\text{left}} > 2) \wedge (\#\text{wires}_{\text{right}} < 2)]$ $\lvert\phi\rvert < 60$ deg
projected range	$\#\text{maxima} > 4$ $\lvert\theta_{2\text{d}}\rvert \geq 5$ deg $(\text{R}_{2\text{d}} \geq 5$ mm$) \wedge$ (not reaching the limits of the cathode plane)
charge profile	$\text{q}_{\text{last}} \leq \text{q}_{\text{second-last}}$ $(\delta\text{q}_0 > 0) \wedge (\delta\text{q}_1 > 0)$

Table 3.1: *Summary of the main filters applied in the different steps of the analysis. The notation is the following:* $\#wires_{total}$ *is the total number of fired anode wires,* $\#wires_{right}$ *and* $\#wires_{left}$ *are the number of fired wires in the right and left side of the projection plane,* $|\phi|$ *is the modulus of the reaction plane angle* ϕ*,* $\#maxima$ *is the number of maxima of charge found in the cathode pads,* $|\theta_{2d}|$ *is the modulus of the projected angle* θ_{2d} *of the trajectory with respect to the beam direction,* R_{2d} *is the projection of the particle range,* q_{last} *and* $q_{second-last}$ *are the two last components of the charge profile, and finally,* δq_0 *and* δq_1 *are the first components of the numerical derivative of the charge profile*

Target thickness normalization

For this study, two experimental setups were used in MAYA, with two different gas pressures, 26 mbar and 30 mbar. This resulted in two target thicknesses, with different numbers of ^{12}C nuclei, $N_{^{12}\mathrm{C}}$, calculated as:

$$N_{^{12}\mathrm{C}} = D_{isobutane} \cdot L \cdot R_C \cdot N_A \cdot A^{-1}_{isobutane} \tag{3.18}$$

where $D_{isobutane}$ is the density of isobutane for each pressure[16], $7.3{\cdot}10^{-5}$ g/cm^3 for 30 mbar, and $6.3{\cdot}10^{-5}$ g/cm^3 for 26 mbar, both with an associated error of 10 % (see Section 3.2.3). L is the usable length of the detector. The geometry of MAYA makes it impossible to detect reactions where the vertex is close to the CsI wall, because the recoil products from such reactions may have enough energy to leave the active area and hit the back of MAYA. The usable length of the detector is defined as the distance from this point to the detector entrance. When determining the usable length the expected recoil angle and energy for the reaction are taken into consideration. The usable length also depends on the gas pressure, because of the range and energy relation. Estimated lengths are $L = 10.5$ cm for 30 mbar and $L = 11.5$ cm for 26 mbar of isobutane, with $\sim$5 % of uncertainty in both cases. R_C is the number of Carbon atoms in the isobutane (C_4H_{10}) molecule. The mass of the molecule is $A_{isobutane} \simeq 4 \cdot 12 + 10 \cdot 1$ g^{-1}mol. The Avogadro constant is $N_A = 6.022 \cdot 10^{23}$ mol^{-1}.

The resulting number of ^{12}C targets is $N_{^{12}\mathrm{C}} = 3.22 \cdot 10^{19}$ cm^{-2} for 30 mbar of gas, and $N_{^{12}\mathrm{C}} = 3.01 \cdot 10^{19}$ cm^{-2} for 26 mbar. The associated error for both quantities is $\sqrt{(10\ \%)^2 + (5\ \%)^2}\ \simeq\ 11\ \%$ (see Equation A.18 in Appendix A.1).

Number of incident projectiles normalization

The total number of ^{8}He projectiles entering MAYA is estimated using the signals recorded from the *Monitoring Drift Chambers* (MDC). The number of beam triggers (T_{beam}) is multiplied by the division factor (f_{BiDiv}) of the BiDiv module (see Sections 2.2.2 and 2.3), and corrected by the detector efficiency (ε_{MDC}), in order to get the total number of detected projectiles. The number of lost projectiles between the MDC and the MAYA entrance due to beam alignment or other circumstances is estimated to be $\alpha_{beam} = 2 \pm 2$ %[17]. The number of projectiles ($N_{^8\mathrm{He}}$) is then:

[16] room temperature

[17] checked with a 15.4A MeV ^{16}O beam.

$$N_{^8\mathrm{He}} = \frac{T_{beam} \cdot f_{BiDiv}}{(1 - \alpha_{beam}) \cdot \varepsilon_{MDC}} \tag{3.19}$$

With an estimated monitor module efficiency of $\varepsilon_{MDC} = 85 \pm 1$ % (see Section 3.1.2), the results are $N_{^8\mathrm{He}} = (7.22 \pm 0.20) \cdot 10^9$ for 30 mbar, and $N_{^8\mathrm{He}} = (3.04 \pm 0.09) \cdot 10^9$ for 26 mbar (see Appendix A.1 for details about the uncertainty calculations).

Chapter 4

Results. Experimental Finding of the ^{7}H Resonance

"Too much of nothing can make a man feel ill at ease" (Bob Dylan)[1]

The purpose of this chapter is to address the selection of those events where the ^{7}H system was produced using the identification of the light scattered particle in the CsI and the reconstruction of the reaction kinematics of the recoil particle stopped in the filling gas of MAYA.

The production of ^{7}H is characterized as a Breit-Wigner resonance, and the energy and width of the resonance are determined from this characterization. The fitting process is also explained in this section, along with the calculation of the reaction cross section, which is the last observable used to characterize the ^{7}H resonance.

4.1 Selection of ^{7}H Resonance Reaction Events

The search of events in which the ^{7}H state was produced begins with the reaction channel selection process. A first selection is made when the particle stopped in the CsI wall is identified as a tritium and the recoil particle stopped in the filling gas of MAYA is identified as a Nitrogen isotope. When this occurs, the associated ^{3,4,5,6,7}H channels are selected. Those events cumulating around the kinematics of the ^{12}C(^{8}He,^{3}H+4n)^{13}N reaction channel are identified as ^{7}H events. The selection

[1] provided by Mr. Catford

is completed with the calculation of the excitation energy associated with the reaction, where events identified as ^{7}H resonances form a peak in the excitation energy spectrum. This production probability enhancement is considered the signature of a well-defined resonant state.

4.1.1 Identification of the ^{7}H reaction channel

Events that pass through all the filters applied in the first part of the analysis are considered to be binary reactions. This selection includes all possible reaction channels where a light scattered particle escapes from the detector, and a recoil particle is stopped in the filling gas. Identification of the scattered and recoil particles makes it possible to select the production of ^{7}H among other reaction channels.

Selection by identification of tritium in the CsI detectors (see Figure 3.6) reduces the possible channels to those producing ^{3,4,5,6,7}H isotopes. This selection is not exclusive to the one-proton channel, and other reactions apart from the one-proton transfer can produce Hydrogen isotopes and a recoil product stopped in the gas. Fragmentation reactions of the ^{8}He projectile or fusion-evaporation of ^{20}O can simulate a binary reaction if all the products are not detected. In order to clean up the selection, we select only Nitrogen isotopes from among the recoil products.

The Nitrogen selection uses the unique relation that links the energy and range for a certain isotope in a given gas. The left panel of Figure 4.1 displays this relation for the different isotopes expected in this experiment: Nitrogen, Carbon, and Boron, which were evaluated with the SRIM code[Sri05]. In addition, it is possible to establish a relation between the collected charge and the calculated range for an isotope stopped in the gas, since the total collected charge is proportional to the energy deposited (see Section 2.2.3). The right panel in Figure 4.1 shows the experimental range versus the collected charge. The most intense area in the middle of the plot is formed with Carbon isotopes produced mainly in elastic and inelastic scattering with the ^{12}C targets. The upper part of the graph corresponds to lighter isotopes, such as Boron or Beryllium, whereas the lower part, clearly separated by the Carbon line, corresponds to Nitrogen isotopes[2]. The Lower right pannel shows the same graph with data gated by the identification of ^{3}H particles in the CsI detectors.

With this setup is not possible to identify the different Nitrogen isotopes. The small differences in range and the large uncertainty associated with the collected charge, along with the low statistics, blur the isotopic lines of the range versus charge plot. Therefore this selection includes all Nitrogen isotopes produced in any

[2] the heaviest element we can produce within this setup.

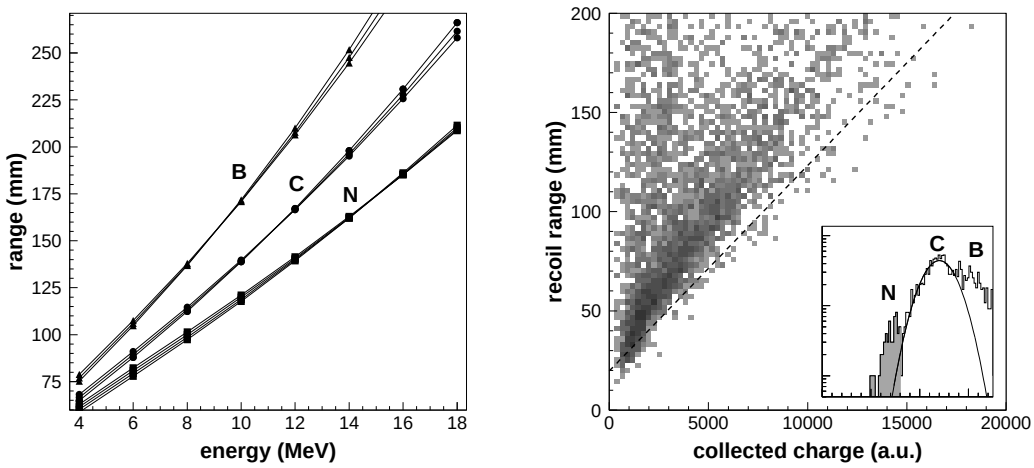

Figure 4.1: *Left panel: range versus energy, as predicted by the SRIM code, for different isotopes expected in the experiment. Right panel: Nitrogen selection in the experimental range versus charge plot. The inset shows the Nitrogen selection in full grey histogram in isotopic projection.*

of the ^{3,4,5,6,7}H reaction channels.

The energy of the recoil particle is estimated from its range inside the gas. This translation depends on the type of particle. Since it is not possible to distinguish between different Nitrogen isotopes, the different reaction channels cannot be observed at the same time. To overcome this problem, the range-energy relation of the corresponding recoil isotope is used to look at a specific reaction channel.

Figure 4.2 shows the relation between the energy and the scattered angle (θ) of the recoil product for the filtered events. This relation describes the kinematics of a particle for a selected reaction channel. The kinematics corresponding to the formation of ^{3,4,5,6,7}H are calculated for the ^{17,16,15,14,13}N recoils and plotted in the left panel of Figure 4.2. In the case of the ^{7}H resonance the kinematics line is calculated assuming a rest mass for the ^{7}H system equal to the sum of the mass of tritium and four neutrons, $m^{0}_{^{7}\mathrm{H}} = m_{^{3}\mathrm{H}} + 4m_{n}$. The lines corresponding to ^{6,5}H resonances were also calculated assuming a mass equal to the subsystems of tritium and the corresponding neutrons.

The main result of this work can be seen in Figure 4.2 and more clearly in Figure 4.3. Some points appear beyond the line corresponding to the ^{6}H kinematics. These points cumulate clearly around the kinematics line corresponding to the production of ^{7}H, which is the first positive experimental observation of the ^{7}H resonance. The

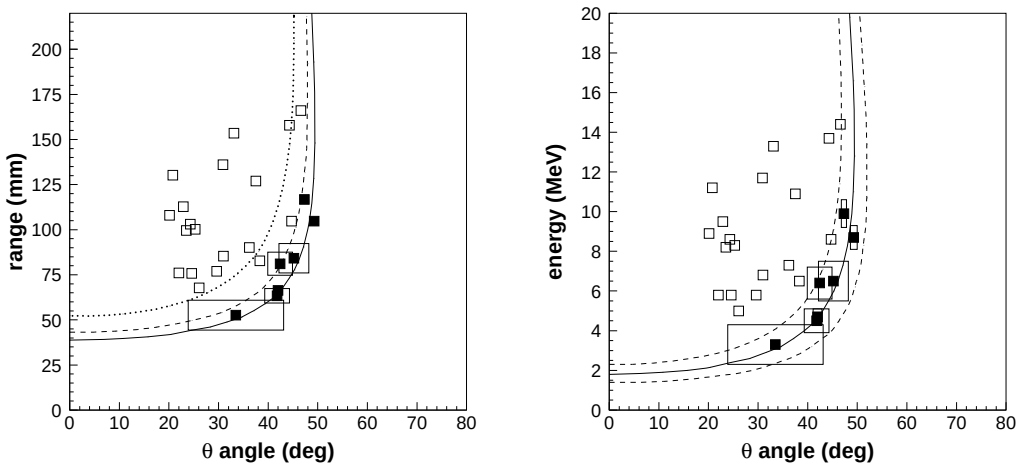

Figure 4.2: *Left panel: kinematics of different reaction channels plotted with the full filtered data. The solid line corresponds to ^7H, the dashed line for ^6H and the dotted line for ^5H. Right panel: dashed lines show a ±4 MeV region around the ^7H kinematics. The solid squares in both panels correspond to the ^7H candidates (see Section 4.1.3) with their corresponding uncertainty areas.*

candidates for ^{7}H resonance events are selected from within the area defined by the two lines corresponding to the kinematics of the ^{12}C(^{8}He,^{3}H+4n)^{13}N reaction with $m^0_{^7\mathrm{H}}$ modified +4 and -4 MeV respectively (see Section 4.1.3), which can be seen in Figure 4.2.

4.1.2 Calculation of the excitation energy

The production of ^{7}H is characterized as a peak in the production cross section around a certain value of the excitation energy (E^{exc}). The excitation energy is defined as the difference between the mass of the resonance ($m_{^7\mathrm{H}}$) and the rest mass of the components ($m_{^3\mathrm{H+4n}}$):

$$E^{exc} = m_{^7\mathrm{H}} - m_{(^3\mathrm{H+4n})} \tag{4.1}$$

The resonance energy corresponds to the energy needed to hold the system together for a certain amount of time (life-time). The calculation of E^{exc} is done by means of the conservation of energy and momentum (see Appendix B). Its applica-

tion to the ^{7}H reaction can be summarized as:

$$|\vec{p}_{^{7}\mathrm{H}}|^2 = |\vec{p}_{^{8}\mathrm{He}}|^2 + |\vec{p}_{^{13}\mathrm{N}}|^2 - 2|\vec{p}_{^{8}\mathrm{He}}||\vec{p}_{^{13}\mathrm{N}}|\cos\theta \tag{4.2}$$

with θ the angle between the projectile and recoil particles.

$$m^2_{^{7}\mathrm{H}} = (E_{^{8}\mathrm{He}} + E_{^{12}\mathrm{C}} - E_{^{13}\mathrm{N}})^2 - |\vec{p}_{^{7}\mathrm{H}}|^2 \tag{4.3}$$

with

$$\begin{aligned} E_{^{8}\mathrm{He}} &= (m_{^{8}\mathrm{He}} + T_{^{8}\mathrm{He}}) && (4.4)\\ E_{^{12}\mathrm{C}} &= m_{^{12}\mathrm{C}} && (4.5)\\ E_{^{13}\mathrm{N}} &= (m_{^{13}\mathrm{N}} + T_{^{13}\mathrm{N}}) && (4.6)\\ & && (4.7) \end{aligned}$$

Finally, E^{exc} is obtained by applying the calculated $m_{^{7}\mathrm{H}}$ in Equation 4.1. The quantities $\cos\theta$, $|\vec{p}_{^{13}\mathrm{N}}|$, and $T_{^{13}\mathrm{N}}$ are experimentally determined with MAYA (see sections 3.2.2 and 3.2.3). The projectile momentum and energy values, as well as the different masses are known (see reference [Wap03]):

$$\begin{aligned} m_{^{8}\mathrm{He}} &= 7483.53 \text{ MeV}\\ m_{^{12}\mathrm{C}} &= 11177.93 \text{ MeV}\\ m_{^{13}\mathrm{N}} &= 12114.73 \text{ MeV}\\ m_{(^{3}\mathrm{H}+4\mathrm{n})} &= 6567.78 \text{ MeV} \end{aligned}$$

$$\begin{aligned} T_{^{8}\mathrm{He}} &= 122.63 \text{ MeV}\\ |\vec{p}_{^{8}\mathrm{He}}| &= 1360.31 \text{ MeV} \end{aligned}$$

The energy value of the secondary beam of ^{8}He ($T_{^{8}\mathrm{He}}$) includes the energy lost in the detectors and the entrance window of MAYA (see Section 2.2).

The uncertainty associated with E^{exc} depends on the energy of the ^{13}N recoil, its θ angle with respect to the projectile, and the energy spread of the beam ($dT_{^{8}\mathrm{He}}$, estimated to be $\pm$ 0.5 % [Jac03] for a CIME beam in Spiral [Jac03]). See Appendix A.2 for details of the uncertainty calculation.

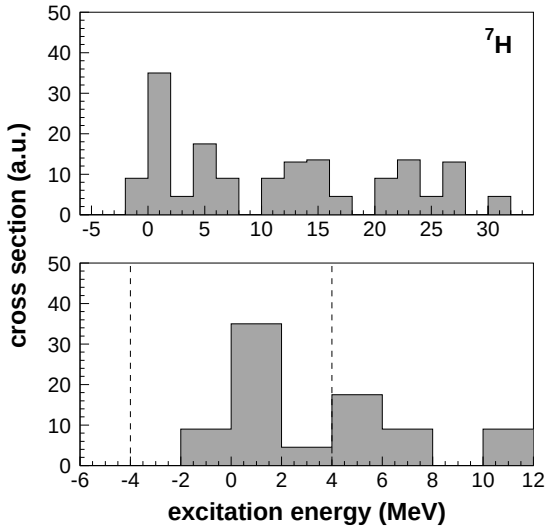

Figure 4.3: *Excitation energy spectra as calculated for the ^{7}H reaction channel. The lower panel shows the ±4 MeV region where the ^{7}H events are expected.*

4.1.3 Identified ^{7}H events

In order to unambiguously identify ^{7}H events, we distinguish different reaction channels within the filtered data. Figures 4.3, 4.4 and 4.5 show the excitation energy (E^{exc}) spectra for the ^{7,6,5}H channels. These spectra were calculated by applying the E^{exc} formula 4.1 to each transfer channel ^{12}C(^{8}He,^{7}H)^{13}N, ^{12}C(^{8}He,^{6}H)^{14}N, and ^{12}C(^{8}He,^{5}H)^{15}N.

The excitation energy calculation (Figure 4.3) assumes one-proton transfer channel ^{12}C(^{8}He,^{7}H)^{13}N. The events represented correspond to those cases where a ^{3}H particle was detected in the CsI wall, and a Nitrogen isotope was stopped in the filling gas, as in Figure 4.2. The peak close to the limit of the ^{3}H+4n mass corresponds to those points cumulated around the line of the ^{12}C(^{8}He,^{3}H+4n)^{13}N reaction kinematics. The expected ^{7}H events are likely to lie in a region below 4 MeV (dashed lines in Figure 4.3), since for higher energy other transfer channels begin to appear. Seven points around the peak are identified as ^{7}H reactions. These events, with their associated uncertainties, are reviewed in table 4.1 (see Appendix A for uncertainties estimation).

Since the applied selections do not exclude the formation of other heavy Hydrogen isotopes, we also expect to see events corresponding to the formation of

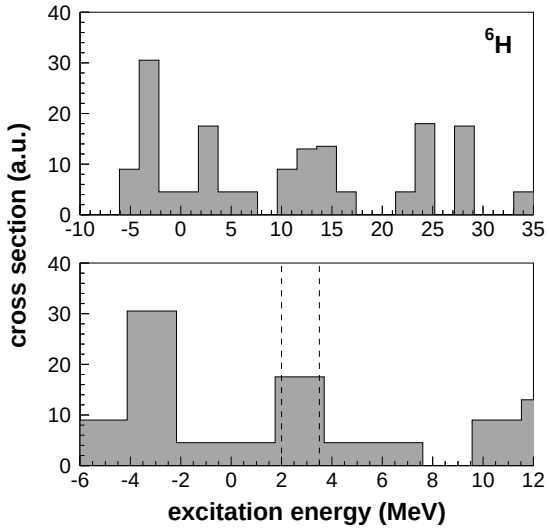

Figure 4.4: *Excitation energy spectra as calculated for the ^{6}H reaction channel. The lower panel shows the 1-3 MeV region where the ^{6}H events are expected, according to [Ale84] and [Bel86].*

^{6}H, and ^{5}H. The ^{6}H resonance is expected to appear mainly in the 2 MeV region around 2.7 MeV [Ale84] and [Bel86]. The excitation energy spectrum is calculated to correspond to the ^{12}C(^{8}He,^{6}H)^{14}N reaction where ^{6}H is produced. Figure 4.4 gives indications of events cumulating in a 2 MeV region around 2.7 MeV which are consistent with the results of [Ale84] and [Bel86].

Equivalent treatment associated with the formation of ^{5}H in the ^{12}C(^{8}He,^{5}H)^{15}N reaction can be seen in Figure 4.5. However, comparison with previous works ([Gol05] or [Mei03a], for example) offers less clarity. The experimental discrepancy among those works makes it necessary to give a relatively large excitation energy interval for the position of the ^{5}H resonance. In addition, this large energy region may also be populated with phase-space events associated with the ^{6}H, and ^{7}H channels, which makes the analysis more difficult.

In our experiment, ^{6}H is formed by the transfer of one proton and one neutron from the ^{8}He projectiles to the ^{12}C targets, whereas the formation of ^{5}H requires the transfer of one more neutron. The probability of transfering two particles is, in principle, greater than that of transfering three particles. Figures 4.4 and 4.5 the ^{6}H appears with presumably lower statistics than ^{5}H[3]. The reasons may lie in

[3]in any case, the ^{5}H is placed in a region where phase space effects from ^{7}H and ^{6}H may contribute to increasing its statistics (see Section 4.1.4).

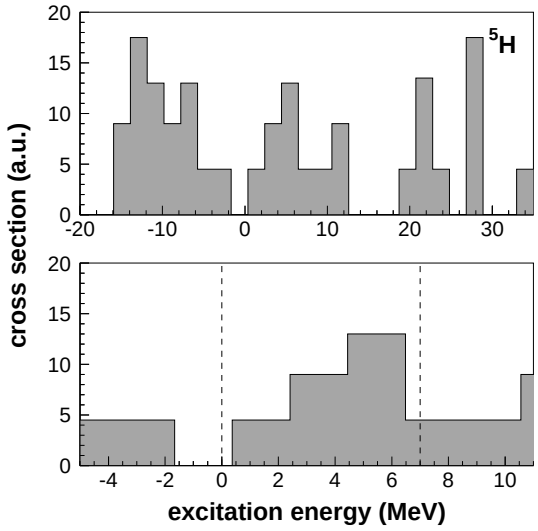

Figure 4.5: *Excitation energy spectra as calculated for the ^5H reaction channel. The lower panel shows the 0-6 MeV region where the ^5H events are expected, according to [Gol05] and [Mei03a].*

the neutron-neutron interaction, which favors the formation of Hydrogen isotopes with an even number of neutrons. This effect appears in many of the theoretical descriptions, such as [Tim04] or [Aoy04].

Another factor affecting the probability of formation is the energy of reaction. More than 21 MeV[4] are needed to produce the ^{7}H resonance, whereas for ^{6}H the energy required is close to 13 MeV[5]. The energy required to produce ^{5}H is much less, close to 1 MeV[6]. In addition, the different angular regions covered by each reaction kinematics inside MAYA produce different yields the corresponding reaction.

A histogram is inadequate to represent the excitation energy spectrum with low statistics. Moreover, the uncertainty associated with each event is individually computed and results in different values, making a common histogram binning unrealistic. We exchanged the histogram for a non-binning spectrum, where each experimental point contributes to the spectrum as a Gaussian distribution centered in the measured value, with a variance σ equal to its estimated uncertainty. The resulting spectrum is shown in Figure 4.6 for the identified ^{7}H events.

[4]calculated as $m_{(^{12}C+^8He)} - m_{(^{13}N+^3H+4n)}$.
[5]calculated as $m_{(^{12}C+^8He)} - m_{(^{14}N+^3H+3n+E_R(^6H))}$ with $E_R(^6H) \simeq 2.6$ MeV from [Bel86].
[6]calculated as $m_{(^{12}C+^8He)} - m_{(^{15}N+^3H+2n+E_R(^5H))}$ with $E_R(^5H) \simeq 1.7$ MeV from [Gol05].

$\mathbf{T}(^{13}\mathbf{N})$ MeV	$\theta_{\mathbf{lab}}$ deg	$\mathbf{E^{exc}}$ MeV	$\mathbf{dE^{exc}}$ MeV
3.33±0.95	33.54±9.63	**0.99**	**6.94**
6.36±0.80	42.42±2.51	**3.32**	**2.82**
9.89±0.67	47.35±0.51	**1.92**	**0.78**
8.73±0.61	49.32±0.73	**−1.37**	**1.02**
4.49±0.55	41.77±2.50	**−0.40**	**2.52**
4.72±0.44	42.05±0.90	**0.00**	**1.38**
6.54±0.97	45.21±2.97	**0.88**	**3.40**

Table 4.1: *Experimental events identified as reactions in which the ^7H resonance was produced.*

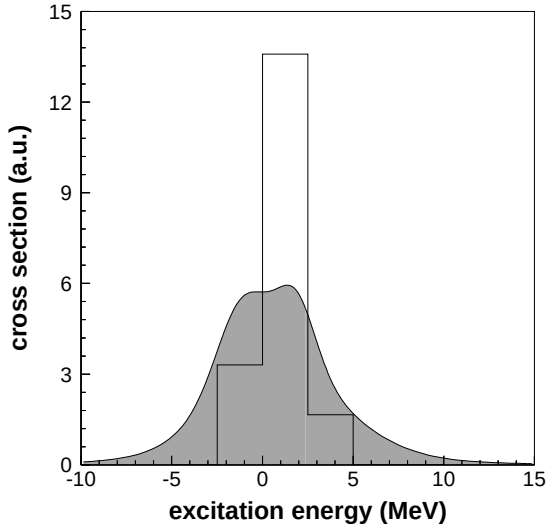

Figure 4.6: *Excitation energy of the identified ^7H events. The empty histogram is plotted with 2.5 counts/MeV, corresponding to the mean uncertainty as calculated from Table 4.1. In the solid distribution each event contributes a Gaussian distribution centered around the measured E^{exc} value, and with a variance equal to the estimated uncertainty. Both the histogram and the distribution are normalized to the number of projectiles and atoms in the target, and corrected with the detection efficiency $\varepsilon_{detection}$.*

4.1.4 Phase-space considerations

In the selection of a resonance production channel, there are always other events found that have the same particles in the final state, but no resonance is produced. This phase-space appears in the excitation energy spectrum as *continuum* background, along with the peak of the resonance, if it exists. In our case, the following reactions may appear in a selection of the ^{3}H+^{13}N channel:

$$^{12}\mathrm{C}\ \left(\ ^{8}\mathrm{He}\ ,\ ^{3}\mathbf{H} + \mathrm{n} + \mathrm{n} + \mathrm{n} + \mathrm{n}\ \right)\ ^{13}\mathbf{N} \qquad (six-body) \tag{4.8}$$

$$^{12}\mathrm{C}\ \left(\ ^{8}\mathrm{He}\ ,\ ^{3}\mathbf{H} +^{2}\mathrm{n} +^{2}\mathrm{n}\ \right)\ ^{13}\mathbf{N} \qquad (four-body) \tag{4.9}$$

$$^{12}\mathrm{C}\ \left(\ ^{8}\mathrm{He}\ ,\ ^{3}\mathbf{H} +^{4}\mathrm{n}\ \right)\ ^{13}\mathbf{N} \qquad (three-body) \tag{4.10}$$

$$^{12}\mathrm{C}\ \left(\ ^{8}\mathrm{He}\ ,\ ^{7}\mathrm{H} \rightarrow\ ^{3}\mathbf{H} + 4\mathrm{n}\ \right)\ ^{13}\mathbf{N} \quad resonance\ production\ (two-body) \tag{4.11}$$

The first equation corresponds to the expected case where the $^{8}He - p$ system splits into a stable ^{3}H and four neutrons. The second case expresses a possible formation of two dineutron clusters, which decay into four separate neutrons, preserving the tritium and the Nitrogen a four-body correlation. The third equation represents the extreme case in which a tetraneutron system is formed, that yields a three-body *continuum*. The fourth equation expresses the formation of a resonance, ^{7}H in our case, that results in a final two-body correlation. The extreme cases of six-body and three-body *continuum*s are plotted in Figure 4.7.

In each case, the *continuum* distributions were computed according the total energy and momentum conservation. In each individual event of the distribution, the total energy available in the reaction is randomly distributed among the reaction products. Once the energy is assigned, the particle trajectory angles are also randomly assigned until the total momentum conservation is assured.

Before calculating the excitation energy of each event, a series of filters and cuts are applied to reproduce the analysis conditions. These conditions include a Nitrogen recoil energy between 2 MeV and 15 MeV, with angles greater than 5 deg, and a ^{3}H scattered energy greater than 30 MeV, with angles lower than 90 deg.

The resulting six-body and three-body *continuum*s are compared with the experimental distribution of excitation energy in Figure 4.8. None of the *continuum*s, not even the most extreme three-body distribution associated with the tetraneutron formation, explain the peak associated with the ^{7}H resonance.

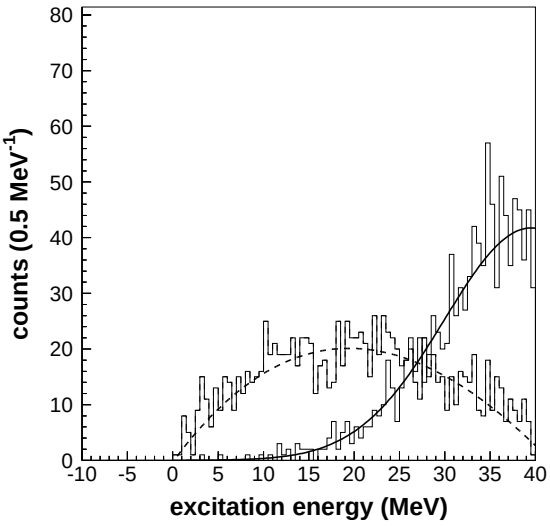

Figure 4.7: *Normalized excitation energy distributions for six-body (solid line) and three-body (dashed line) continuums.*

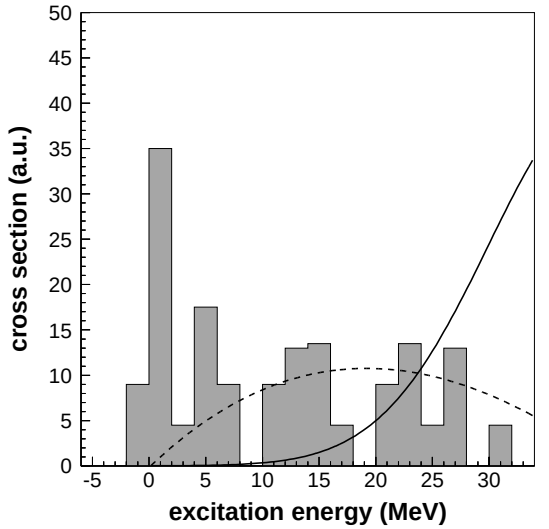

Figure 4.8: *Experimental excitation energy distribution compared with six-body (solid line) and three-body (dashed line) continuums normalized to the experimental yield.*

The calculations of the phase-space associated with ^{6}H and ^{5}H channels lead to similar distributions, shifted to higher energies above their associated thresholds. The main consequence of this behaviour is that the ^{7}H resonance peak can only be affected by its own phase space. The most probable contribution, in the case of ^{7}H, comes from the six-body *continuum*, which begins to appear around 20 MeV above the ^{3}H+4n threshold. This assures a ^{7}H peak, around the ^{3}H+4n threshold, almost undisturbed by the phase-space effect.

4.2 Characterization of the ^{7}H Resonance

This section is devoted to the characterization of the ^{7}H resonance. The physical parameters that identify the resonant state, such as its energy and life-time, are extracted from the fit of the excitation energy spectrum of events identified as ^{7}H to a modified Breit-Wigner function. The first part of this section describes the modifications to the standard Breit-Wigner function. The fitting process using the *Maximum Likelihood* procedure is detailed in the last part of this section, with special attention to the case of extremely low statistics.

4.2.1 Modified Breit-Wigner function

The ^{7}H resonance is characterized by means of a fit to a Breit-Wigner function. This is a generalized distribution form originally intended to describe the cross section of resonant nuclear scattering [Bre36], and derived from the transition probability of a resonant state with a known lifetime:

$$\sigma_{BW}(E) = \frac{\Gamma}{2\pi(E - E_R)^2 + (\Gamma/2)^2} \tag{4.12}$$

Where $\sigma_{BW}(E)$ is the probability of producing the resonance, which is maximal when the energy is equal to E_R. The width of the distribution is governed by the parameter Γ, which also contains information about the lifetime of the resonance through the Heisenberg relation $\tau\Gamma \geq \hbar$.

Γ depends on the probability that the reaction wave will emerge promptly. This probability is normally reduced by the angular momentum and Coulomb barriers. The effect of these barriers is practically independent of the nuclear interaction but depends critically on the energy and size of the system. In the case of the Coulomb

barrier it also depends on the charges of the target and projectile involved. These effects can produce a strong dependence of Γ [Fes74] on the energy of the system.

We assume that the effect of the Coulomb barrier is dominant in the formation of the resonance due to the proton transfer from the ^{8}He projectile to the ^{12}C target. The target and projectile charges, as well as their energies, are fixed in our experimental setup, therefore the Coulomb barrier effect does not produce noticeable changes in Γ with the resonance energy.

The next stage of the resonance is its decay. We attributed a neutron emission decay for the ^{7}H. The neutrons should traverse the angular momentum barrier to leave the potential well with a probability that depends on the energy of the ^{7}H compound. This effect is simplified with Γ depending on its probability as[7]:

$$\Gamma = \Gamma_0 \frac{P_l(E)}{P_l(E_R)} \tag{4.13}$$

where Γ_0 is the reduced width, and $P_l(E)$ the penetrability of the barrier for an energy E. In the case of the angular momentum barrier, the penetrability is proportional to the square root of the energy, $P_l(E) \propto \sqrt{E}$, resulting in[8]:

$$\Gamma = \Gamma_0 \sqrt{\frac{E}{E_R}} \tag{4.14}$$

The reduced width (Γ_0) includes both partial constant widths: the constant dependence on the Coulomb barrier and the constant factors of the angular momentum barrier $\Gamma_0 \equiv \Gamma^{Coulomb}\Gamma_0^{angular}$.

The Breit-Wigner function in Form 4.12 is a normalized distribution. In order to account for the probability of the reaction we include a normalization factor, σ_0, which yields an integral value of the Breit-Wigner distribution equal to the reaction cross section.

With these modifications, the Breit-Wigner distribution used in this work for characterizing the ^{7}H resonance is expressed as:

[7] the same approximation is also used, for instance, in reference [Boh01].
[8] however, other parameterizations are possible, see Section 4.2.2.

$$\sigma_{BW}(E) = \sigma_0 \frac{\Gamma_0 \sqrt{\frac{E}{E_R}}}{(E - E_R)^2 + \left(\frac{\Gamma_0}{2}\sqrt{\frac{E}{E_R}}\right)^2} \tag{4.15}$$

4.2.2 Data fitting procedure

We assume that the experimental ^{7}H events follow the Breit-Wigner distribution presented in the previous section. The resonance energy (E_R) and width (Γ_0) parameters of this distribution were extracted from the fit of the excitation energy spectrum. The fit was done following a *Maximum Likelihood* procedure, which maximizes the associated probability of measuring a set of experimental points, by varying the parameters of the given probability density function. The *Maximum Likelihood* procedure computes the probability for each event separately, taking into account each associated uncertainty, as in Equations 4.16 and 4.17. This feature is especially interesting for low statistics samples, such as those studied in this work.

The associated *Maximum Likelihood* $\mathscr{L}$ can be expressed as:

$$\max[\mathscr{L}] = \max[\prod_{i=1}^{n} P_i] \tag{4.16}$$

where the likelihood $\mathscr{L}$ is the multiplication of the probability P_i of measuring each i for a set of n events. The probability P_i is defined in our case as:

$$P_i = \frac{\int_0^\infty \sigma_{BW}(E^{exc}|E_R, \Gamma_0) \times \mathscr{G}_i(E^{exc}|E_i^{exc}, dE_i^{exc})\ \mathrm{d}E^{exc}}{\int_0^\infty \sigma_{BW}(E^{exc}|E_R, \Gamma_0)\ \mathrm{d}E^{exc}} \tag{4.17}$$

with

$$\mathscr{G}_i(E^{exc}|E_i^{exc}, dE_i^{exc}) = \frac{1}{dE_i^{exc}\sqrt{2\pi}} \exp\left(\frac{-(E^{exc} - E_i^{exc})^2}{2(dE_i^{exc})^2}\right) \tag{4.18}$$

that is: the mathematical convolution of the Breit-Wigner distribution $\sigma_{BW}(E^{exc})$ with parameters E_R and Γ_0, with a normalized Gaussian distribution $\mathscr{G}_i(E^{exc})$ centered in the measured excitation energy E_i^{exc}, and with a variance equal

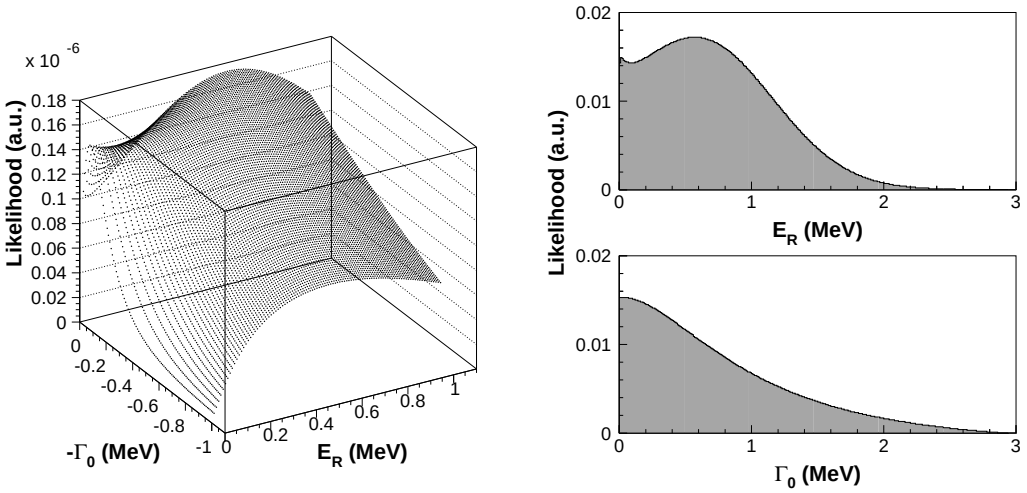

Figure 4.9: *Left panel: $\mathscr{L}$ as a function of E_R and Γ_0. Right panel: projections of $\mathscr{L}$ over E_R and Γ_0. Notice the absence of a maximum in the Γ_0 projection.*

to the associated error dE_i^{exc}. The resulting number is normalized to the integral of the Breit-Wigner distribution.

The largest $\mathscr{L}$ is associated with the set of parameters E_R and Γ_0, which better reproduces the experimental distribution. Notice the absence of the parameter σ_0 in the fitting procedure. This parameter is a fixed value independent of the excitation energy (E^{exc}) and determined by normalization to the cross section (see Section 4.3.2).

The $\mathscr{L}$ quantity is calculated numerically for any pair of values for E_R and Γ_0 with Equation 4.17. The resulting map is plotted in Figure 4.9, with the projections over each parameter. We can distinguish a maximum value in the E_R projection which is defined as the fitted value (E_R^{fit}), in this case corresponding to $E_R^{fit} = 0.63$ MeV. The projection over Γ_0 does not reveal any maximum value, thus there is no assigment to any fitted value of the width (Γ_0^{fit}). This may be due to an overestimation of the uncertainties and indicated that the direct *Maximum Likelihood* fitting could be improved. In order to ensure that proper values for E_R and Γ_0, and to refine the fitting procedure, the sample stability is examined in the next section.

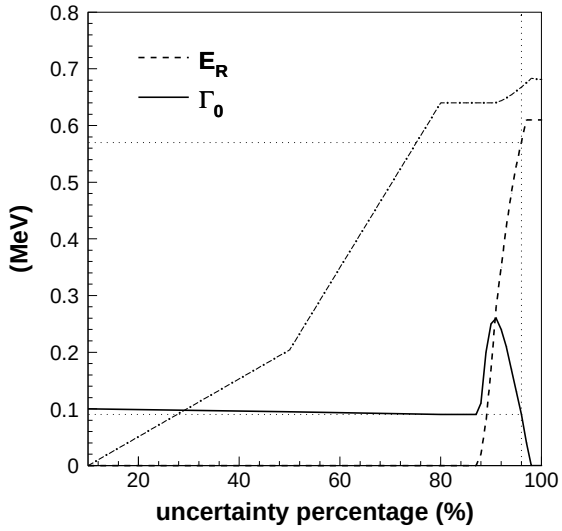

Figure 4.10: *Results of E_R (dashed line) and Γ_0 (solid line) for different factors of the original uncertainties. The dash-dotted line is the calculated $\mathscr{L}$ in arbitrary units. The chosen percentage, along with its corresponding E_R and Γ_0, are marked with thin dotted lines.*

Sample stability

The fitting process reveals the physical distribution that governs the measured data. The results should not depend, in principle, on the amount of data, or on the estimated uncertainties. This information about statistics and experimental uncertainties is contained in the goodness of the fit. We can examine this dependence by checking the sample stability in two situations: variations of the uncertainties, and variations of the data set.

The first check consists of repeating the *Maximum Likelihood* procedure in the experimental data for different fractions of the estimated uncertainties. Figure 4.10 shows the E_R^{fit} and Γ_0^{fit} values that result when the data set uncertainties are varied between 10 % and 100 % of their original values.

The resulting E_R and Γ_0 parameters values change by around 90 %. For lower uncertainties the value of Γ_0 is stable around 0.09 MeV, whereas for larger errors the E_R value is around 0.60 MeV. Moreover the resulting $\mathscr{L}$ is maximal in a region between 95 % and 100 % of the estimated uncertainties. We interpret the change in the behaviour of E_R and Γ_0, as an overestimation of the errors. The behaviour of $\mathscr{L}$ also suggests that the errors are compatible with the experimental E^{exc} distribution

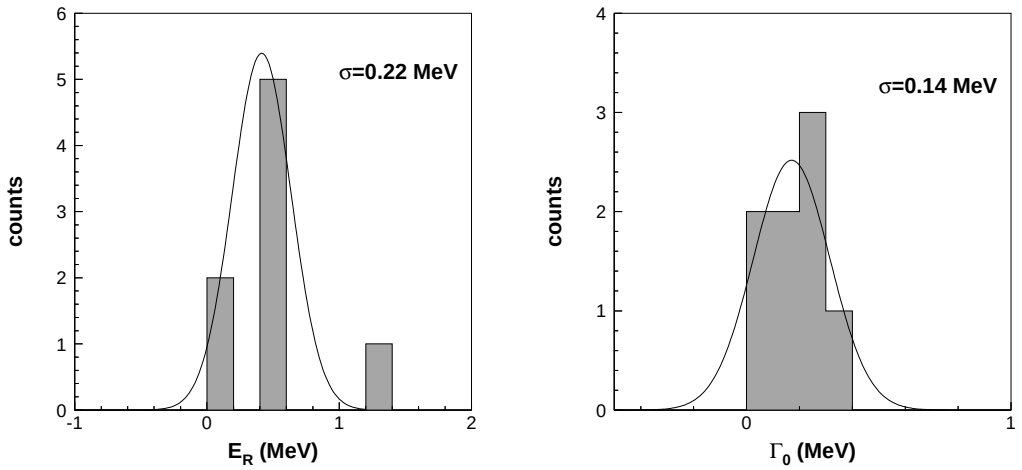

Figure 4.11: *E_R (left panel) and Γ_0 (right panel) for the different subsets of $N-1$ events out of the total N. The result of the whole set of N events is also included in the distributions.*

when they are reduced to around 95 %. We selected a factor of 96 % of the estimated uncertainties as an optimum value, where there is a compromise between the stable value of 0.09 MeV for Γ_0 and the corresponding E_R is close to 0.60 MeV. The validity of this selection would be optimal if variations of the E_R and Γ_0 values due to small variations in the selection are included in the uncertainty estimation.

The uncertainty estimation assumes Gaussian distributions around the measured values. The error propagation is calculated by summing the variances associated with each dependence on the parameters[9]. A check of the sample stability by varying the uncertainties may reveal the limitation of this uncertainty estimation procedure. According to this test, we repeat the *Maximum Likelihood* fit with 96 % of the value of the associated data uncertainties, resulting in $E_R^{fit} = 0.57$ MeV, and $\Gamma_0^{fit} = 0.09$ MeV[10].

The second test consists of repeating the fitting procedure for different data samples in order to check how the results depend on each individual event. We repeat the fit for all the subsets of $N-1$ events out of the total N of data (the seven possible subsets of six events out of seven in our case). Figure 4.11 shows the results of the different fits applied to the $N-1$ subsets. The E_R and Γ_0 distributions are fitted to Gaussian functions and their variances are obtained. The resonance energy E_R varies by ± 0.22 MeV, while the Γ_0 width lies within ± 0.14 MeV.

[9] that is $\sigma_{tot}^2 = \sum(\partial_i)\sigma_i^2$.

[10] the expected life-time of the ^{7}H resonance can then be estimated as $\tau \sim \hbar/\Gamma_0 = 10^{-21}$ s.

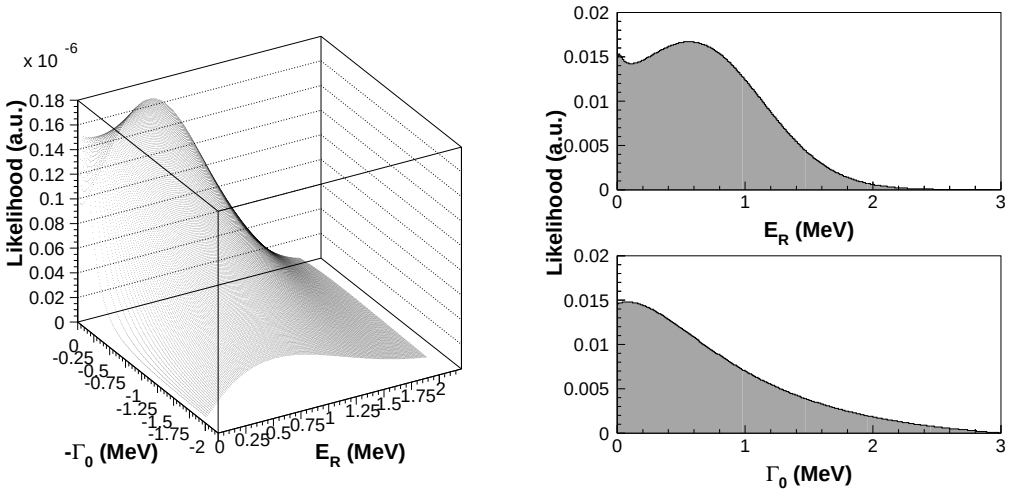

Figure 4.12: *Left panel: $\mathscr{L}$ as a function of E_R and Γ_0. Right panels: projections of $\mathscr{L}$ over E_R (above), and Γ_0 (down).*

The resulting width Γ_0^{fit} is much lower than the width of the experimental distribution (see Figure 4.6). This is indeed the sum of the physical distribution, which we assume in a Breit-Wigner form, and the uncertainty associated with the measurement. The experimental uncertainty dominates the E^{exc} distribution when compared with the resulting width Γ_0^{fit}[11]. The *Maximum Likelihood* procedure separates out the experimental uncertainty contribution by means of the mathematical convolution described in Equation 4.17.

Estimation of the goodness of the *Maximum Likelihood* fit

The *Maximum Likelihood* fit gives the set of E_R and Γ_0 parameters that better describes the experimental distribution. In order to estimate the uncertainty of this set, we treated the projection of $\mathscr{L}$ over each parameter (see Figure 4.12) as probability density distributions $\mathscr{L}_{proj(E_R)}(E_R)$ and $\mathscr{L}_{proj(\Gamma_0)}(\Gamma_0)$. Figure 4.13 shows the corresponding probability functions, which were obtained by the normalization of $\mathscr{L}_{proj(E_R)}(E_R)$, and $\mathscr{L}_{proj(\Gamma_0)}(\Gamma_0)$:

$$\mathscr{L}_{E_R}(E_R) = \frac{\mathscr{L}_{proj(E_R)}(E_R)}{\sum_{k=0}^{500} \mathscr{L}_{proj(E_R)}(k\Delta)\Delta} \tag{4.19}$$

[11] in Table 4.1 a mean value for dE^{exc} larger than 2.5 MeV can be calculated.

$$\mathscr{L}_{\Gamma_0}(\Gamma_0) = \frac{\mathscr{L}_{proj(\Gamma_0)}(\Gamma_0)}{\sum_{k=0}^{500} \mathscr{L}_{proj(\Gamma_0)}(k\Delta)\Delta} \tag{4.20}$$

the sum is performed with fixed steps of $\Delta = 0.01$ MeV up to 5 MeV.

The maximum value of each distribution corresponds to the value of the fitted parameters:

$$\max[\mathscr{L}_{E_R}(E_R)] = \mathscr{L}_{E_R}(E_R^{fit}) \qquad \max[\mathscr{L}_{\Gamma_0}(\Gamma_0)] = \mathscr{L}_{\Gamma_0}(\Gamma_0^{fit}) \tag{4.21}$$

and their variances can be identified as equivalent to the goodness of the Likelihood fit.

The variance of a normalized distribution $f(x)$ with a mean value μ is generally defined as:

$$\epsilon_f^2 = \int_{-\infty}^{+\infty} f(x)(x-\mu)^2 \, \mathrm{d}x \tag{4.22}$$

This definition is modified to meet the specific needs of our case. In the $\mathscr{L}_{E_R}(E_R)$ and $\mathscr{L}_{\Gamma_0}(\Gamma_0)$ distributions the mean value does not correspond to the maximum of distribution, i.e., the mean value is not the parameter resulting in the fit. So the mean value μ is exchange for the fitted E_R^{fit} and Γ_0^{fit}. The other modification deals with the integration limits, which are set at 0 MeV to 5 MeV. To make the variances ϵ_f correspond to values larger and smaller than the fitted parameters, we perform two integrations around the fitted values, equivalent to $\int_{0\ MeV}^{E_R^{fit}}$, and $\int_{E_R^{fit}}^{5\ MeV}$ for E_R^{fit}, and $\int_{0\ MeV}^{\Gamma_0^{fit}}$, and $\int_{\Gamma_0^{fit}}^{5\ MeV}$ for Γ_0^{fit}. Finally we compute the resulting expressions as discrete sums:

$$^{-}\epsilon_{E_R}^2 = \sum_{k=0}^{57} \mathscr{L}_{E_R}(k\Delta)(k\Delta - E_R^{fit})^2\Delta \tag{4.23}$$

$$^{+}\epsilon_{E_R}^2 = \sum_{k=57}^{500} \mathscr{L}_{E_R}(k\Delta)(k\Delta - E_R^{fit})^2\Delta \tag{4.24}$$

$$^{-}\epsilon_{\Gamma_0}^2 = \sum_{k=0}^{9} \mathscr{L}_{\Gamma_0}(k\Delta)(k\Delta - \Gamma_0^{fit})^2\Delta \tag{4.25}$$

$$^{+}\epsilon_{\Gamma_0}^2 = \sum_{k=9}^{500} \mathscr{L}_{\Gamma_0}(k\Delta)(k\Delta - \Gamma_0^{fit})^2\Delta \tag{4.26}$$

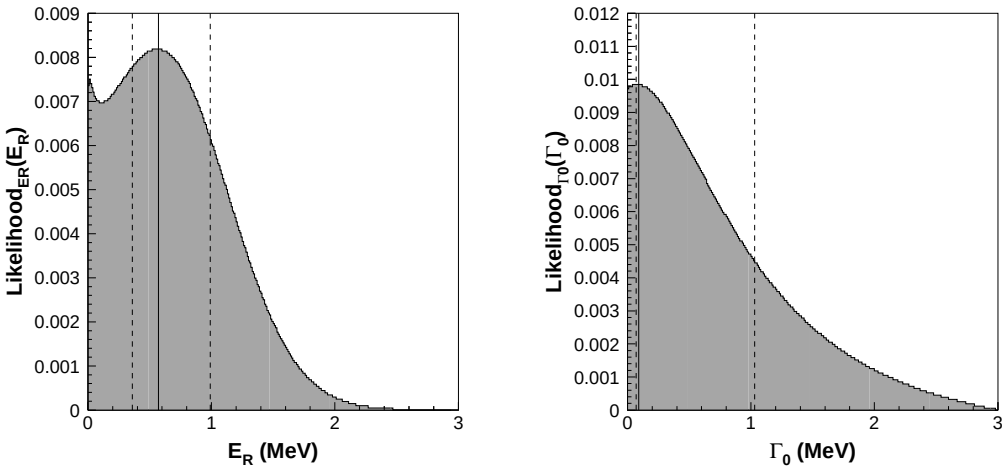

Figure 4.13: *Left panel: normalized distribution $\mathscr{L}_{E_R}(E_R)$. Right panel: normalized distribution $\mathscr{L}_{\Gamma_0}(\Gamma_0)$. Dashed lines are the calculated ${}^-\epsilon$ and ${}^+\epsilon$ for each parameter, solid lines mark the fitted values for E_R and Γ_0.*

with fixed steps of $\Delta = 0.01$ MeV. The resulting values are:

$$ {}^-\epsilon_{E_R} = 0.21 \text{ MeV} \quad (4.27) $$
$$ {}^+\epsilon_{E_R} = 0.42 \text{ MeV} \quad (4.28) $$
$$ {}^-\epsilon_{\Gamma_0} = 0.02 \text{ MeV} \quad (4.29) $$
$$ {}^+\epsilon_{\Gamma_0} = 0.94 \text{ MeV} \quad (4.30) $$

The calculated uncertainties should cover, as we already mentioned, the variations on the selection of the error percentage estimated previously. The negative uncertainty ${}^-\epsilon_{\Gamma_0}$ is very small to include the variation of Γ_0 when the percentages change in +1 %, what results in $\Gamma_0 = 0.04$ MeV. In order to include this variation we increase ${}^-\epsilon_{\Gamma_0}$ in 0.04 MeV, resulting in $\Gamma_0 = 0.02 + 0.04 = 0.06$ MeV.

Estimation of the observed E_{max} and $FWHM$ of the resonance

In order to characterize the enhancement of the production of the ^{7}H in the form of a peak in the E^{exc} spectrum, we used the E_R and Γ_0 parameters contained within the modified Breit-Wigner distribution previously described in Section 4.2.1. However, another set of parameters can be defined which are less dependent on the chosen distribution: the location of the maximum value (E_{max}), and the observed Full Width at Half Maximum ($FWHM$). These parameters can be extracted from the

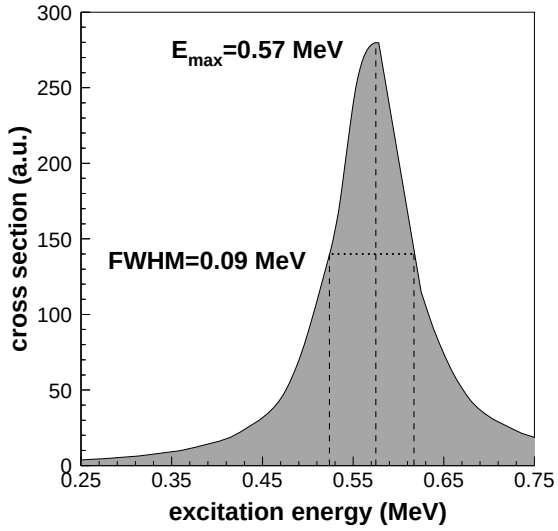

Figure 4.14: *Fitted Breit-Wigner distribution. Dashed lines mark the location of the E_{max} and the limits of the $FWHM$.*

previous fitted distribution, according to their description, as is represented in Figure 4.14.

The E_{max} and $FWHM$ parameters result in $0.57^{+0.42}_{-0.24}$ MeV and $0.09^{+0.79}_{-0.06}$ MeV, with uncertainties calculated as following:

$$
\begin{aligned}
{}^{-}\epsilon^2_{E_{max}} &= E^2_{max}(E_R -^{-} \epsilon_{E_R}) + E^2_{max}(\Gamma_0 -^{-} \epsilon_{\Gamma_0}) && (4.31)\\
{}^{+}\epsilon^2_{E_{max}} &= E^2_{max}(E_R +^{+} \epsilon_{E_R}) + E^2_{max}(\Gamma_0 +^{+} \epsilon_{\Gamma_0}) && (4.32)\\
{}^{-}\epsilon^2_{\Gamma} &= \Gamma^2(E_R -^{-} \epsilon_{E_R}) + \Gamma^2(\Gamma_0 -^{-} \epsilon_{\Gamma_0}) && (4.33)\\
{}^{+}\epsilon^2_{\Gamma} &= \Gamma^2(E_R +^{+} \epsilon_{E_R}) + \Gamma^2(\Gamma_0 +^{+} \epsilon_{\Gamma_0}) && (4.34)\\
& && (4.35)
\end{aligned}
$$

The fact that both set of parameters, E_R with Γ_0, and E_{max} with $FWHM$, are that close in value is part due to the narrow shape of the distribution.

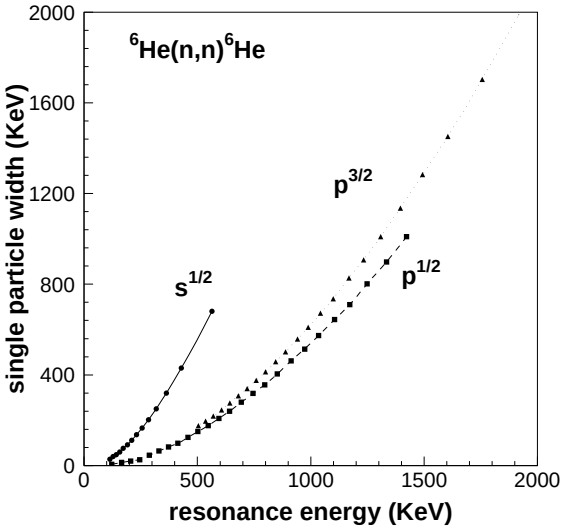

Figure 4.15: *FRESCO calculation of the neutron single particle width dependence with the resonance energy in the* ^{6}He(n,n)^{6}He *scattering, for different* L^S *states.*

Single particle width dependence with excitation energy

At this point we can check other possibilities for the single particle width dependence on the energy. During this study we chose a square root dependence for the neutron single particle width, as it is discussed in Section 4.2.1, $\Gamma \propto \sqrt{E}$. Calculations with FRESCO code [Tho06] show a possibility for a square-like dependence, $\Gamma \propto E^2$, of the Γ width[12], as it can be seen in the calculation of Figure 4.15 for the test reaction ^{6}He(n,n)^{6}He [13]. A general calculation of Γ with the phase shift can be expressed as (see for example [Des01] or [Wur97]):

$$\Gamma = 2 \left(\frac{\partial \delta(E)}{\partial E} \right)^{-1} \Bigg|_{E=E_R} \tag{4.36}$$

From the most of the examples, the behaviour of Γ near the resonance energy[14] falls somewhere between a root-like description, and a linear dependence, $\Gamma \propto E$ (see

[12] in reference [Hal04] is also posible to extract a square-like dependence, even if is not specifically mentioned in the text.

[13] calculation performed by H.W. Wang.

[14] $\delta(E_R) = \pi/2$, see also [Des01].

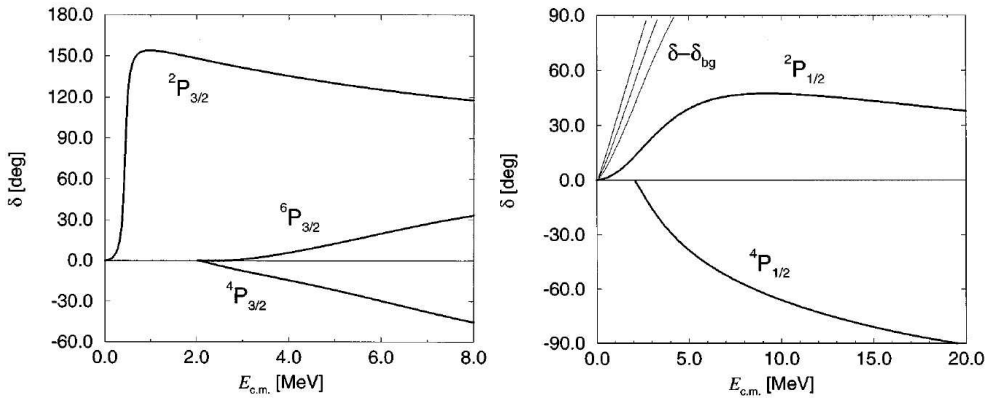

Figure 4.16: *Diagonal phase shift* $\frac{3}{2}^-$ *and* $\frac{1}{2}^-$ *of* ^{6}*He+n and* ^{6}*He*+n resonant elastic scattering, as calculated in reference[Wur97].*

Figure 4.16).

In order to check these possibilities we calculate the corresponding set of E_R and Γ_0 parameters for each of the Γ behaviours, that reproduce the same E_{max} and $FWHM$ in the energy distribution[15]. The resulting values are summarized in table 4.2 and compared in Figure 4.17.

$\Gamma(E)$ *dependence*	$\mathbf{E_R}$ MeV	$\mathbf{\Gamma_0}$ MeV
$\Gamma = \Gamma_0\sqrt{E/E_R}$	$0.57^{+0.42}_{-0.21}$	$0.09^{+0.94}_{-0.06}$
$\Gamma = \Gamma_0\ E/E_R$	$0.57^{+0.46}_{-0.24}$	$0.09^{+1.20}_{-0.06}$
$\Gamma = \Gamma_0(E/E_R)^2$	$0.57^{+0.64}_{-0.23}$	$0.10^{+4.67}_{-0.07}$

Table 4.2: *The* E_R *and* Γ_0 *parameters are calculated for different single particle widths dependences.*

Again, due to the narrow nature of the resonance, the results do not differ much from one description to another.

[15] we supose that different descriptions of the distribution should led to the same maximum and FWHM, since these parameters do not depend much on the parameterization.

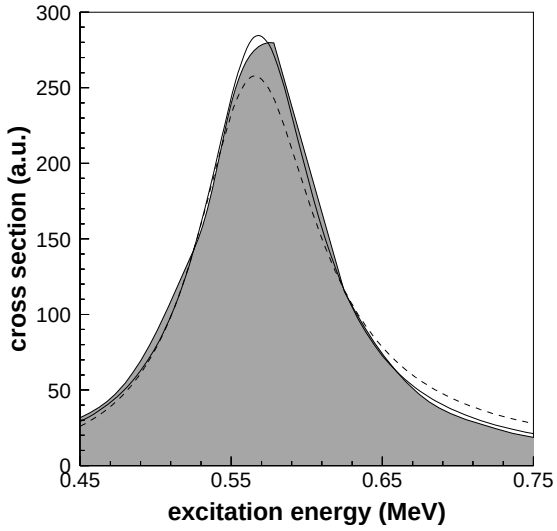

Figure 4.17: *Comparison between $\propto \sqrt{E}$, $\propto E$, and $\propto E^2$ dependences of single particle width. Full grey distribution: $\propto \sqrt{E}$ dependence of Γ described in Section 4.2.1. $\propto E$ and $\propto E^2$ depences are marked with solid and dashed lines.*

Summary

Finally the energy E_R and the width Γ_0 of the resonance were obtained from the fitting of the experimental data to the Breit-Wigner distribution with the Likelihood procedure, and checked with different tests on the stability of the sample. The associated errors were computed with the variance of the normalized $\mathscr{L}$ probability density distribution. The fitted parameters are:

$$\mathbf{E_R} = 0.57^{+0.42}_{-0.21}\ \text{MeV} \quad \text{and} \quad \mathbf{\Gamma_0} = 0.09^{+0.94}_{-0.06}\ \text{MeV} \tag{4.37}$$

with the observable maximum and width:

$$\mathbf{E_{max}} = 0.57^{+0.42}_{-0.24}\ \text{MeV} \quad \text{and} \quad \mathbf{FWHM} = 0.09^{+0.79}_{-0.06}\ \text{MeV} \tag{4.38}$$

4.3 Experimental Cross Section

The present section is devoted to the calculation of the experimental cross section of ^{7}H in the transfer reaction ^{12}C(^{8}He,^{7}H)^{13}N. The cross section, $\sigma_{(^{7}H)}$, is directly related with the probability of producing the ^{7}H resonance. It completes its characterization allowing the determination of the normalization factor σ_0 used in the Breit-Wigner distribution (see Section 4.2.1).

4.3.1 Production cross section

The production cross section is computed essentially as the ratio of the number of reactions of interest produced per projectile particle and target atom:

$$\sigma_{(^{7}H)} = \frac{N(^{7}\mathrm{H})}{N(^{8}\mathrm{He})N(^{12}\mathrm{C})} \tag{4.39}$$

The number of projectiles, $N_{^{8}\mathrm{He}}$, and atoms in the target, $N_{^{12}\mathrm{C}}$, are calculated in Section 3.3, and reviewed in table 4.3. The number of produced reactions, $N_{^{7}\mathrm{H}}$, is estimated with the number of measured events corrected by the detection efficiency ε_{det}, and, in general, the factor F_{DT} for correcting the events lost due to the acquisition dead time, DT:

$$N_{^{7}\mathrm{H}} = \frac{N^{rec}_{^{7}\mathrm{H}}}{\varepsilon_{det} F_{DT}} \tag{4.40}$$

The detection efficiency ε_{det} is calculated in Section 3.2.4, and results in $\varepsilon_{det} = 28 \pm 0.3$ %. The dead time correction can be estimated with the probability of producing more than one reactions in a time region equal to DT. This depends on the ratio bewteen the production reaction frequency f_{reac} (reactions produced), and the detection reaction frequency f^{rec} (reactions detected and recorded). The frequency f^{rec} can be calculated as:

$$f^{rec} \approx \frac{N^{rec}}{N_{^{7}\mathrm{H}}} I_{beam} \tag{4.41}$$

In our case the total number of recorded events is $N^{rec} = 19.4 \cdot 10^{6}$, the number of projectiles is $N_{^{8}\mathrm{He}} = 10.2 \cdot 10^{9}$ (see table 4.3), and the intensity of the beam

exp.setup	$\mathbf{F_{DT}}$ %	$\varepsilon_{\mathbf{det}}$ %	$\mathbf{N_{^8He}}$ 10^9 counts	$\mathbf{N_{^{12}C}}$ 10^{19} cm^{-2}	$\mathbf{N^{rec}_{^7H}}$ counts	$\sigma_{(^7\mathbf{H})}$ μb
30 *mbar*	99.98 ±0.01	28.0 ±0.3	7.22 ±0.20	3.22 ±0.35	**5** ±2.24	**76.8** ±**35.4**
26 *mbar*	99.98 ±0.01	28.0 ±0.3	3.04 ±0.09	3.01 ±0.33	**2** ±1.41	**78.1** ±**55.9**

Table 4.3: *Calculation of the production cross section associated to the production of ^7H in each experimental setup. See text for details*

is $I_{beam} \approx 10^4$ Hz. Applying these quantities the frequency f^{rec} results in ≈20 reactions/s.

Each recorded event produces DT, the total amount of data lost during the DT is then $\mathscr{F}_{DT} = f^{rec}DT$. The fraction of recorded data is:

$$F_{DT} = \frac{f^{rec}}{f_{reac}} = 1 - \mathscr{F}_{DT} \tag{4.42}$$

with $DT \simeq 10$ μs (see Section 2.3), results in $F_{DT} = 99.98$ %. That is, we loose $(1 - F_{DT})N^{rec} \simeq 3800$ events from any reaction channel during the whole experiment.

Finally the production cross section is:

$$\sigma_{(^7H)} = \frac{N^{rec}_{^7\mathrm{H}}}{\varepsilon_{det}F_{DT}N_{^8\mathrm{He}}N_{^{12}\mathrm{C}}} \tag{4.43}$$

The uncertainty corresponding to the F_{DT} factor is estimated in $dF_{DT} \leq 0.01$ %, whereas $dN^{rec}_{^7\mathrm{H}} = \sqrt{N^{rec}_{^7\mathrm{H}}}$. Applying Equation 4.43 with both experimental setups, the resulting cross sections are: $\sigma^{30}_{(^7H)} = 76.8 \pm 35.4$ μb for the 30 mbar setup, and $\sigma^{26}_{(^7H)} = 78.1 \pm 55.9$ μb for the 26 mbar setup. Table 4.3 reviews the results along with the associated uncertainties (see Appendix A.2 for details).

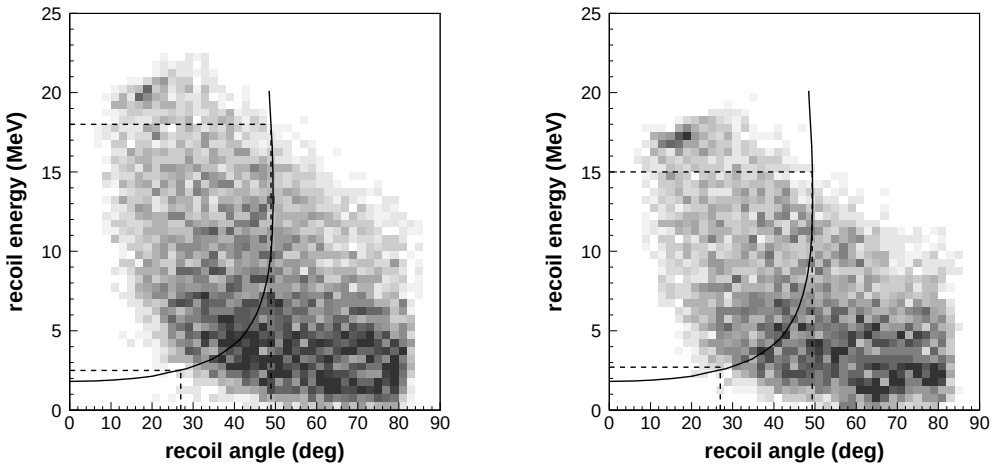

Figure 4.18: *Angular coverages for both setups with 30 mbar (left panel) and 26 mbar (right panel). The solid line draws the kinematics of the ^7H production over the experimental data sets.*

4.3.2 Differential cross section

The calculated cross section $\sigma_{(^7H)}$ is limited by the angular coverage of the detection system, determined mainly by the geometry of the detector. In our case is not only the geometry of MAYA but also the pressure of the gas which fixes this coverage. Each setup based on different pressures allows different angle-range relations for the recoil particle stopped inside MAYA. Figure 4.18 shows the difference coverage of the reaction kinematics of ^{7}H in the two setups used in the experiment. The angular region of the ^{7}H kinematics covered by MAYA ranges approximately between $27< \theta_{lab} <48.9$ deg in the 30 mbar setup, and $27< \theta_{lab} <49.3$ deg in the 26 mbar setup, both in laboratory frame. The uncertainty for the lower limits is estimated in ± 1 deg, and ± 1 MeV for the upper limit. In center of mass frame these regions are $9.7\pm0.6< \theta_{cm} <48.2\pm0.7$ deg in the 30 mbar setup and $9.7\pm0.5< \theta_{cm} <43.3\pm0.8$ deg in the 26 mbar setup (see Figure 4.19).

The measured $\sigma^{30}_{(^7H)}$ and $\sigma^{26}_{(^7H)}$ can be express as the sum of the differential cross section over each angular region as:

$$\sigma^{30}_{(^7H)} = \int_{9.7}^{48.2} \left(\frac{\mathrm{d}\sigma_{(^7H)}}{\mathrm{d}\Omega} \right)^{30} \sin\theta_{cm} 2\pi \mathrm{d}\theta_{cm} \tag{4.44}$$

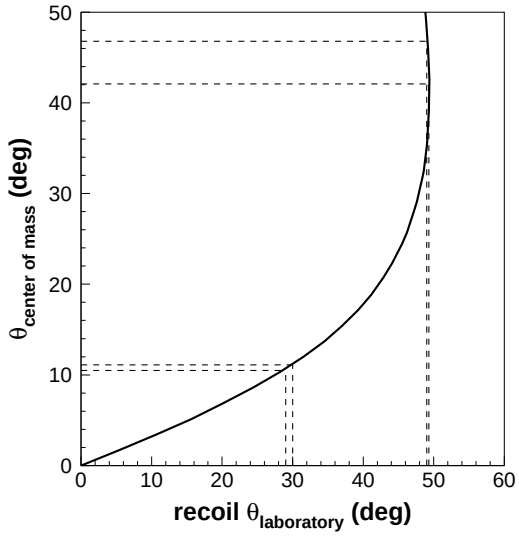

Figure 4.19: *Relation between laboratory and center of mass frames for the recoil θ angle in the ^7H reaction.*

$$\sigma^{26}_{(^7H)} = \int_{9.7}^{43.3} \left(\frac{\mathrm{d}\sigma_{(^7H)}}{\mathrm{d}\Omega} \right)^{26} \sin\theta_{cm} 2\pi \mathrm{d}\theta_{cm} \tag{4.45}$$

Assuming a linear dependence of $\sigma_{(^7H)}$ with the solid angle Ω we have:

$$\sigma^{30}_{(^7H)} \simeq \left(\frac{\mathrm{d}\sigma_{(^7H)}}{\mathrm{d}\Omega} \right)^{30} \int_{9.7}^{48.2} \sin\theta_{cm} 2\pi \mathrm{d}\theta_{cm} \tag{4.46}$$

$$\sigma^{26}_{(^7H)} \simeq \left(\frac{\mathrm{d}\sigma_{(^7H)}}{\mathrm{d}\Omega} \right)^{26} \int_{9.7}^{43.3} \sin\theta_{cm} 2\pi \mathrm{d}\theta_{cm} \tag{4.47}$$

Finally:

$$\left(\frac{\mathrm{d}\sigma_{(^7H)}}{\mathrm{d}\Omega} \right)^{30}_{9.7-48.2} \simeq \frac{\sigma^{30}_{(^7H)}}{2.01} = 38.2^{+64.9}_{-38.2} \ \ \mu\mathrm{b/sr} \tag{4.48}$$

and

$$\left(\frac{\mathrm{d}\sigma_{(^7H)}}{\mathrm{d}\Omega} \right)^{26}_{9.7-43.3} \simeq \frac{\sigma^{26}_{(^7H)}}{1.63} = 47.8^{+129.1}_{-47.8} \ \ \mu\mathrm{b/sr} \tag{4.49}$$

The large uncertainties (see Appendix A.2 for details) have their source on the determination of the angular coverage of MAYA. The resulting $\left(\frac{\mathrm{d}\sigma_{(^7H)}}{\mathrm{d}\Omega}\right)$ are independent on the experimental setup and conditions, and should be identical under our assumption of a linear dependence of $\sigma_{(^7H)}$ with the solid angle Ω. The mean value can be adopted as a definitive value for the differential cross section measurement, resulting in:

$$\left(\frac{\mathrm{d}\sigma_{(^7H)}}{\mathrm{d}\Omega}\right) = \mathbf{40.1}^{+\mathbf{58.0}}_{-\mathbf{30.6}} \ \mu\mathrm{b/sr} \tag{4.50}$$

Determination of the Breit-Wigner normalization

The ^{7}H resonant state is characterized in this work with a Breit-Wigner distribution (see Section 4.2.1). The distribution contains the information about the probability of producing the ^{7}H in the σ_0 factor, which can be deduced from the reaction cross section. The integral of the normalized Breit-Wigner distribution σ_{BW} should be equal to the total probability of producing the ^{7}H resonance, which can be expressed in the form of its cross section $\left(\frac{\mathrm{d}\sigma_{(^7H)}}{\mathrm{d}\Omega}\right)$:

$$\int \sigma_{BW} \mathrm{d}E^{exc} = \left(\frac{\mathrm{d}\sigma_{(^7H)}}{\mathrm{d}\Omega}\right) \tag{4.51}$$

Assuming σ_0 as a constant factor, the integral of σ_{BW} can be reduced as:

$$\int \sigma_{BW} \mathrm{d}E^{exc} = \sigma_0 \int_0^{+\infty} \frac{\Gamma_0 \sqrt{\frac{E^{exc}}{E_R}}}{(E^{exc} - E_R)^2 + \frac{\Gamma_0^2}{4}\left(\frac{E^{exc}}{E_R}\right)} \mathrm{d}E^{exc} = \sigma_0 \mathscr{I}(E_R, \Gamma_0) \tag{4.52}$$

Then, the link between the normalization factor and the differential cross section is:

$$\sigma_0 = \frac{\left(\frac{\mathrm{d}\sigma_{(^7H)}}{\mathrm{d}\Omega}\right)}{\mathscr{I}(E_R, \Gamma_0)} \tag{4.53}$$

The integral results in $\mathscr{I} = 6.2 \pm 0.6$ for the fitted E_R and Γ_0 (see Section 4.2.2). Finally:

$$\sigma_0 = 6.4^{+9.0}_{-4.9} \ \mu\mathrm{b/sr} \tag{4.54}$$

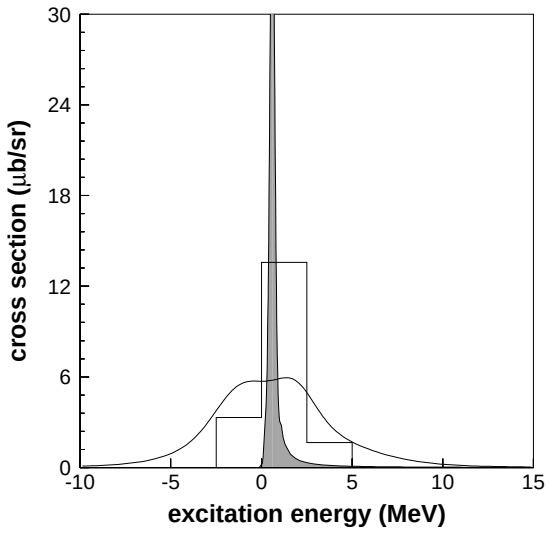

Figure 4.20: *Comparison between the measured E^{exc} and the fitted Breit-Wigner distribution. Both empty distributions represent the measured E^{exc} for the identified ^7H events. The solid function is the σ_{BW} function resulting in our analysis. The σ_{BW} distribution is much higher than the experimental spectra in order to keep the area of both distributions equal to the measured cross section.*

See Appendix A.2 for details in the uncertainty estimation.

Review on the ^{7}H characterization

The measured distribution of events identified as ^{7}H resonance reactions is characterized by a Breit-Wigner distribution with three parameters: the energy of reaction E_R, the resonance width Γ_0, and the normalization factor σ_0 related with the probability of production. The resulting distribution is:

$$\sigma_{BW} = 6.4 \frac{0.09\sqrt{\frac{E^{exc}}{0.57}}}{(E^{exc}-0.09)^2 + \frac{0.09^2}{4}\left(\frac{E^{exc}}{0.57}\right)} \quad \mu\text{b/sr} \tag{4.55}$$

and is shown in Figure 4.20 compared with the measured data.

Chapter 5

Discussion and Comparison of the Results

The present study about the finding and characterization of ^{7}H would not be complete without a final discussion and comparison with previous experimental results and theoretical predictions, already mentioned in chapter 1. This chapter begins with a discussion of the few theoretical predictions involving the ^{7}H resonance, and ends with a comparison of the experimental results to those of previous studies.

5.1 Comparison with Theoretical Predictions

Among the different theoretical approaches that attempt to describe the properties of extremely neutron rich light isotopes (see Section 1.1.1) there are only a few predictions about ^{7}H. In this section we review two of such predictions: the extended *Antisymmetrized Molecular Dynamics* (AMD) approach [Aoy04], and the hyperspherical approach based on the shell model description [Tim02][Tim04]. Both models can be classified as *ab-initio* calculations, where the nuclear systems are mainly treated with a nucleon-nucleon interaction, resulting in a very realistic and general description. Although there is still room for improvement in the ability of these models to predict the existence of resonances, the $ab-initio$ microscopic models are progressing rapidly and it is expected that their main difficulty, very time-consuming calculations, can soon be overcome in the future.

The extended AMD approach is briefly described in Section 1.1.1. It is based on a random inspection of the positions of each individual nucleon in the total wave function of the system using the *Generator Coordinate Method*. Figure 5.1 gives

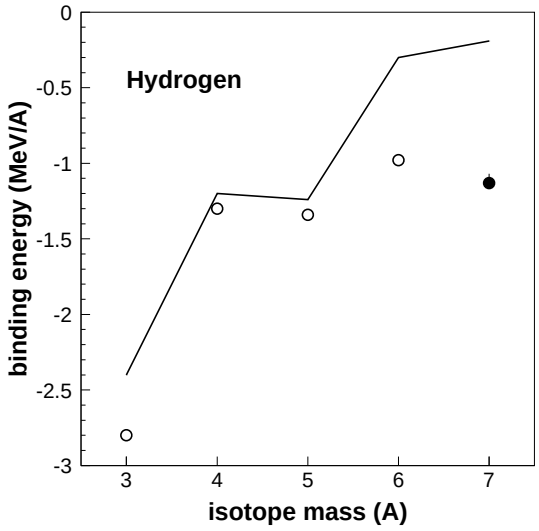

Figure 5.1: *Systematic binding energies for Hydrogen isotopes. The solid line is the AMD prediction. Empty points correspond to previous experimental results and the full point represents the binding energy of the* ^{7}H *resonance calculated in our work.*

ab example of its application [Aoy04] to the systematic binding energies of Hydrogen isotopes. When comparing the results with experimental values we can observe a systematic shift, that is much higher in the particular case of ^{7}H. The authors, Aoyama and Itagaki, are aware of this discrepancy, which was already suggested by the work of Korsheninnikov *et al.* [Kor03], and they indicate the need for additional correlations and/or modification of the interaction. Future studies are to include more detailed information about the ^{7}H structure, by coupling two channels: a tritium core surrounded by four valence neutrons and a single proton surrounded by three di-neutron clusters.

The *hyperspherical harmonics* method is applied to the shell model in the work of Timofeyuk (Section 1.1.1). The shell model is widely used throughout the nuclear chart, giving a good description of the properties of most experimentally accessible nuclei. Shell model predictions begin to fail as we move away from the stability valley and new properties in these exotic nuclear systems appear, or when there are few nucleons and individual interactions dominate the mean field approximation. The main advantage of using the hyperspherical basis that it overcomes the many-body problem and extracts valuable predictions.

The primary difficulty of the hyperspherical method is the need for convergence

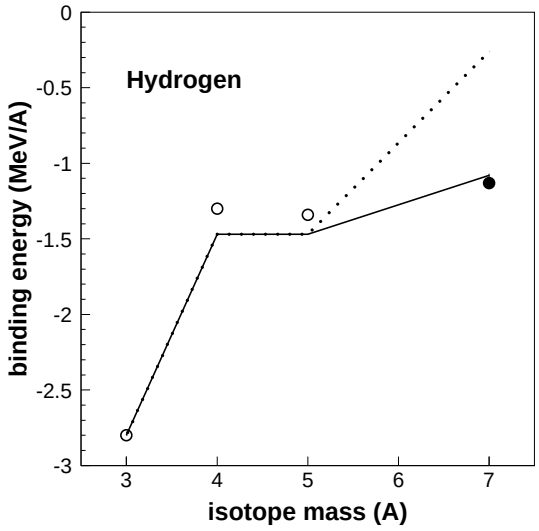

Figure 5.2: *Systematic binding energies for Hydrogen isotopes. The solid line is the extrapolated result calculated with the hyperspherical basis description of the shell model [Tim02], the dotted line is the result from a following work [Tim04]. Empty points correspond to previous experimental results and the full point is the binding energy of the ^7H resonance calculated in our work.*

of the series in hypermomentum, which can be technically difficult to obtain for some relatively heavy systems, as in the case of ^{7}H. When this occurs, an extrapolation of the series may be an option. These results are represented in Figure 5.2, with the extrapolated values for the Hydrogen isotopes.

A good agreement is seen between the experimental results and calculations from [Tim02]. In a latter work, Timofeyuk refines the method by constructing the basis state that corresponds to the O_{A-1} symmetry [Tim04]. The parameters of the O_{A-1} group can be conveniently chosen as independent variables used to describe the intrinsic motion in the A-body system. The use of this new basis changes the results for ^{3,4,5}H slightly, but an extrapolation is needed again where ^{7}H is concerned. Timofeyuk compares the ^{7}H+p and ^{8}He systems and suggests a ^{7}H resonance energy about 3 MeV above the ^{3}H+4n threshold.

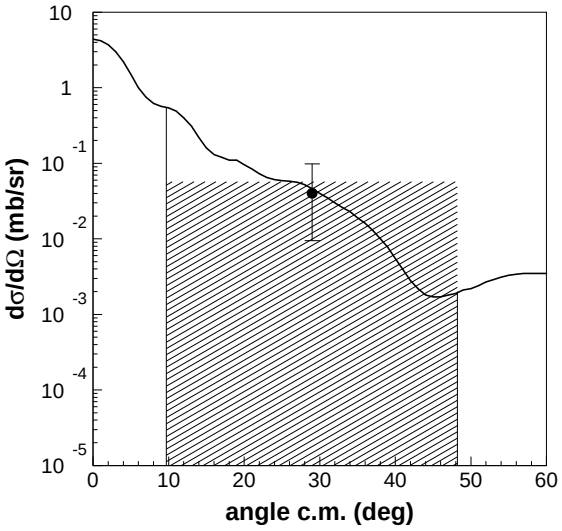

Figure 5.3: *FRESCO calculation of the* $^{12}C(^{8}He,^{7}H)^{13}N$ *reaction differential cross section. The vertical solid lines mark the experimental angular coverage. The hatched area represents the average differential cross section within the experimental coverage, whereas the black dot is the experimental average differential cross section.*

Cross section calculation

The cross-section calculation associated to direct reactions has received especial attention since more than fifty years [Fes58][Lan58], with several attempts to refine the results from different descriptions and approximations of the reaction mechanism.

In one of the first approximations [Fes74] the whole Hilbert space is split into a region containing the possible wave functions of the entrance and exit channels of the system, and a region with the remaining space. The corresponding Hamiltonian is then constructed on the system space. In another approximation [Sat83], the *Distorted Wave Born Approximation* helps to simplify the description of the emerging wave functions after the interaction occurs, by treating them as plane waves affected by the involved potentials and without intermediate states. The potentials themselves are also approximated in different ways, normally treated as optical potentials that fit the elastic scattering channel, and modified with distorted interactions that depend on the channels and structure of the nuclei. When it is necessary to calculate the coupling of different channels, the R-matrix formalism [Lan58] includes non-local couplings from nucleon transfer. Basically, the R-matrix method diagonalizes the set of Hamiltonians associated with each channel, finding a basis of the

eigensolutions of the system, and expanding the scattering wave functions in terms of this basis, finding the solutions faster than other calculation methods.

In the last years, I.J. Thompson has developed the FRESCO code [Tho06], that takes profit of all these achievements in direct reaction descriptions for calculating the associated cross sections, being one of the most valuable and widely used tools in direct reaction descriptions.

The prediction for the cross section associated with the production of ^{7}H resonance calculated with the FRESCO code[1] is shown in Figure 5.3. The average value of the differential cross section between the experimental angular range of $9.7< \theta_{c.m.} <48.2$ deg (marked by the vertical solid lines in Figure 5.3) predicted by the FRESCO code is $\left(\frac{d\sigma_{(^{7}H)}}{d\Omega}\right)= 56.9$ μb/sr. The cross section measured in our experiment (marked with a black dot in figure 5.3) is in agreement with the FRESCO code calculation within the error bars, $\left(\frac{d\sigma_{(^{7}H)}}{d\Omega}\right)= 40.1^{+58.0}_{-30.6}$ μb/sr. This result reinforces the validity of the FRESCO code and its description of the transfer reactions mechanism.

5.2 Comparison with Previous Experimental Results

The low cross section associated with the reactions and the experimental procedures, mainly based on missing mass reconstruction of the reaction, makes it difficult not only to produce the ^{7}H resonance, but also to detect it positively. Consequently, there has been very little success extracting experimental information about the resonance. Two relevant experiments and their findings are reviewed in this section compared to ours.

The first indication of the existence of ^{7}H was reported by Korsheninnikov *et al.* [Kor03], whose search was encouraged by the theoretical work of Timofeyuk [Tim02], also reviewed in Section 5.1. For the experiment, Korsheninnikov *et al.* assumed that the neutrons in the ground state of ^{7}H occupy the same orbitals as in ^{8}He. If this were so, it could be possible to populate the ground state of ^{7}H by picking up one proton from ^{8}He. Our experimental approach was similar to that of Korsheninnikov *et al.* with the main difference being the reaction mechanism. Korsheninnikov *et al.* used the pickup reaction with a Hydrogen target: p(^{8}He,pp)^{7}H, while we chose the transfer reaction channel.

[1] calculation performed by P. Roussel-Chomaz. The parametrization of the applied potentials was based according with predictions for similar reactions.

	two − body phase space	three − body phase space	five − body phase space	this work
$\mathbf{E_R}$ (MeV)	1.5 ± 0.1	3.1 ± 0.5	8.1 ± 1.5	$0.57^{+0.42}_{-0.21}$
$\mathbf{\Gamma}$ (MeV)	2.6 ± 0.6	11.2 ± 2.9	49.1 ± 10.6	$0.09^{+0.94}_{-0.06}$

Table 5.1: *Characterization of the ^7H spectra resulting from the subtraction of two-body, three-body, and five-body phase space. The uncertainties are the mathematical errors of the fit, except in the case of the results from this work, that include the uncertainties estimated in section A.*

The Korsheninnikov *et al.* experiment was done at RIKEN (Japan) using a secondary ^{8}He beam at 61.3A MeV. The projectiles impinged on a cryogenic Hydrogen target of $6{\times}10^2$ protons/cm^2. The trajectory and energy of each beam projectile were measured with plastic scintillators and multiwire proportional chambers. The two protons emerging from the reaction were detected, and their angles and energy measured by a stack of Silicon strip detectors. The tritium and neutrons from the breakup of ^{7}H can also be detected by a system composed of a dipole magnet and plastic scintillators.

The mass of the ^{7}H system was reconstructed using only the information extracted from the two protons detected in coincidence. The calculated energy spectrum of ^{7}H showed a sharp increase of the cross section at the ^{3}H+4n threshold (Figures 1.7 and 5.4). The energy spectrum was obtained after empty target measurement subtraction, and there used three attempts to explain the resulting distribution with non-resonant continuums. The calculations correspond to five-body, four-body, and two-body phase space, equivalent to ^{3}H+4n, ^{3}H+^{2}n+^{2}n, and ^{3}H+^{4}n decay channels. Since any of the continuum calculations does not cover the resulting spectrum, the increase is thought to be due to the production of the ^{7}H resonance. Figure 5.4 shows the resulting spectra after subtraction of the different possible continuums[2].

After subtraction of the phase space contribution, the ^{7}H energy spectrum should correspond to the formation of the resonance, and can be characterized as a Breit-Wigner distribution. The panels of Figure 5.4 show the fit of the spectra corresponding to each type of phase space. The results are reviewed in Table 5.1.

[2]the analysis with the subtracted continuums was not done by Korsheninnikov *et al* in the original reference. We performed it in our work for comparison purposes.

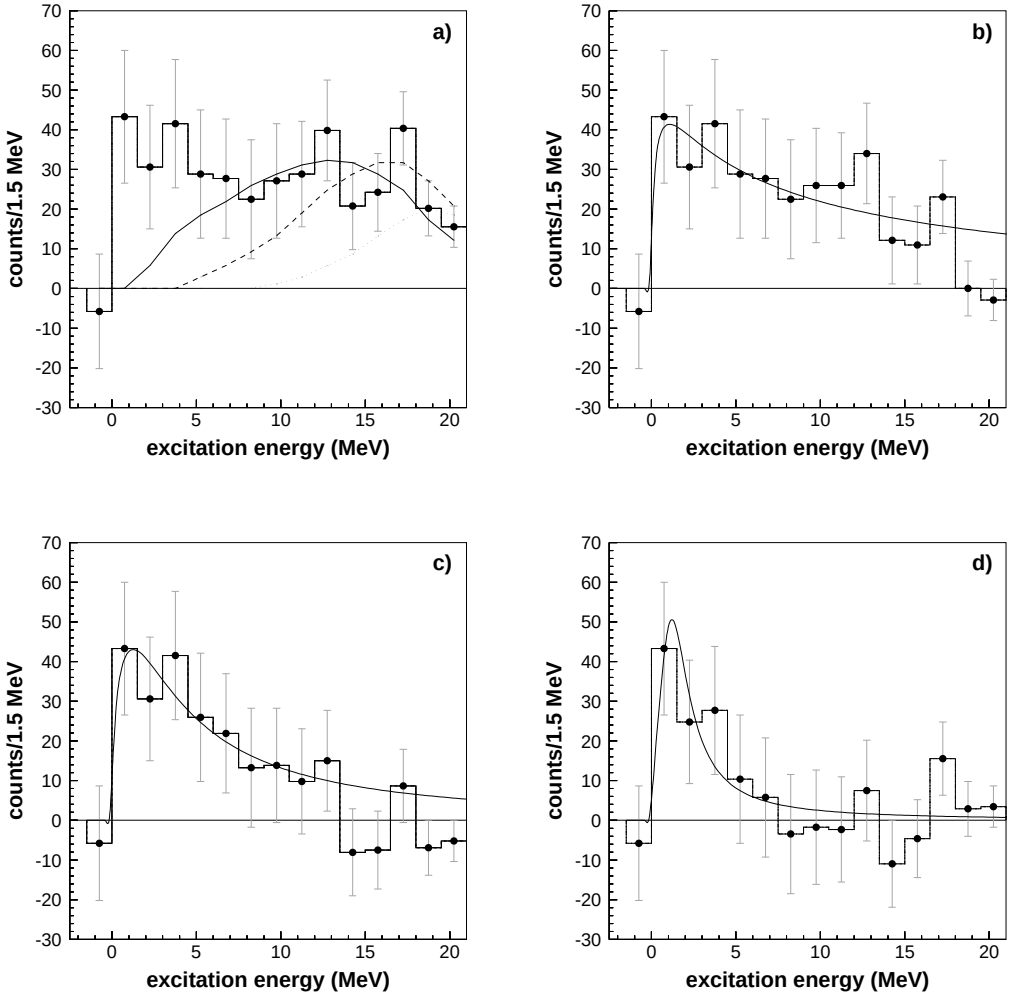

Figure 5.4: *Panel a): spectrum of ^7H from [Kor03]. The curves are estimations of five-body (dotted line), three-body (dashed line), and two-body (solid line) phase-space contributions. Panels b), c), and d), show the resulting ^7H spectra after subtraction of the five, three and two-body phase space estimations. The spectra are fitted to Breit-Wigner distributions for reference. See text for details*

By comparing the results in Table 5.1 with the results of our work, we can infer that the two-body phase space matches both studies more closely. This result would reinforce the suggestion of a four-neutron decay, perhaps within a virtual state. However, the resulting width is still much broader than our result, possibly due to the influence of other reaction channels giving two protons in the final state[3]. In any case, the main finding from the work of Korsheninnikov *et al.* was the sharp increase of the cross section in the ^{3}H+4n threshold. This is consistent with the results of our work, which shows a narrow peak very near the threshold.

Regarding the cross section, Korsheninnikov *et al.* report $\sim 10^{-2}$ mb sr^{-1}MeV^{-1}, which is similar to the cross section estimated in our work, $40.1^{+58.0}_{-30.6}$ μb/sr. Since both reaction mechanisms are based on removing a proton from the ^{8}He projectile, a certain level of agreement was expected.

The promising results of Korsheninnikov *et al.* encouraged Golovkov *et al.* to attempt direct detection of ^{7}H nucleus [Gol04a]. The theoretical calculations made in the work of Golovkov *et al.* related the width of ^{7}H to its decay energy, leaving room for a very small width, and thereby indicating a long-living quasi-stable ^{7}H nucleus. The experiment was made in Dubna (Russia) with a 20.5 MeV/u ^{8}He beam impinging on a liquid deuterium target. The authors searched in the ^{2}H(^{8}He,^{7}H)3He reaction, for which they had estimated a cross section of 100-150 nb/sr. The reaction products were identified by means of ΔE-E measurement with Si and CsI detectors. The results revealed no trace of ^{7}H.

Golovkov *et al.* set a limit of 3 nb/sr for the experimental cross section. Since this is more than 30 times the previously estimated cross section, they concluded that the lifetime of ^{7}H is less than 1 ns. A lower limit in the breakup energy of 50-100 KeV was also set, based on the calculated relation between the width and energy of the resonance. This width-energy function is compared with our results in Figure 5.5. Even thought the lower limit of the breakup energy is compatible with our result, our measurement of the width lies in an upper region of the Golovkov *et al.* estimation. Qualitatively, the model describes narrow states, with $\Gamma \leq 1$ MeV, for $E_R < 3$ MeV, which is in agreement with our observations.

[3]the coincidence of the two protons with tritium may help to reduce this background. The authors reported that "Spectra measured in coincidence with triton (...) have a very similar character, but lower statistics".

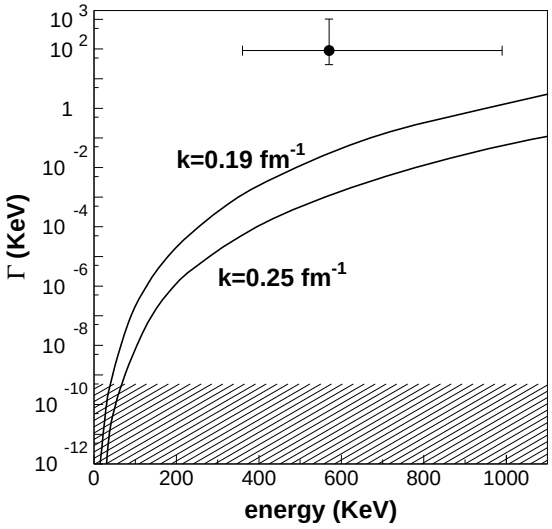

Figure 5.5: *Width dependency on energy for the ground state of* ^7H*, with hyperspherical momentum K=2. The two lines stand for different assumptions of the parameter k, related to the radial part of the interaction (see [Gol04a]). The hatched area corresponds to lifetimes that allow direct detection within the experimental setup. The black point correspond to to our experimental result.*

Conclusions

The experimental observation of ^{7}H resonance is addressed in this work. The resonance was produced via one-proton transfer reactions between a ^{8}He 15.4A MeV radioactive beam and a ^{12}C gas target. The use of the active target MAYA allows a complete 3-d tracking of the recoil partner of the reaction. This information makes possible the kinematic analysis of the ^{7}H formation, and the characterization of the ^{7}H resonance as a peak of the production cross section in the excitation energy spectrum.

The experimental setup was based on the detector MAYA, which has been proved to be a valuable tool for studying this type of reaction with extremely low energy recoil. The low efficiency (of 28 %) for this reaction is compensated with the scarce sources of background (reduced phase space), and with a dedicated analysis of the individual interesting events (see apendix C). The identification of the scattered ^{3}H from the ^{4,5,6,7}H decay, and the recoil Nitrogen allows a good separation from other reaction channels. We have developed different tracking methods and range determination, suitable for being used in future experiments with MAYA (or other similar detectors).

The analysis of the ^{3}H+Nitrogen channels[4] shows different peaks in the excitation energy spectrum that can be attributed to the ^{5}H, ^{6}H, and ^{7}H production. The comparison of the ^{5}H and ^{6}H resonance energies resulted compatible with previous observations , even with our low statistics. The formation of a peak compatible with the ^{7}H production stands as the first experimental observation of such a extremely neutron-rich exotic nuclear state.

The ^{7}H state is characterized as a Breit-Wigner distribution[Bre36]. The seven events compatible with the ^{7}H production are fitted with a *Maximum Likelihood* procedure to extract the Breit-Wigner distribution parameters. The results of this procedure are a resonance energy of $E_R = 0.57^{+0.42}_{-0.21}$ MeV, and a resonance width of $\Gamma = 0.09^{+0.94}_{-0.06}$ MeV. The measured cross section results in $40.1^{+58.0}_{-30.6}$ μb/sr for an

[4]including ^{12}C(^{8}He,^{7}H$\rightarrow^{3}$**H**+4n)^{13}**N**, ^{12}C(^{8}He,^{6}H$\rightarrow^{3}$**H**+3n)^{14}**N**, ^{12}C(^{8}He,^{5}H$\rightarrow^{3}$**H**+2n)^{15}**N**.

angular coverage of $\sim 10 - 45$ degrees in center of mass frame.

The estimated resonance energy is in agreement with previous works from Korsheninnikov *et al.* where a sharp increase of the cross section, associated with the production of ^{7}H, was observed near the ^{3}H+4n threshold in the ^{8}He(p,pp) reaction. On another hand, theoretical studies using hyperspherical coordinates on the basis of the shell model provide predictions about the resonance energy compatible with our results. The very narrow width of the resonance obtained in this experimental work reinforces the suggestion of Korsheninnikov of an unique four-neutron decay channel.

With this work, we demonstrate the capabilities of MAYA for detecting and measuring experimental observables in extreme conditions. The detection of particles with very low energy is nearly impossible with the standard solid targets. MAYA allows direct measurements of the observables of these particles within a target thickness large enough to overcome the low cross sections. In addition, the 3-d tracking avoids common problems of straggling with a total reconstruction of the particle trajectory. These features have proved to be extremely useful in future experimental studies near and beyond the drip lines, where large kinematic ranges are needed, including regions not accessible with the standard techniques.

The validity of MAYA as a detection system has recently encouraged the design and development of the active target detector ACTAR. This project, still under study, is intended to cover a wider spectrum of experimental energies and masses involved, and to include more reaction mechanisms for the study of new properties of exotic nuclei, like giant resonances, or two-proton decay.

Concerning the near future, further improvements in MAYA[5] may allow to increase the detection efficiency. The repetition of this experimental study with higher efficiency would add new data, refining our present results. Moreover, the study of the angular dispersion, either of the recoil Nitrogen, or of the scatter ^{3}H, would make it possible the extraction of information about the spin and parity of the ^{7}H, and about its inner structure.

In conclusion, this work stands as a further step in the study of the most exotic isotopes ever found. The existence of ^{7}H has been demonstrated for the first time, as a sharp resonance at $0.57^{+0.42}_{-0.21}$ MeV above the ^{3}H+4n threshold. This result pushes the limits of the present knowledge about nuclear interaction and structure, representing a necessary input to further development of theoretical descriptions and improving our present understanding about nuclear matter.

[5]like a possible use of the Frisch grid as another tracking monitor, the use of position Silicon detectors instead CsI crystals, or an enhancement in the pads readout system

Resumen en castellano

Introducción

Una de las principales tareas de la física nuclear consiste en explicar cómo están constituidos los núcleos. La comprensión del mecanismo que forma estas complejas estructuras requiere un conocimiento profundo de las fuerzas que actúan entre los nucleones y la disposición de éstos dentro del núcleo. A pesar del gran esfuerzo invertido para desarrollar un modelo capaz de describir todas las especies nucleares conocidas, nuestra visión es todavía muy parcial, con diferentes descripciones que únicamente son válidas en áreas concretas de la carta nuclear.

Experimentalmente, el estudio de reacciones nucleares inducidas por núcleos exóticos[6], la localización de la *drip line* de neutrones[7] y protones[8], así como la identificación y estudio de resonancias[9] más allá de esos límites, son valiosas fuentes de información que ayudan a mejorar nuestro conocimiento sobre la estructura y propiedades de la materia nuclear.

Los recientes avances técnicos en la producción de haces radiactivos abre nuevas oportunidades para el estudio de estos núcleos exóticos con diferentes técnicas[10]. El estudio de resonancias más allá de los límites de ligadura es relativamente accesible para núcleos ligeros muy ricos en neutrones, como Helio o Hidrógeno, donde la *drip line* se alcanza añadiendo tan sólo unos pocos neutrones. Además, estos núcleos

[6] núcleos que no encontramos de forma natural en nuestro entorno debido a que se desintegran rápidamente en núcleos estables.

[7] límite de ligadura, número máximo de neutrones para cada elemento con el que se construyen núcleos ligados.

[8] límite de ligadura, numero mínimo de neutrones para cada elemento con el que se construyen núcleos ligados.

[9] grupo de nucleones que juntos forman un estado definido pero no ligado.

[10] entre ellas, reacciones de $knock-out$, donde un nucleón es arrancado de un núcleo golpeado por otro; reacciones de transferencia, donde uno o más nucleones se transfieren de un núcleo a otro; reacciones de fragmentación, donde un projectil es roto en pedazos por un blanco; etc.

ofrecen la posibilidad de trabajar con los estados nucleares más exóticos en número relativo de neutrones, alcanzando $N/Z > 4$, sólo comparable a un escenario propio de las estrellas de neutrones.

A pesar de que la búsqueda de isótopos de Hidrógeno más pesados que el tritio empezó hace más de 30 años [Ade67], el mapa de los núcleos super-pesados de Hidrógeno aún no está completo debido a las dificultades asociadas con esta búsqueda. Las secciones eficaces de producción[11] extremadamente bajas relacionadas con estos isótopos hace muy complicada la búsqueda de soluciones experimentales. Aunque se ha confirmado experimentalmente la existencia de ^{4}H [Mei03b][Sid04], ^{5}H y ^{6}H [Ale84][Bel86] como resonancias, sus propiedades aún no están del todo claras. Por ejemplo, la discusión acerca del ^{5}H es particularmente intensa, con diferentes estudios, realizados principalmente en Dubna (Rusia) [Kor01] y en el GSI (Alemania) [Mei03a], que proporcionan resultados muy diferentes sobre la energía de resonancia y su anchura.

Desde el punto de vista teórico, el caso de los núcleos ligeros es especialmente interesante, ya que el número de nucleones sitúa estas especies entre dos escenarios: pueden ser vistos como sistemas de pocos cuerpos directamente afectados por la interacción nuclear, o como sistemas de varios cuerpos dominados por la estructura interna. Dependiendo de la aproximación utilizada, estos núcleos pueden describirse desde un punto macroscópico como un *core*[12] interno rodeado de neutrones externos[Bla04], o ser tratados como estructuras que presentan diferentes agrupaciones de nucleones bajo la hipótesis de *cluster*[13] en modelos microscópicos [Des01][Ara03]. Otra posible aproximación es la que utiliza cálculos $ab-initio$ donde no se hace ninguna suposición sobre la estructura interna del núcleo y se tiene en cuenta principalmente la interacción nucleón-nucleón para deducir las propiedades del sistema [Aoy04][Tim04]. Por otro lado, nuestra relativa ignorancia acerca de la interacción nuclear, que se describe normalmente como una fuerza efectiva, es una fuente adicional de incertidumbre que afecta en mayor o menor medida a cualquier modelo nuclear.

Algunos de los modelos mencionados han predicho recientemente la existencia del ^{7}H como una resonancia, aunque con diferentes propiedades. La energía asociada varía, según la descripción teórica utilizada, desde 1 MeV [Tim02] hasta 7 MeV [Aoy04]. Paralelamente, un experimento realizado por Korsheninnikov *et al.* en RIKEN (Japon) [Kor03] constituye la primera evidencia experimental de la existencia del ^{7}H como una resonancia próxima a la masa del sistema ^{3}H+4n. En nuestro

[11] la sección eficaz de producción refleja esencialmente la probabilidad de producir un cierto estado nuclear.

[12] estructura interna en un núcleo con propiedades bien definidas.

[13] grupo de nucleones que son tratados como un cuerpo cohesionado que interacciona con otros nucleones y/o otros grupos.

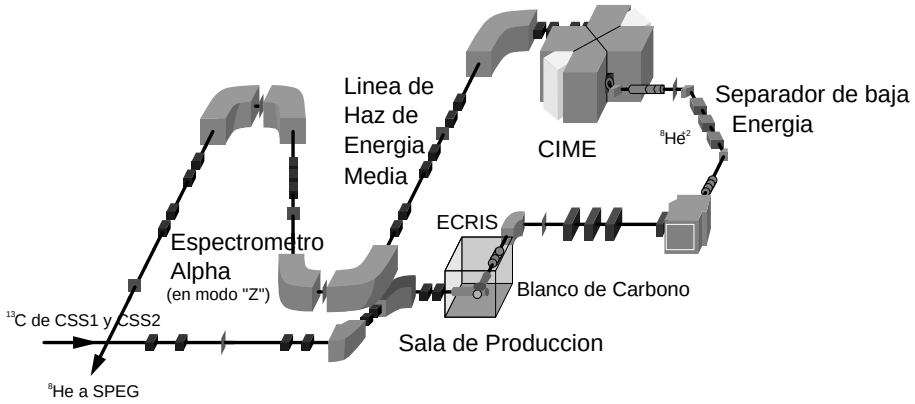

Figure 6.1: *Instalaciones de Spiral en GANIL.*

trabajo se confirma esta predicción y se caracteriza la resonancia de ^{7}H como un estado definido, alcanzando así uno de los límites en la carta nuclear.

Dispositivo experimental

El experimento fue realizado en el acelerador de iones pesados de GANIL (Francia). El haz radiactivo empleado se preparó mediante la técnica de *Separacion de Isotopos en Linea* (ISOL) en las instalaciones de Spiral (figura 6.1), donde los núcleos de un haz primario de ^{13}C se fragmentan al reaccionar con un blanco grueso de ^{12}C, produciendo diferentes especies nucleares. El haz secundario de ^{8}He se extrae y selecciona, para ser acelerado a continuación hasta una energía de 15.4A MeV en el ciclotrón CIME, con una tasa aproximada de 10^4 pps durante las dos semanas de duración del experimento. Los núcleos de ^{8}He son enviados contra un blanco gaseoso de ^{12}C. Cuando uno de los proyectiles de ^{8}He colisiona contra un núcleo de ^{12}C, éste le puede transferir un protón, produciendo ^{7}H en forma de resonancia en la reacción:

$$^{12}\mathrm{C}\ \left(\ ^{8}\mathrm{He}\ ,\ ^{7}\mathbf{H}\ \rightarrow\ ^{3}\mathrm{H} + 4\mathrm{n}\ \right)\ ^{13}\mathrm{N} \tag{6.1}$$

El dispositivo experimental estuvo basado principalmente en el detector activo MAYA [Gan02][Dem03][Mit03]. Este detector funciona esencialmente como una cámara de deriva donde el gas interno de llenado empleado en la detección es, a su vez, el blanco de reacción. La medida del tiempo de deriva de los electrones creados en la ionización del gas hasta un plano de ánodos, y la carga recogida en cada una de las celdas del cátodo segmentado permite una reconstrucción en tres dimensiones

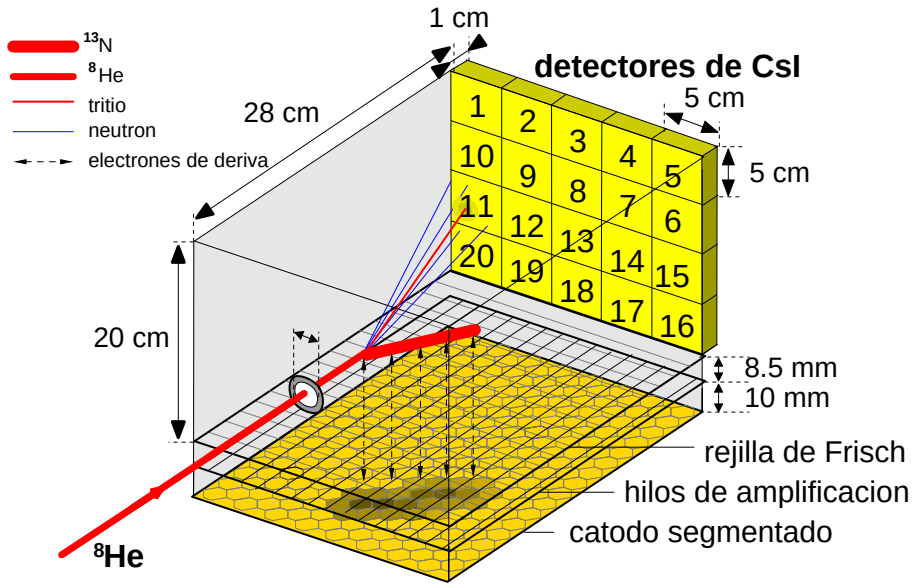

Figure 6.2: *Representación esquemática de MAYA. El suceso mostrado corresponde a una posible formación y detección de la resonancia de* ^{7}H.

de las trazas de las partículas ionizantes dentro del detector. Antes de entrar en MAYA, los proyectiles de ^{8}He atraviesan dos pequeñas cámaras de deriva, cuyo uso principal es el de monitorizar el haz. Las partículas de ^{8}He que no reaccionan con ningún núcleo del gas que llena el detector no son desviadas y siguen una trayectoria rectilínea hasta que se detienen en una pequeña pieza de metal situada en la pared posterior de MAYA, que evita la saturación del sistema de adquisición. En la parte posterior de MAYA se encuentra una matriz de detectores de cristal de Ioduro de Cesio (CsI), en los que se detienen e identifican aquellos productos de reacción que escapan del volúmen activo del detector. El dispositivo experimental está descrito gráficamente en la figura 6.2

En un suceso típico de producción de ^{7}H un proyectil de ^{8}He entra en el detector y golpea el núcleo de un átomo de ^{12}C del gas de llenado, en nuestro caso C_4H_{10} con presiones de 30 y 26 mbar, y le transfiere un protón produciendo la reacción descrita en la expresión 6.1. Al tratarse de una resonancia, el ^{7}H producido se separa en un tiempo muy corto[14] en un núcleo de ^{3}H y cuatro neutrones. El tritio es detenido e identificado en uno de los veinte detectores de cristal de Ioduro de Cesio (CsI) dispuestos en la parte posterior de MAYA. Los cristales de CsI producen luz al ser atravesados por una partícula cargada. Esta luz se emite en forma de pulso con dos componentes características. Una de ellas es sensible a la carga y masa de la partícula. El análisis de la forma de la señal producida, realizado antes de que ésta sea enviada a la adquisición, permite identificar la partícula detenida en el cristal

[14] del orden de 10^{-21} s.

de CsI. En la figura 6.3 vemos un ejemplo de la selección de sucesos de ^{3}H realizada sobre la señal de los cristales de CsI.

Por su parte, el núcleo de Nitrógeno creado en la reacción se detiene dentro del gas del interior de MAYA mientras lo ioniza, perdiendo toda su energía en su recorrido. Los electrones arrancados de los átomos en la ionización derivan hacia un plano de hilos de amplificación, guiados por un campo eléctrico aplicado en el interior del detector. Después de atravesar una rejilla de Frisch [Fri89], que actúa como filtro, los electrones llegan a los hilos de amplificación, donde se aceleran debido al gradiente eléctrico que existe alrededor de cada hilo. Al acelerarse, los electrones ionizan el gas y crean nuevos pares de electrones y átomos con carga neta positiva que derivan hacia el cátodo segmentado, situado debajo del plano de amplificación. Este movimiento induce una carga espejo, en cada uno de las celdas, que se recoge y graba en una serie de chips especialmente diseñados. Posteriormente, los valores de carga de cada celda se envian a la adquisición cuando ésta detecta un suceso.

El proceso de inducción de carga en el cátodo segmentado crea una imagen proyectada sobre las celdas del recorrido de la partícula en el interior del detector sobre la que se calcula el ángulo de la trayectoria, así como su alcance[15]. Las proyecciones de ángulo y alcance se corrigen con el ángulo del plano de reacción, calculado con los tiempos de deriva de los electrones hasta los hilos de amplificación. A través de la relación entre la energía[16] de una partícula y el alcance de esa partícula en un gas dado, se puede identificar al Nitrógeno entre otros posibles elementos producidos en otros canales de reacción. Es importante señalar que con este dispositivo experimental y a estas energías (entre 5 MeV y 20 MeV) no es posible la separación entre isótopos del mismo elemento. La figura 6.3 muestra la selección de Nitrógeno sobre la relación carga total frente a alcance.

Análisis de datos. Caracterización de la resonancia de ^{7}H

La identificación de ^{3}H en los detectores de CsI en coincidencia con la identficación de un isótopo de Nitrógeno detenido en el interior de MAYA nos permite seleccionar los canales de transferencia de, al menos, un protón. Es decir: $^{12}\mathrm{C}(^{8}\mathrm{He},^{3,4,5,6,7}\mathrm{H})^{17,16,15,14,13}\mathrm{N}$. Para distinguir los diferentes canales reconstruimos la cinemática asociada a cada uno.

[15] distancia recorrida por la partícula en el gas antes de detenerse al perder completamente su energia.

[16] la energía es, en este caso, proporcional a la carga total recogida.

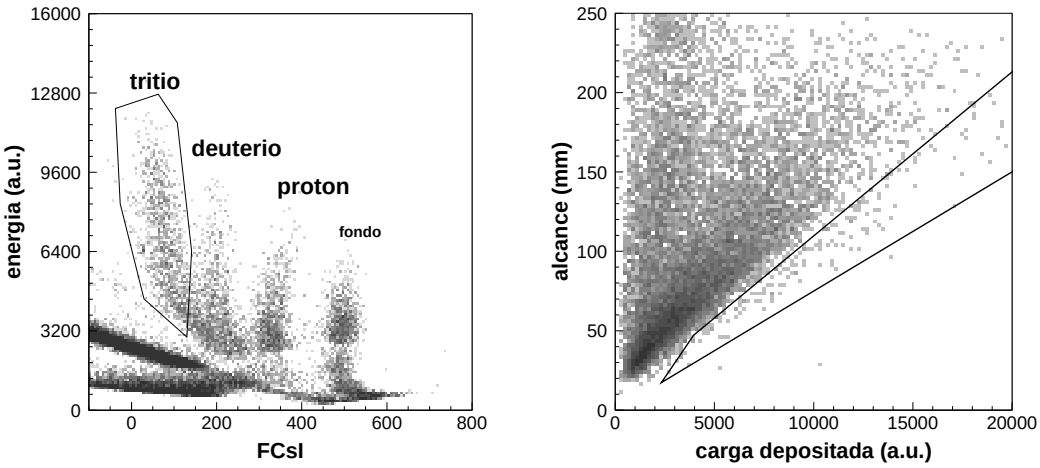

Figure 6.3: *Panel izquierdo: Identificación y selección de ^3H en un cristal de CsI, Cada linea representa un isótopo de Hidrógeno. Panel izquierdo: Identificación y selección de Nitrógeno en una gráfica del alcance frente a carga total.*

Las reacciones de transferencia son procesos binarios en los que las energías y ángulos de los dos productos están unívocamente relacionados a través de la cinemática. Debido a que uno de los productos, el ^{7}H, se desintegra antes de ser detectado, extraemos la información cinemática de la energía y ángulo del Nitrógeno, medidos a partir de la reconstrucción de su trayectoria en MAYA. Este procedimiento permite una extracción limpia de la información sin procesos intermedios entre la formación de la resonancia y la medida de estos observables.

En el panel izquierdo de la figura 6.4 se muestra con una línea continua la cinemática de la formación del ^{7}H calculada para la energía y ángulo del ^{13}N, con dos líneas de referencia representando +4 y MeV -4 MeV alrededor de la masa del sistema ^{3}H+4n. Podemos observar algunos puntos experimentales del total de la selección ^{3}H+Nitrógeno acumulándose alrededor de la cinemática. Ésta es una clara señal de un estado definido y representa la primera confirmación de la producción y existencia del ^{7}H.

El panel de la derecha representa el espectro de energía de excitación para los mismos datos experimentales. La energía de excitación se define como la diferencia entre la masa del ^{7}H, calculada a través de la conservación de energía y momento en la reacción, y una masa de referencia correspondiente, en este caso, al sistema ^{3}H+4n. En este espectro de energía de excitación podemos identificar los sucesos asociados a la producción del ^{7}H formando un pico muy cerca del nivel de ^{3}H+4n,

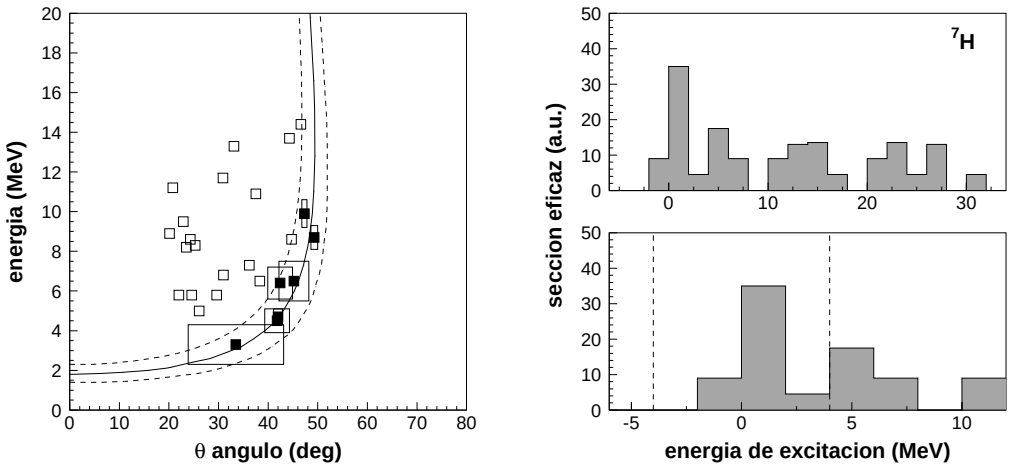

Figure 6.4: *Panel izquierdo: cinemática de la reacción* $^{12}C(^{8}He,^{7}H)^{13}N$ *calculada para el* ^{13}N*. Los puntos corresponden a los sucesos seleccionados como* ^{3}H*+Nitrógeno. Las lineas discontinuas marcan +4 MeV y -4 MeV alrededor de la cinemática. Panel derecho: energía de excitación calculada para el canal de reacción de* ^{7}H*.*

representado por 0 MeV.

La separación del canal de producción del ^{7}H del resto de canales de producción de otras resonancias de Hidrógeno se realiza con el cálculo de la energía de excitación asociado a cada canal e identificando el correspondiente pico de producción. En la figura 6.5 vemos los resultados para ^{6}H y ^{5}H respectivamente.

Se han identificado positivamente siete sucesos correspondientes al ^{7}H durante el análisis de los datos experimentales. La sección eficaz de producción del ^{7}H se ha determinado como el número de sucesos detectados, normalizado al número de proyectiles incidentes y de átomos disponibles en el blanco. El resultado final es corregido por la eficiencia de detección del sistema experimental, así como por pérdidas debidas al tiempo muerto de la adquisición[17]. Finalmente, hemos obtenido una sección eficaz de $\mathrm{d}\sigma/\mathrm{d}\Omega = 40.1^{+58.0}_{-30.6}$ μb/sr dentro de la covertura angular de MAYA, estimada para este experimento[18] en $\sim 10-45$ deg en el sistema de referencia del centro de masas. La eficiencia de detección se ha estimado, para los canales de reacción estudiados, en un 28 ± 3 %. Esta baja eficiencia es el resultado de las condiciones extremas de nuestro experimento. La extracción de la información, prin-

[17]durante el tiempo muerto la adquisición está grabando o procesando un suceso y es *ciega* a la llegada de nuevos sucesos.

[18]la covertura angular depende de la geometría del detector y de la cinemática de la reacción.

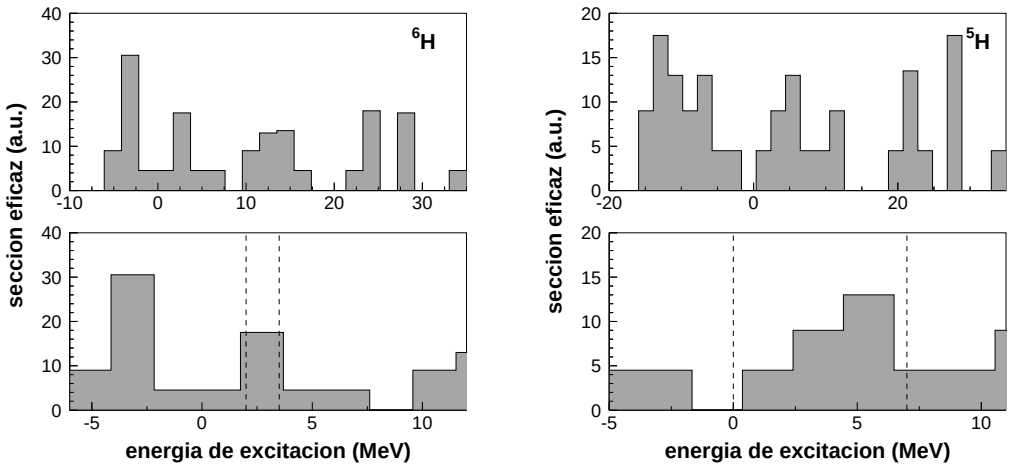

Figure 6.5: *Panel izquierdo: energía de excitación asociada con* $^{12}C(^{8}He,^{6}H)^{14}N$. *Panel derecho: energía de excitación asociada con* $^{12}C(^{8}He,^{5}H)^{15}N$. *Las líneas discontinuas marcan las regiones donde se esperan las resonancias de* ^{6}H *y* ^{5}H *respectivamente.*

cipalmente de la partícula detenida en el gas, con energías en el límite de detección, ha forzado el empleo de un gran número de filtros y fuertes restricciones en la selección de sucesos aceptables. Es importante decir que este experimento habría sido imposible de realizar con las técnicas habituales de detección con blancos sólidos.

La caracterización del ^{7}H como resonancia se realiza a partir de la determinación de la energía de la resonancia y su anchura. La energía de resonancia está asociada con la masa del sistema, y representa la energía que se debe aportar para mantenerlo unido. La anchura, por su parte, indica el tiempo que la resonancia necesita para desintegrarse en un estado más estable, y puede, por tanto, dar información sobre el mecanismo de desintegración. Debido a que el sistema de ^{7}H no está ligado, su masa es mayor que la asociada a sus componentes por separado, por esa razón aparece el pico en valores positivos de la energía de excitación en la figura 6.4. La forma de la resonancia se describe con una distribución de Breit-Wigner [Bre36] modificada para tener en cuenta la influencia de la energía del sistema en la anchura de la resonancia:

$$\sigma(E) = \sigma_0 \frac{\Gamma \sqrt{\frac{E}{E_R}}}{(E - E_R)^2 + \frac{\Gamma^2}{4}\frac{E}{E_R}} \tag{6.2}$$

donde la sección eficaz de producción $\sigma(E)$ depende de la energía de excitación E a través de la anchura Γ, y de la energía de resonancia E_R. El factor de normalización

σ_0 se determina con la sección eficaz total.

La distribución de Breit-Wigner se ajusta a los valores experimentales de energía de excitación a través de un proceso multiparamétrico de *Máxima Verosimilitud*, el cuál es especialmente adecuado para conjuntos de estadística extremadamente baja. En este proceso se calcula la probabilidad individual de cada uno de los puntos experimentales, y se modifican los parámetros de la distribución hasta maximizar el producto resultante. De esta forma es posible utilizar el error asociado a cada uno de los puntos extraídos del análisis. La anchura experimental de la resonancia es el resultado de la convolución entre la anchura física de la distribución de Breit-Wigner y el error asociado a cada suceso. El proceso de *Máxima Verosimilitud* separa ambas contribuciones en el resultado final. Como indicación, los errores asociados a las energías de resonancia de los puntos medidos tienen un valor típico de ~ 2.5 MeV.

El proceso de ajuste nos da como resultado final una energía de resonancia de $E_R = 0.57^{+0.42}_{-0.21}$ MeV sobre la masa de ^{3}H+4n y una anchura de $\Gamma = 0.09^{+0.94}_{-0.06}$ MeV. En la figura 6.6 podemos ver el espectro de energía de excitación para los datos experimentales, junto con la distribución de Breit-Wigner resultante.

Discusión de los resultados

La energía de resonancia resultante de nuestro análisis está cualitativamente de acuerdo con el resultado previo de Korsheninnikov *et al.* [Kor03], en el que un brusco incremento de la sección eficaz en la reacción ^{8}He(p,pp) aparecía muy cerca del umbral representado por la masa del sistema ^{3}H+4n. La proximidad de la energía necesaria para la formación del ^{7}H a este umbral reduce enormemente la posibilidad de existencia de un isótopo de Hidrógeno más pesado. Muy probablemente, el ^{7}H represente el limite que podemos alcanzar más allá de la *drip line* de neutrones.

La comparación con la anchura de la resonancia es mucho más difícil de realizar ya que los autores no ofrecen ningun dato, ciñéndose a mostrar la distribución experimental. Las mayores dificultades para definir una anchura provienen principalmente de la influencia del espacio de fase[19] y de probables contribuciones de otros canales de reacción. De cualquier forma, Korsheninnikov ya había predicho en sus trabajos una anchura muy estrecha para este estado nuclear [Kor05], debido a la probable desintegración en ^{3}H+n+n+n+n. Ésta sería una desintegración en cuatro

[19]contribución debida al reparto de energía y momento entre los mismos productos de reacción cuando no se ha producido la resonancia.

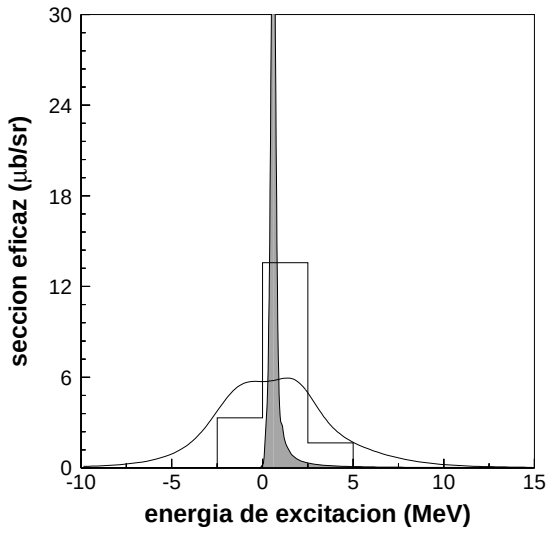

Figure 6.6: *Las líneas continuas marcan la distribución experimental en forma de histograma con canales de 2.5 MeV, y distribución de probabilidad calculada con la suma de cada suceso representado como una distribución gaussiana centrada en el valor medido con una anchura igual al error estimado. La distribución gris corresponde a la función de Breit-Wigner que mejor reproduce los datos experimentales.*

neutrones[20], y constituiría un caso único entre todas las especies nucleares. En el futuro se necesitarán nuevos estudios acerca del ^{7}H que confirmen estos resultados y puedan también aclarar este nuevo y extremadamente interesante canal de desintegración, que quizás arroje también algo de luz sobre el actual debate acerca de la posible existencia de un estado tetraneutrón ^{4}n [Mar02][Pie03].

Desde el punto de vista experimental, es interesante mencionar otro trabajo posterior en el que se intentó una detección directa del núcleo de ^{7}H [Gol04a]. Golovkov *et al*. pusieron a prueba la remota posibilidad de la existencia de un estado de ^{7}H con una vida media de 10^{-9} s, tiempo suficiente para ser detectado. Finalmente, la búsqueda no reveló ninguna traza de ese estado. De cualquier forma, la descripcion teórica del sistema de ^{7}H de este trabajo asocia anchuras reducidas para bajas energías de resonancia. Nuestra caracterización de la resonancia sigue una tendencia similar, aunque cuantitativamente la anchura obtenida sea alrededor de diez veces mayor que la predicha por Golovkov *et al*.

Por otro lado, nuestro conocimiento sobre el mecanismo de reacciones de transferencia se puede poner a prueba comparando la sección eficaz medida experimentalmente con las predicciones hechas con modelos de reacciones directas. En concreto, la sección eficaz medida en nuestro trabajo coincide con los cálculos hechos con el programa FRESCO [Tho06], basado en aproximaciones como *Aproximación de Onda Distorsionada de Born* (DWBA), o formulación en matrices-R [21]. El valor medio de la sección eficaz diferencial calculada FRESCO en el rango angular experimental es $\mathrm{d}\sigma/\mathrm{d}\Omega = 56.9$ μb/sr, a comparar con el resultado experimental $\mathrm{d}\sigma/\mathrm{d}\Omega = 40.1^{+58.0}_{-40.0}$ μb/sr.

Respecto a las descripciones teóricas, parece que los trabajos $ab-initio$ con desarrollo en bases hyperesféricas sobre el modelo de capas dan las predicciones que más se apróximan a nuestros resultados experimentales. De cualquier forma es muy difícil concluir que es ésta la mejor aproximación debido a las diferentes predicciones en diferentes versiones del mismo modelo (véase por ejemplo [Tim02] y [Tim04]). A pesar de todo, las aproximaciones hechas partiendo de las hipótesis $ab-initio$ son las más prometedoras, ya que su descripción de la interacciones nucleares parece la más realista, y todos los autores coinciden en señalarlas como la mejor solución, a la vez que prometen futuras mejoras.

[20] en cualquiera de sus posibles versiones: ^{3}H+n+n+n+n, ^{3}H+^{2}n+^{2}n, ^{3}H+^{4}n, etc.

[21] Estudios acerca de métodos sobre reacciones directas pueden ser encontrados en [Fes74] o [Sat83].

¿Cuántos neutrones puede mantener ligados un protón?

Con este trabajo hemos demostrado la capacidad de MAYA para detectar y medir observables experimentales en condiciones extremas. La detección de partículas con muy baja energía, como en nuestro experimento, es prácticamente imposible de realizar con los detectores sólidos normalmente usados. Además, el uso de un volumen apreciable de gas, lo que significa un gran número de blancos de reacción, compensa las bajas secciones eficaces. Las propiedades de MAYA resultan muy útiles para la realización de futuros experimentos con núcleos exóticos, donde se necesita cubrir una gran región cinemática, incluidas zonas no accesibles con las técnicas habituales.

La validez de MAYA como sistema de detección ha impulsado recientemente el diseño del nuevo detector ACTAR, también basado en el concepto de blanco activo. Este proyecto, aún en desarrollo, pretende cubrir un espectro de energías y masas involucradas más amplio, e incluir más mecanismos de reacción en el estudio de nuevas propiedades de núcleos exóticos, como resonancias gigantes, o la desintegración en dos protones.

Sobre el futuro inmediato, se espera incrementar la eficiencia de deteccion de MAYA con nuevas modificaciones[22], lo que permitirá refinar los resultados obtenidos hasta ahora. Además, el estudio de las distribuciones angulares, tanto del Nitrogeno como del ^{3}H dispersado, haría posible la obtención de información sobre el espín y paridad del ^{7}H, y sobre su estructura interna.

En conclusión, nuestro trabajo se muestra como un paso más allá en el estudio de las especies nucleares más exoticas jamás encontradas. Estos resultados aumentan los límites de nuestro conocimiento sobre interacción y estructura nuclear, representando el necesario aporte para desarrollar descripciones teóricas y mejorando nuestra comprensión acerca de la materia nuclear.

Un protón puede mantener ligados hasta seis neutrones. En general, podemos decir $N/Z \leq 6$.

[22] como un posible uso de la rejilla de Frisch para completar la reconstrucción, el uso de detectores de Silicio como detectores de posición, o mejoras en la lectura de las celdas del cátodo.

Appendix A

Estimation of the errors

During this work the uncertainties associated to each calculated parameter were generally estimated on the base of a *Central Limit* behaviour, where the variance σ_y of a linear combination of random variables x_i, is given by[1]:

$$\sigma_y^2 = \sum_{i=1}^{n} c_i^2 \sigma_{x_i}^2 \tag{A.1}$$

In general, the parameters (y) calculated during this work are not a linear combination of other variables (x_i), but more complicated dependences. For small variations of x_i around a measured central value $y_{central}$ the linear factors c_i^2 can be approximated as:

$$c_i \approx \left(\frac{\partial y}{\partial x_i} \right) \tag{A.2}$$

finally, we get the *error propagation equation*, mainly used in our analysis:

$$\sigma_y^2 = \sum_{i=1}^{n} \sigma_{x_i}^2 \left(\frac{\partial y}{\partial x_i} \right)^2 + \sum_{i \neq j}^{n} \sigma_{x_{ij}}^2 \left(\frac{\partial y}{\partial x_i} \right) \left(\frac{\partial y}{\partial x_j} \right) \tag{A.3}$$

[1] an extensive review on Probability and Uncertainty can be found in [D'Ag95]

A.1 Data analysis uncertainties

Determination of the reaction plane uncertainty

The uncertainty associated to the reaction plane ϕ angle, $d\phi$, is calculated from the uncertainty of the fitted slope, $d\tan\phi$ as:

$$d\phi = \frac{\partial\phi}{\partial\tan\phi}\, d\tan\phi = \frac{1}{1+\tan^2\phi} d\tan\phi \tag{A.4}$$

Calculation of the recoil angle uncertainty

The estimated uncertainty for the θ angle calculation contains three components. The error associated with the fit of the projected trajectory, $d\theta_{2d}$, the dependence on the ϕ angle, and the uncertainty in the angle of the projectile direction, $d\theta_{beam} = 0.38$ deg:

$$(d\theta)^2 = \left(\frac{\partial\theta}{\partial\theta_{2d}}\, d\theta_{2d}\right)^2 + \left(\frac{\partial\theta}{\partial\phi}\, d\phi\right)^2 + (d\theta_{beam})^2 \tag{A.5}$$

the different components are the derivatives from equation

$$\theta = \mathrm{abs}\left[\arctan\left(\tan\theta_{2d}\sqrt{1+\tan^2\phi}\right)\right] \tag{A.6}$$

resulting in:

$$\frac{\partial\theta}{\partial\theta_{2d}}\, d\theta_{2d} = \frac{(1+\tan^2\theta_{2d})\sqrt{1+\tan^2\phi}}{1+\tan^2\theta}\, d\theta_{2d} \tag{A.7}$$

$$\frac{\partial\theta}{\partial\phi}\, d\phi = \frac{\tan\theta\tan\phi}{1+tan^2\theta}\, d\phi \tag{A.8}$$

Calculation of the recoil energy uncertainty

The range is extracted from the projected range and the measured θ_{2d} and ϕ angles with:

$$R = R_{2d}\sqrt{1 + \tan^2\phi \sin^2\theta_{2d}} \tag{A.9}$$

The associated uncertainty for the range calculation depends on the uncertainty of the ϕ and θ_{2d} calculations, and on the uncertainty of the determination in the projected range R_{2d}:

$$(dR)^2 = \left(\frac{\partial R}{\partial R_{2d}}\, dR_{2d}\right)^2 + \left(\frac{\partial R}{\partial \phi}\, d\phi\right)^2 + \left(\frac{\partial R}{\partial \theta_{2d}}\, d\theta_{2d}\right)^2 \tag{A.10}$$

the components are calculated differentiating the equation A.9:

$$\frac{\partial R}{\partial R_{2d}}\, dR_{2d} = \sqrt{1 + \tan^2\phi \sin^2\theta_{2d}}\, dR_{2d} \tag{A.11}$$

$$\frac{\partial R}{\partial \phi}\, d\phi = \frac{R \cdot \tan\phi \sin\theta_{2d}}{1 + \tan^2\phi \sin^2\theta_{2d}} \sin\theta_{2d}(1 + \tan^2\phi)\, d\phi \tag{A.12}$$

$$\frac{\partial R}{\partial \theta_{2d}}\, d\theta_{2d} = \frac{R \cdot \tan\phi \sin\theta_{2d}}{1 + \tan^2\phi \sin^2\theta_{2d}} \tan\phi \cos\theta_{2d}\, d\theta_{2d} \tag{A.13}$$

The translation from range to energy is calculated with the code TRIM [Zie99][Sri05]. The predictions of the code are fitted to a second-order polynomial function. Finally the uncertainty associated with the calculation of the energy is determined as:

$$(dE)^2 = \left(\frac{\partial E}{\partial P}\, dP\right)^2 + \left(\frac{\partial E}{\partial R}\, dR\right)^2 + (\delta E)^2 \tag{A.14}$$

where dP is the pressure uncertainty. The lecture of the gas pressure was done with an estimated precision of 10%, then $dP = 0.1P$. The partial derivative $\partial E/\partial P$ is numerically calculated as:

$$\frac{\partial E}{\partial P}\, dP \simeq \frac{E(R)_{(P)} - E(R)_{(1.1 \cdot P)}}{0.1 \cdot P}\, dP \simeq 0.01 \cdot R \tag{A.15}$$

The term corresponding to the R uncertainty of equation A.14 is:

$$\frac{\partial E}{\partial R}\, dR = (A_1 - 2A_2 R)\, dR \tag{A.16}$$

being A_1 and A_2 the lineal and square factors of the $E(R)$ polynomial function corresponding to each pressure.

The δE component corresponds to the uncertainty of the TRIM code, which is estimated in $\sim$3 % [Zie99].

Normalization to target thickness and incident projectiles uncertainties

The normalization to target thickness is calculated as:

$$N_{^{12}\mathrm{C}} = D_{isobutane} \cdot L \cdot R_C \cdot N_A \cdot A^{-1}_{isobutane} \tag{A.17}$$

where the sources of uncertainty are the density $D_{isobutane}$ of isobutane for each pressure, with an associated uncertainty of 10 %, and the usable length of the detector L with 5 % of precision. Finally:

$$\left(\frac{dN_{^{12}\mathrm{C}}}{N_{^{12}\mathrm{C}}}\right)^2 = \left(\frac{dD_{isobutane}}{D_{isobutane}}\right)^2 + \left(\frac{dL}{L}\right)^2 \tag{A.18}$$

The estimation of the total number of ^{8}He projectiles entering in MAYA depends on the number of beam triggers (T_{beam}) multiplied by the division factor (f_{BiDiv}), the efficiency of the detector (ε_{MDC}), and on the number of lost projectiles between the MDC and the entrance of MAYA estimated in $\alpha_{beam} = 2 \pm 2$ %.

$$N_{^{8}\mathrm{He}} = \frac{T_{beam} \cdot f_{BiDiv}}{(1 - \alpha_{beam}) \cdot \varepsilon_{MDC}} \tag{A.19}$$

the corresponding uncertainty is obtained through the derivatives and the statistical uncertainty $\sqrt{N_{^{8}\mathrm{He}}}$:

$$(dN_{^8\mathrm{He}})^2 = \left(\frac{\partial N_{^8\mathrm{He}}}{\partial \alpha_{beam}}\, d\alpha_{beam}\right)^2 + \left(\frac{\partial N_{^8\mathrm{He}}}{\partial \varepsilon_{MDC}}\, d\varepsilon_{MDC}\right)^2 + \left(\sqrt{N_{^8\mathrm{He}}}\right)^2 \tag{A.20}$$

from equation A.19:

$$\frac{\partial N_{^8\mathrm{He}}}{\partial \alpha_{beam}}\, d\alpha_{beam} = \frac{N_{^8\mathrm{He}}}{(1-\alpha_{beam})}\, d\alpha_{beam} \tag{A.21}$$

$$\frac{\partial N_{^8\mathrm{He}}}{\partial \varepsilon_{MDC}}\, d\varepsilon_{MDC} = \frac{N_{^8\mathrm{He}}}{\varepsilon_{MDC}}\, d\varepsilon_{MDC} \tag{A.22}$$

with an uncertainty on the efficiency of $d\varepsilon_{MDC} = 1$ % (see section 3.1.2).

A.2 Characterization results uncertainties

Calculation of the excitation energy uncertainty

The excitation energy is calculated as:

$$E^{exc} = m_{^7\mathrm{H}} - m_{(^3\mathrm{H}+4\mathrm{n})} \tag{A.23}$$

with the mass $m_{^7\mathrm{H}}$:

$$m^2_{^7\mathrm{H}} = (E_{^8\mathrm{He}} + E_{^{12}\mathrm{C}} - E_{^{13}\mathrm{N}})^2 - |\vec{p}_{^7\mathrm{H}}|^2 \tag{A.24}$$

and the momentum $\vec{p}_{^7\mathrm{H}}$:

$$|\vec{p}_{^7\mathrm{H}}|^2 = |\vec{p}_{^8\mathrm{He}}|^2 + |\vec{p}_{^{13}\mathrm{N}}|^2 - 2|\vec{p}_{^8\mathrm{He}}||\vec{p}_{^{13}\mathrm{N}}|\cos\theta \tag{A.25}$$

The uncertainty associated with E^{exc} depends on the energy of the ^{13}N recoil, its θ angle respect to the projectile, and the energy spread of the beam ($dT_{^8\mathrm{He}}$), expressed as:

$\mathbf{T(^{13}N)}$ MeV	$\theta_{\mathbf{lab}}$ deg	$\mathbf{E^{exc}}$ MeV	$\partial_{\mathbf{T(^{13}N)}}\mathbf{E^{exc}}$ MeV	$\partial_{\theta}\mathbf{E^{exc}}$ MeV	$\partial_{\mathbf{E_{beam}}}\mathbf{E^{exc}}$ MeV	$\mathbf{dE^{exc}}$ MeV
3.33±0.95	33.54±9.63	**0.99**	4.28	5.46	0.04	**6.94**
6.36±0.80	42.42±2.51	**3.32**	1.48	2.40	0.06	**2.82**
9.89±0.67	47.35±0.51	**1.92**	0.41	0.66	0.08	**0.78**
8.73±0.61	49.32±0.73	**−1.37**	0.43	0.92	0.07	**1.02**
4.49±0.55	41.77±2.50	**−0.40**	1.55	1.98	0.04	**2.52**
4.72±0.44	42.05±0.90	**0.00**	1.16	0.73	0.04	**1.38**
6.54±0.97	45.21±2.97	**0.88**	1.54	3.03	0.06	**3.40**

Table A.1: *Experimental events identified as reactions in which the ^7H resonance was produced.*

$$(dE^{exc})^2 = \left(\frac{\partial E^{exc}}{\partial T_{^{13}N}}\, dT_{^{13}N}\right)^2 + \left(\frac{\partial E^{exc}}{\partial \theta}\, d\theta\right)^2 + \left(\frac{\partial E^{exc}}{\partial T_{^8\mathrm{He}}}\, dT_{^8\mathrm{He}}\right)^2 \qquad \text{(A.26)}$$

The partial derivatives were calculated for each event as:

$$\frac{\partial E^{exc}}{\partial T_{^{13}\mathrm{N}}}\, dT_{^{13}\mathrm{N}} = \left(E_{^8\mathrm{He}} + E_{^{12}\mathrm{C}} - E_{^{13}\mathrm{N}}\frac{|\vec{p}_{^8\mathrm{He}}|\cos\theta}{|\vec{p}_{^{13}\mathrm{N}}|}\right)\frac{dT_{^{13}\mathrm{N}}}{E^{exc} + m_{(^3\mathrm{H}+4\mathrm{n})}} \qquad \text{(A.27)}$$

$$\frac{\partial E^{exc}}{\partial \theta}\, d\theta = (|\vec{p}_{^{13}\mathrm{N}}||\vec{p}_{^8\mathrm{He}}|\sin\theta)\,\frac{dT_{^{13}\mathrm{N}}}{E^{exc} + m_{(^3\mathrm{H}+4\mathrm{n})}} \qquad \text{(A.28)}$$

$$\frac{\partial E^{exc}}{\partial E_{^8\mathrm{He}}}\, dE_{^8\mathrm{He}} \simeq (E^{exc}[E_{^8\mathrm{He}}] - E^{exc}[E_{^8\mathrm{He}} + \Delta E_{^8\mathrm{He}}])\,\frac{dE_{^8\mathrm{He}}}{\Delta E_{^8\mathrm{He}}} \qquad \text{(A.29)}$$

being dE, and $d\theta$ the errors associated with the calculation of the ^{13}N energy and angle (see sections 3.2.2 and 3.2.3). The energy spread $dE_{^8\mathrm{He}}$ for a CIME beam in Spiral is estimated in ± 0.5 % [Jac03].

The excitation energy of the seven events identified as ^{7}H resonances are reviewed in table A.1 with their estimated uncertainties.

Experimental cross section uncertainty

The production cross section is:

$$\sigma_{(^7H)} = \frac{N^{rec}_{^7\mathrm{H}}}{\varepsilon_{det} F_{DT} N_{^8\mathrm{He}} N_{^{12}\mathrm{C}}} \tag{A.30}$$

The sources of uncertainty are included as follows:

$$\left(\frac{d\sigma_{(^7H)}}{\sigma_{(^7H)}}\right)^2 = \left(\frac{dN^{rec}_{^7\mathrm{H}}}{N^{rec}_{^7\mathrm{H}}}\right)^2 + \left(\frac{dF_{DT}}{F_{DT}}\right)^2 + \left(\frac{d\varepsilon_{det}}{\varepsilon_{det}}\right)^2 \tag{A.31}$$

$$+ \left(\frac{dN_{^8\mathrm{He}}}{N_{^8\mathrm{He}}}\right)^2 + \left(\frac{dN_{^{12}\mathrm{C}}}{N_{^{12}\mathrm{C}}}\right)^2 \tag{A.32}$$

The uncertainty corresponding to the dead time factor is estimated in $dF_{DT} \leq 0.01$ %, whereas $dN^{rec}_{^7\mathrm{H}} = \sqrt{N^{rec}_{^7\mathrm{H}}}$. The uncertainty of the detector efficiency is calculated in $d\varepsilon_{det} = 0.3$ %, and the normalization uncertainties are $dN_{^8\mathrm{He}} = 0.03 N_{^8\mathrm{He}}$, and $dN_{^{12}\mathrm{C}} = 0.11 N_{^{12}\mathrm{C}}$.

The differential cross section is calculated approximating a linear dependence of $\sigma_{(^7H)}$ with the solid angle Ω:

$$\sigma_{(^7H)} \simeq \left(\frac{\mathrm{d}\sigma_{(^7H)}}{\mathrm{d}\Omega}\right) \int_{\theta_{cm,i}}^{\theta_{cm,f}} \sin\theta_{cm} 2\pi \mathrm{d}\theta_{cm} \tag{A.33}$$

then the associated uncertainty is:

$$\left(\frac{d\left(\frac{\mathrm{d}\sigma_{(^7H)}}{\mathrm{d}\Omega}\right)}{\left(\frac{\mathrm{d}\sigma_{(^7H)}}{\mathrm{d}\Omega}\right)}\right)^2 = \left(\frac{d\sigma_{(^7H)}}{\sigma_{(^7H)}}\right)^2 + \left(\frac{d\int \sin\theta_{cm} 2\pi \mathrm{d}\theta_{cm}}{\int \sin\theta_{cm} 2\pi \mathrm{d}\theta_{cm}}\right)^2 \tag{A.34}$$

with

$$d\int \sin\theta_{cm} 2\pi \mathrm{d}\theta_{cm} = 2\pi\sqrt{(\sin\theta_{cm,i} d\theta_{cm,i})^2 + (\sin\theta_{cm,f} d\theta_{cm,f})^2} \tag{A.35}$$

See section 4.3.2 for details about the $d\theta_{cm,i}$ and $d\theta_{cm,f}$ uncertainties in each experimental setup.

The σ_0 factor of the Breit-Wigner distribution is deduced with the $\left(\frac{\mathrm{d}\sigma_{(^7H)}}{\mathrm{d}\Omega}\right)$ differential cross section:

$$\sigma_0 = \frac{\left(\frac{\mathrm{d}\sigma_{(^7H)}}{\mathrm{d}\Omega}\right)}{\mathscr{I}(E_R, \Gamma_0)} \tag{A.36}$$

with

$$\int \sigma_{BW} \mathrm{d}E^{exc} = \sigma_0 \int_0^{+\infty} \frac{\Gamma_0 \sqrt{\frac{E^{exc}}{E_R}}}{(E^{exc} - E_R)^2 + \frac{\Gamma_0^2}{4}\left(\frac{E^{exc}}{E_R}\right)} \mathrm{d}E^{exc} = \sigma_0 \mathscr{I}(E_R, \Gamma_0) \tag{A.37}$$

The associated uncertainty is:

$$(d\sigma_0)^2 = \left(\sigma_0 \frac{d\left(\frac{\mathrm{d}\sigma_{(^7H)}}{\mathrm{d}\Omega}\right)}{\left(\frac{\mathrm{d}\sigma_{(^7H)}}{\mathrm{d}\Omega}\right)} \right)^2 + \left(\sigma_0 \frac{d\mathscr{I}}{\mathscr{I}} \right)^2 \tag{A.38}$$

The error corresponding to the integral $\mathscr{I}$ is calculated as:

$$\begin{aligned}
(d\mathscr{I})^2 &= (\mathscr{I}(E_R, \Gamma_0) - \mathscr{I}(E_R +^+ \epsilon_{E_R}, \Gamma_0))^2 && \text{(A.39)} \\
&+ (\mathscr{I}(E_R, \Gamma_0) - \mathscr{I}(E_R -^- \epsilon_{E_R}, \Gamma_0))^2 && \text{(A.40)} \\
&+ (\mathscr{I}(E_R, \Gamma_0) - \mathscr{I}(E_R, \Gamma_0 +^+ \epsilon_{\Gamma_0}))^2 && \text{(A.41)} \\
&+ (\mathscr{I}(E_R, \Gamma_0) - \mathscr{I}(E_R, \Gamma_0 -^- \epsilon_{\Gamma_0}))^2 && \text{(A.42)}
\end{aligned}$$

Appendix B

Calculation of excitation energy

The excitation energy is defined as the difference between the mass of the resonance ($m_{^7\mathrm{H}}$) and the rest mass of the components ($m_{^3\mathrm{H}+4\mathrm{n}}$)[1]:

$$E^{exc} = m_{^7\mathrm{H}} - m_{(^3\mathrm{H}+4\mathrm{n})} \tag{B.1}$$

The calculation of E^{exc} is done through the conservation of energy and momentum. In the case of a binary reaction these can be written as:

$$E_1 + E_2 = E_3 + E_4 \tag{B.2}$$

$$\vec{p_1} + \vec{p_2} = \vec{p_3} + \vec{p_4} \tag{B.3}$$

being E_i, and $\vec{p_i}$ the energy and the momentum for projectile ^{8}He ($i = 1$), ^{12}C target ($i = 2$), ^{7}H scattered ($i = 3$), and ^{13}N recoil ($i = 4$) (see figure B.1). The energy can be expressed either as the sum of the kinetic energy (T_i) and the rest mass, $E_i = m_i + T_i$, or depending on the mass an momentum as $E_i^2 = m_i^2 + |\vec{p_i}|^2$. For the scattered particle these experssions can be written as:

$$E_3 = m_1 + T_1 + m_2 + T_2 - m_4 - T_4 \quad and \quad E_3^2 = m_3^2 + |\vec{p_3}|^2 \tag{B.4}$$

then

[1] with reduced units $c = 1$, $MeV/c = MeV$

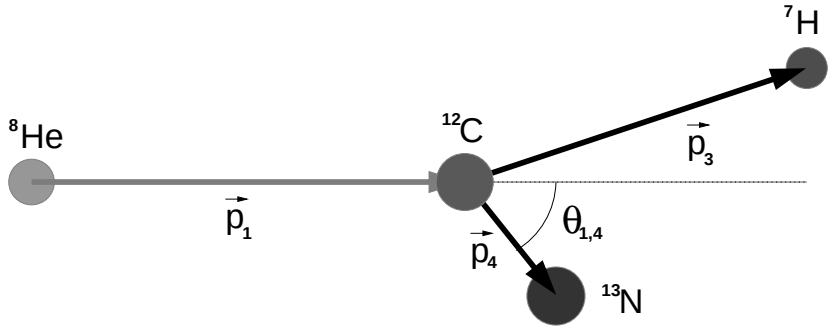

Figure B.1: $^{12}C(^{8}He,^{7}H)^{13}N$ *momenta in laboratory frame.*

$$m_3^2 = (m_1 + T_1 + m_2 + T_2 - m_4 - T_4)^2 - |\vec{p_3}|^2 \tag{B.5}$$

From the conservation of momentum:

$$|\vec{p_3}|^2 = |\vec{p_1}|^2 + |\vec{p_4}|^2 - 2|\vec{p_1}||\vec{p_4}|\cos\theta_{1,4} \tag{B.6}$$

with $\theta_{1,4}$ the angle between the projectile and recoil particles.

The application of this formula to the ^{7}H reaction gives:

$$|\vec{p}_{^7\mathrm{H}}|^2 = |\vec{p}_{^8\mathrm{He}}|^2 + |\vec{p}_{^{13}\mathrm{N}}|^2 - 2|\vec{p}_{^8\mathrm{He}}||\vec{p}_{^{13}\mathrm{N}}|\cos\theta \tag{B.7}$$

$$m_{^7\mathrm{H}}^2 = (E_{^8\mathrm{He}} + E_{^{12}\mathrm{C}} - E_{^{13}\mathrm{N}})^2 - |\vec{p}_{^7\mathrm{H}}|^2 \tag{B.8}$$

with

$$E_{^8\mathrm{He}} = (m_{^8\mathrm{He}} + T_{^8\mathrm{He}}) \tag{B.9}$$
$$E_{^{12}\mathrm{C}} = m_{^{12}\mathrm{C}} \tag{B.10}$$
$$E_{^{13}\mathrm{N}} = (m_{^{13}\mathrm{N}} + T_{^{13}\mathrm{N}}) \tag{B.11}$$
$$\tag{B.12}$$

Appendix C

The seven events of ^{7}H

Seven events have been identified as ^{7}H resonance reactions, and they are reviewed in this appendix. Each event is presented in a matrix format, where the charges collected in the pads of the segmented cathode are mapped. The drift times and charges measured in each wire are also displayed, along with the signal from the fired CsI detector. In figure C.1 we explain this matrix format.

The caption of each figure contains the projected and final recoil ranges, the calculated energy of the recoil in the corresponding gas pressure, the final excitation energy, the projected and final recoil angles, the reaction plane angle, the sum of the charges collected in the pads along the trajectory, as well as the components of the charge profile.

Some indications may be also needed: The total charge collected may not be comparable between different events, since it is possible that they correspond to different settings of voltage or adjustements in the electronics. During the analysis all filters and selections were applied separately to these sets of data.

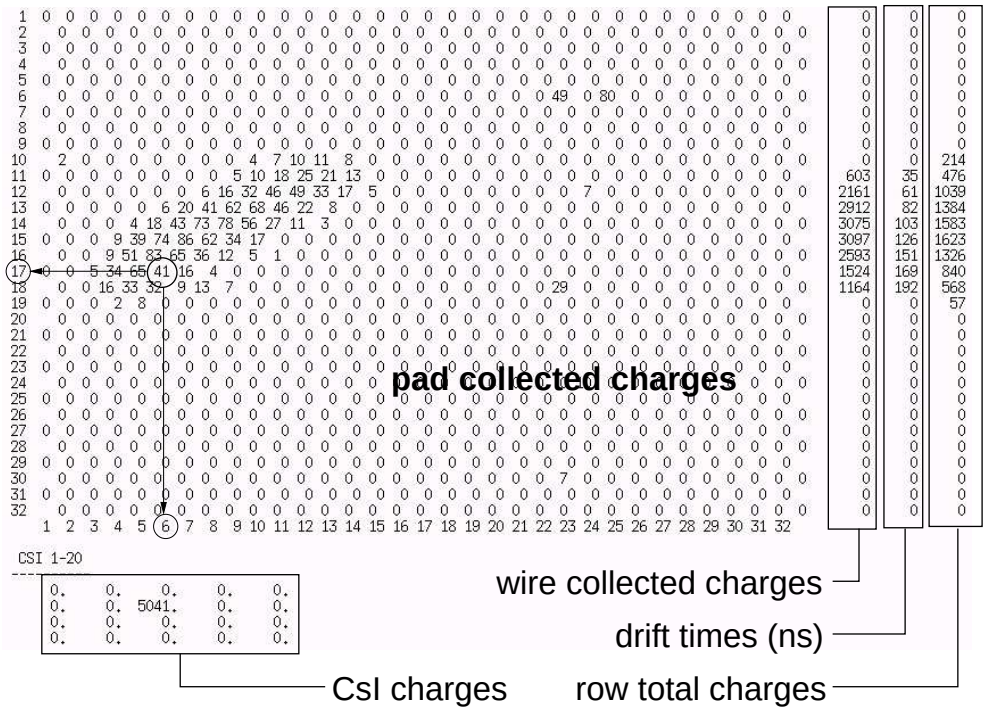

Figure C.1: *Event matrix conventions. Each pad is represented by the charge collected in. The charges and times for each wire are printed beside the corresponding line of pads with the total charge in each row of pads. The charges collected in the CsI wall are ordered in the same position as the corresponding detector. All quantities are in arbitrary units except the drift times, presented in ns. The charges in the pads are normalized in a factor 5 respect to the raw data. See figure 3.7 in section 3.2 as complementary information .*

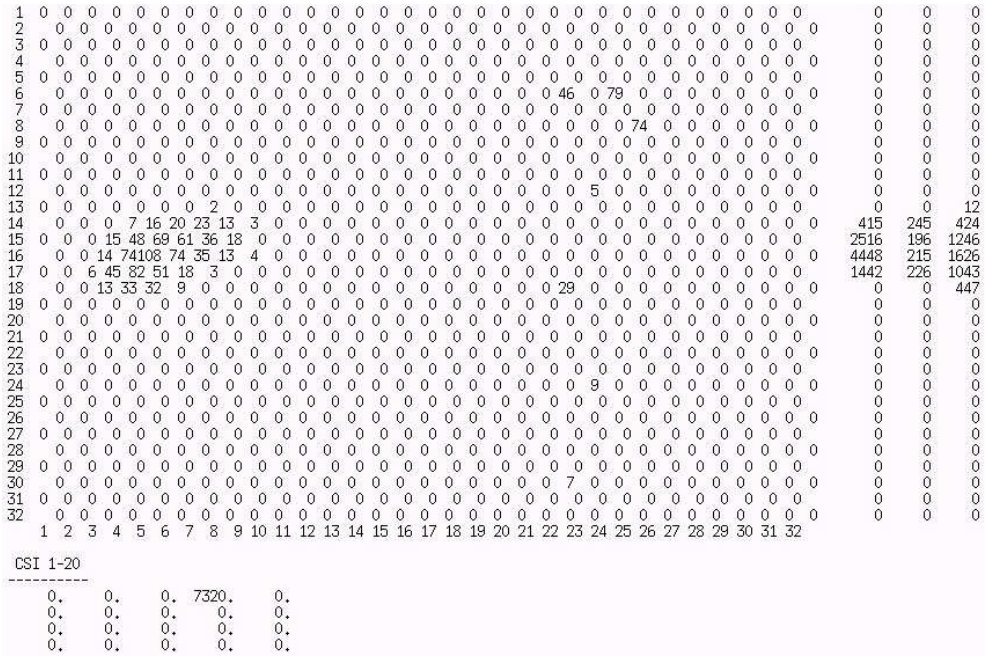

Figure C.2:
Projected range: *49.3±1.4 mm.* **Range**: *52.6±8.3 mm.*
Energy: *3.3±0.9 MeV (30 mbar).***Excitation energy**: *0.99±6.94 MeV.*
Projected angle: *27.1±2.3 deg.* **Angle**: *33.5±9.6 deg.*
Reaction plane angle: *39.4±24.6 deg.*
Total charge in pads: *4801.*
Charge profile: *103, 471, 1022, 1127, 899, 602, 365, 192, 20.*

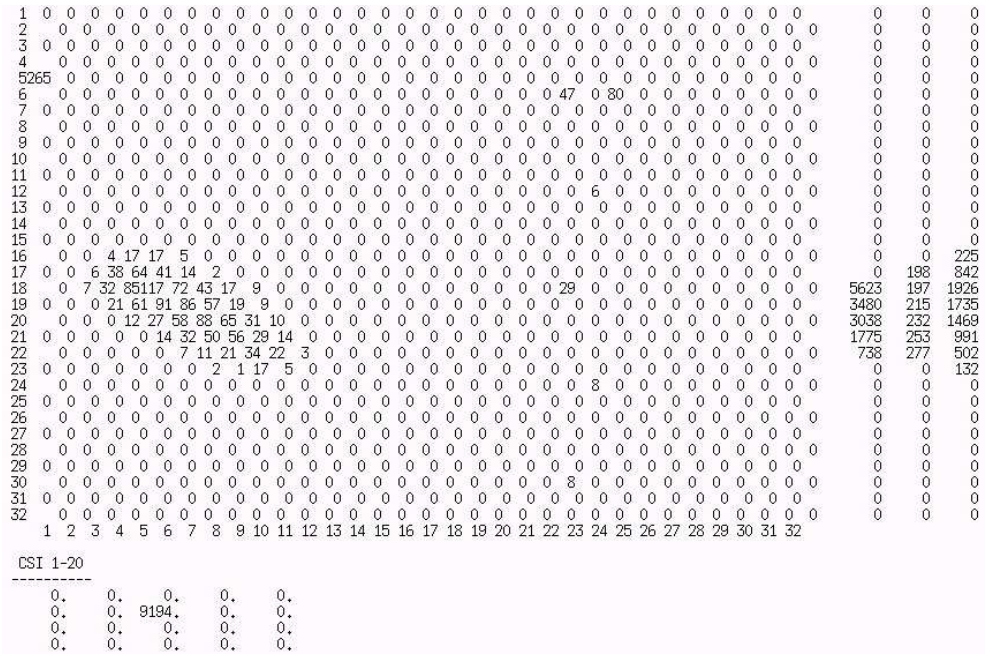

Figure C.3:
Projected range*: 71.5±1.4 mm.* **Range***: 81.2±6.4 mm.*
Energy*: 6.4±0.8 MeV (30 mbar).***Excitation energy***: 3.32±2.82 MeV.*
Projected angle*: 33.1±0.7 deg.* **Angle***: 42.4±2.5 deg.*
Reaction plane angle*: 44.5±4.9 deg.*
Total charge in pads*: 7827.*
Charge profile*: 94, 444, 944, 1186, 1033, 1026, 1017, 784, 606, 377, 272, 44.*

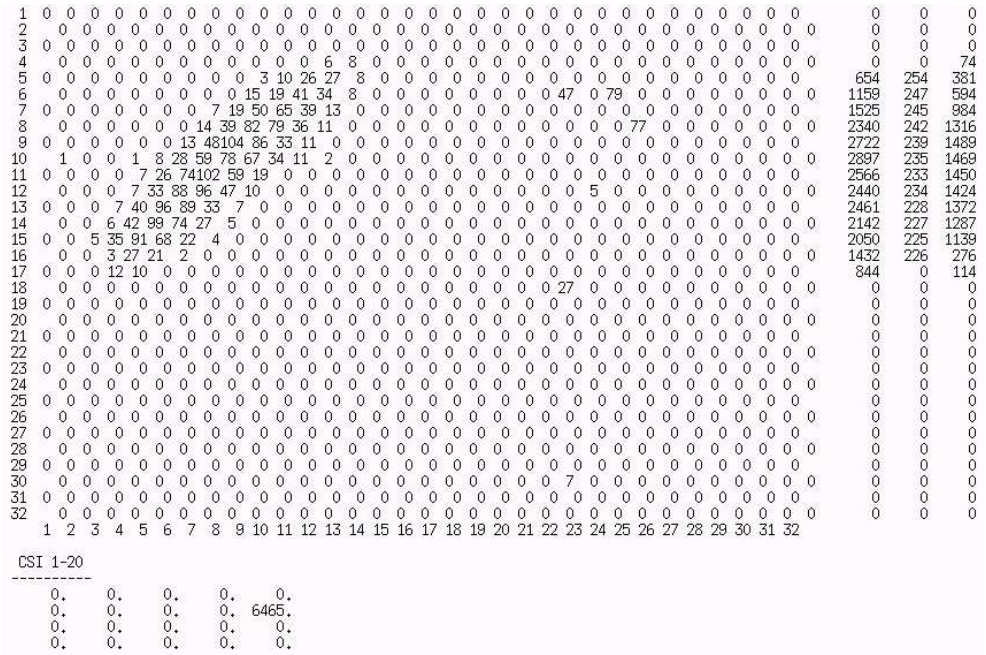

Figure C.4:
Projected range*: 116.0±1.4 mm.* **Range***: 116.7*1.6 *mm.*
Energy*: 9.9±0.7 MeV (30 mbar).***Excitation energy***: 1.92±0.78 MeV.*
Projected angle*: 47.0*0.4 *deg.* **Angle***: 47.4±0.5 deg.*
Reaction plane angle*: 8.7±3.4 deg.*
Total charge in pads*: 13352.*
Charge profile*: 108, 401, 815, 1092, 1173, 1227, 1199, 1153, 1058, 1186, 1122, 953, 681, 513, 376, 213, 82.*

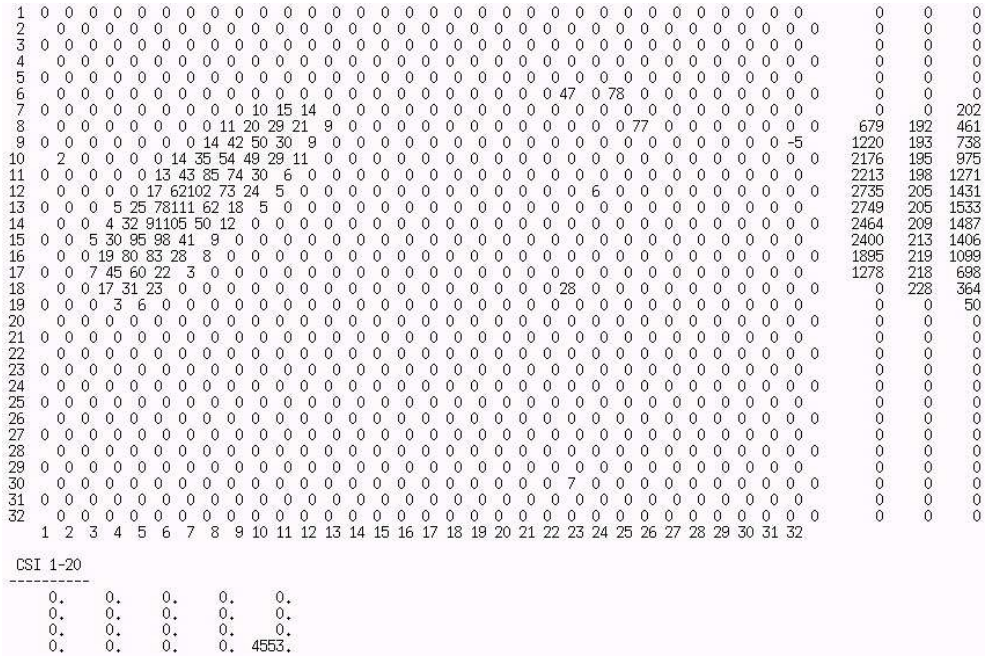

Figure C.5:
Projected range*: 103.4±1.4 mm.* **Range***: 104.7±1.9 mm.*
Energy*: 8.7±0.6 MeV (30 mbar).***Excitation energy***: -1.37±1.02 MeV.*
Projected angle*: 48.7±0.6 deg.* **Angle***: 49.3±0.7 deg.*
Reaction plane angle*: 11.8±4.3 deg.*
Total charge in pads*: 11722.*
Charge profile*: 145, 542, 997, 1197, 1237, 1258, 1241, 1177, 1060, 869, 699, 538, 407, 232, 123.*

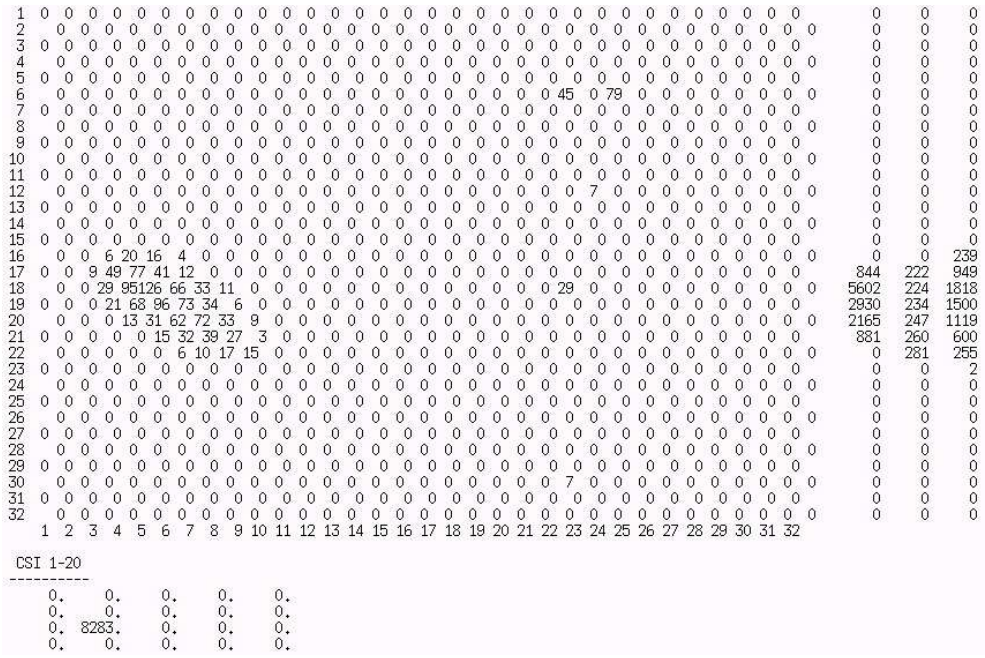

Figure C.6:
Projected range: *58.5±1.4 mm.* **Range**: *63.4±4.0 mm.*
Energy: *4.5±0.6 MeV (30 mbar).***Excitation energy**: *-0.40±2.52 MeV.*
Projected angle: *36.1±0.6 deg.* **Angle**: *41.8±2.5 deg.*
Reaction plane angle: *35.3±6.9 deg.*
Total charge in pads: *6486.*
Charge profile: *77, 501, 1054, 1276, 1035, 927, 788, 453, 274, 101.*

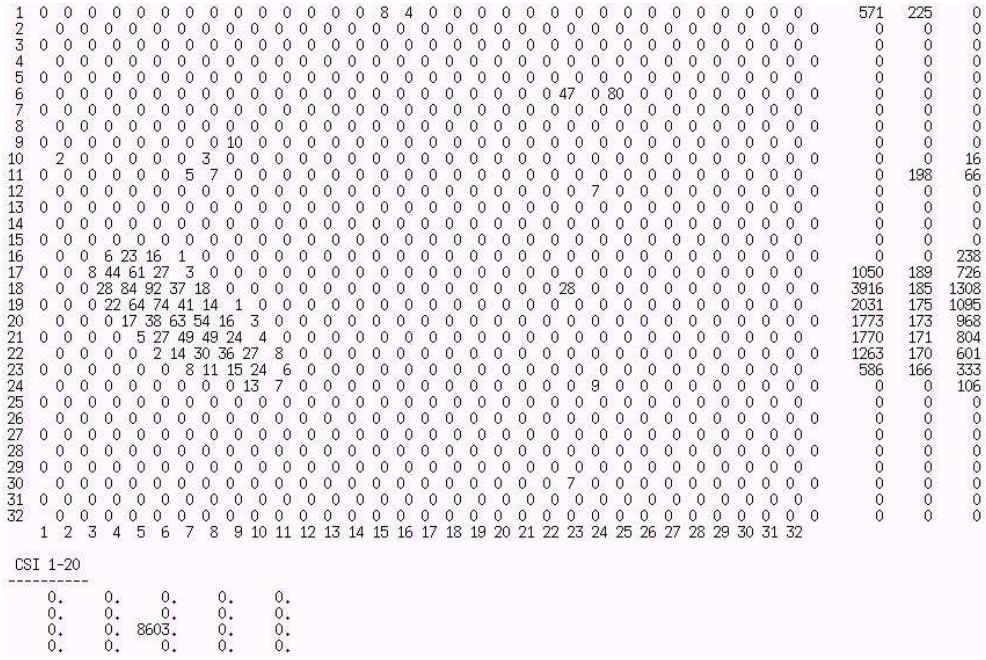

Figure C.7:
Projected range*: 76.0±1.4 mm.* **Range***: 76.6±1.8 mm.*
Energy*: 4.7±0.4 MeV (26 mbar).***Excitation energy***: 0.00±1.38 MeV.*
Projected angle*: 41.6±0.6 deg.* **Angle***: 42.0±0.9 deg.*
Reaction plane angle*: 10.6±6.9 deg.*
Total charge in pads*: 6183.*
Charge profile*: 76, 484, 922, 1017, 793, 769, 666, 530, 385, 234, 235, 72.*

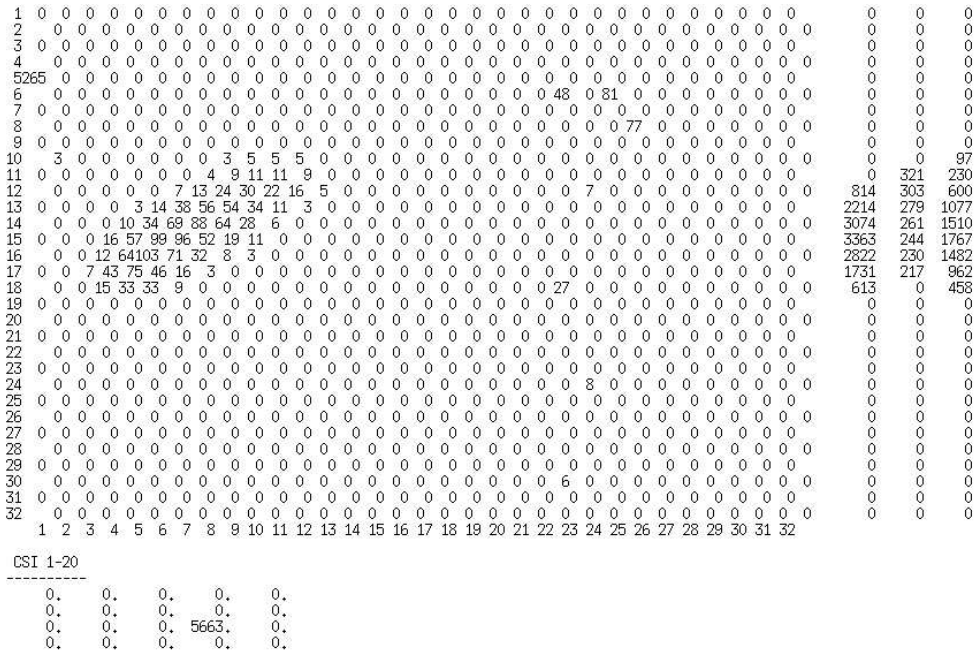

Figure C.8:
Projected range*: 77.6±1.4 mm.* **Range***: 97.1±9.4 mm.*
Energy*: 6.5±1.0 MeV (30 mbar).***Excitation energy***: 0.88±3.40 MeV.*
Projected angle*: 33.9±0.6 deg.* **Angle***: 45.2±3.0 deg.*
Reaction plane angle*: 48.2±5.2 deg.*
Total charge in pads*: 8185.*
Charge profile*: 112, 447, 948, 1138, 1125, 1085, 971, 783, 619, 419, 253, 186, 99.*

Bibliography

[Ade67] E.G. Adelberger et al., *Phys. Lett.* B**25**(1967) 595.

[Ale84] D.V. Aleksandrov et al., *Sov. Jour. Nucl. Phys.* **39** (1984) 323 (as cited in [Til02])

[Aoy04] S. Aoyama and N. Itagaki, *Nucl. Phys.* A**738** (2004) 362.

[Ara03] K. Arai, *Phys. Rev.* C**68** (2003) 034303.

[Bar95] E. Baron, J. Gillet, and M. Ozille, *Nucl. Instr. and Meth.* A**362** (1995) 90

[Bar03] N. Barnea, W. Leidemann, and G. Orlandini, *Phys. Rev.* C**67** (2003) 054003.

[Bay81] D. Baye and N. Pecher, *Bull. Cl. Sci.* Acad. R. Belg. **67** (1981) 835.

[Bel86] A.V. Belozyorov et al., *Nucl. Phys.* A**460** (1986) 352

[Bet30] H. Bethe, *Ann. Physik* **5** (1930) 325. *Z. Phys.* **76** (1932) 293.

[Bia89] L. Bianchi et al., *Nucl. Instr. and Meth.* A**276** (1989) 509.

[Bla04] G. Blanchon, A. Bonaccorso, and N. Vinh Mau, *Nucl. Phys.* A**739** (2004) 259.

[Bla05] B. Blank et al., *Phys. Rev. Lett.* **94**(2005) 232501.

[Blo33] F. Bloch, *Ann. Physik* **16** (1933) 285. *Z. Phys.* **81** (1933) 363.

[Boh01] H.G. Bohlen et al., *Phys. Rev.* C**64** (2001) 024312

[Bou01] A. Boujrad and F. Saillant, *2000 IEEE Nuclear Science Symposium Conference Record* (2001) 12-192

[Bre36] G. Breit and E. Wigner, *Phys. Rev.* **49** (1936) 519

[D'Ag95] G. D'Agostini, *Probability and Measurement Uncertainty in Physics* arXiv:hep-ph/9512295 v2 (1995).

[Dem03] C.E. Demonchy, *Thesis T0306* Université de Caen (2003).

[Des01] P. Descouvemont and A. Kharbach, *Phys. Rev.* C**63**(2001) 027001.

[Dob83] A.V. Dobrovolsky et al., *Nucl. Phys.* B**214** (1983) 1.

[Eks99] L.P. Ekstrm and R.B. Firestone, *WWW Table of Radioactive Isotopes* database version 2/28/99 from URL http://ie.lbl.gov/toi/index.htm

[End81] I. Endo, et al., *Nucl. Instr. and Meth.* **188** (1981) 51.

[Fes58] H. Feshbach, *Ann. Phys.* **5** (1958) 357. *Ann. Phys.* **19** (1962) 287. (as cited in [Tho06])

[Fes74] H. Feshbach, *Theoretical Nuclear Physics* John Wiley & Sons Inc (1974) 242.

[Fri89] O. Frisch, *British Atomic Energy Report* **BR-49** (1989).

[Gan02] P. Gangnant et al., *Report Ganil* **27-2002**(2002)

[Gan05] http://www.ganil.fr

[Gol03] M.S. Golovkov et al., *Phys. Lett.* B**566** (2003) 70.

[Gol04a] M.S. Golovkov et al., *Phys. Lett.* B**588** (2004) 163.

[Gol04b] M.S. Golovkov et al., *Phys. Rev. Lett.* **93** (2004) 262501.

[Gol05] M.S. Golovkov, *Phys. Rev.* c**72** (2005) 064612

[Gor03] M.G. Gornov et al., *JETP Lett.* **77**(2003) 344.

[Gui84] D. Guillemaud-Müller et al., *Nucl. Phys.* A**426**(1984) 37.

[Hal04] D. Halderson, *Phys. Rev.* C**70** (2004) 041603(R)

[Han87] P.G. Hansen and B. Jonson, *Europhys. Lett.* B**160**(1987) 409.

[Iwa00] H. Iwasaki et al., *Phys. Lett.* B**481**(2000) 7. *Phys. Lett.* B**491**(2000) 8.

[Jac03] B. Jacquot, *Accelerator tour for users* (2003) from URL http://www.ganil.fr/operation/diaporamas/physicist/index.htm

[Kno89] G.F. Knoll, *Radiation detection and measurement* ed. J. Wiley and sons, Inc. (1989) Scintillation detector principles 215

[Kor01] A.A. Korsheninnikov et al., *Phys. Rev. Lett.* **87**(2001) 092501.

[Kor03] A.A. Korsheninnikov et al., *Phys. Rev. Lett.* **90** (2003) 082501.

[Kor05] A.A. Korsheninnikov, *Nucl. Phys.* A**751**(2005) 501c.

[Lan58] A.M. Lane & R.G. Thomas, *Rev. Mod. Phys.* **30** (1958) 257. (as cited in [Tho06])

[Lau95] K. Lau and J. Pyrlik, *Nucl. Instr. and Meth.* A**366** (1995) 298.

[Mar02] F. M. Marqués et al., *Phys. Rev.* C**65** (2002) 044006.

[Mei03a] M. Meister et al., *Phys. Rev. Lett.* **91** (2003) 162504.

[Mei03b] M. Meister et al., *Nucl. Phys.* A**723**(2003) 13.

[Mer86] T. Mertelmeier and H.M. Hofmann, *Nucl. Phys.* A**459** (1986) 387.

[Mey79] T.S. Meyer, *Nucl. Phys.* A**324**(1979) 335.

[Mit03] W. Mittig et al., *Nucl. Phys.* A**722** (2003) 10c.

[Miz99] Y. Mizoi et al., *Nucl. Instr. and Meth.* A**431** (1999) 112.

[Odl96] O.H. Odland et al., *Nucl. Instr. and Meth.* A**378** (1996) 149.

[Nav02] P. Navrátil and W. E. Ormand, *Phys. Rev.* C**88** (2002) 152502.

[Ono92] A. Ono et al., *Prog. Theor. Phys.* **87** (1992) 1185.

[Ots01] T. Otsuka et al., *Phys. Rev. Lett.* **87** (2001) 082502.

[Pan76] J.A. Panitz and J.A. Foerch, *Rev. Sci. Instr.* **47** (1976) 44.

[Par90] B. Parker et al., *Phys. Lett.* B**251**(1990) 483.

[Par02] M. Pârlog et al., *Nucl. Instr. and Meth.* A**482** (2002) 674.

[Pei84] A. Peisert and F. Sauli, *Drift and diffusion of electrons in gases: a compilation* CERN/84-08 (1984)

[Pie03] S. C. Pieper, *Phys. Rev. Lett.* **90** (2003) 252501.

[Rei70] I. Reichstein and Y.C. Tang, *Nucl. Phys.* A**158** (1970) 529.

[Rup05] G. Ruprecht et al., *Status of the TRIUMF Annular Chamber for the Tracking and Identification of Charge Partcles (TACTIC)* Submitted to *Eur. Phys. Jour.*

[Sak99] H. Sakurai et al., *Phys. Lett.* B**448**(1999) 180.

[San94] J.C. Santiard et al., *GASSIPLEX, a low noise analog signal processor for readout of gaseous detectors* CERN-ECP/94-17 (1994)

[Sat83] G.R. Satchler, *Direct Nuclear Reactions* Oxford University Press (1983)

[Sid03] S.I. Sidorchuk et al., *Nucl. Phys.* A**719**(2003) 229c.

[Sid04] S.I. Sidorchuk et al., *Phys. Lett.* B**594**(2004) 54.

[Sri05] J. F. Ziegler, http://www.srim.org

[Ste04] S.V. Stepantsov et al., *Nucl. Phys.* A**738**(2004) 436.

[Sto66] R.H. Stokes et al., *Bull. Amer. Phys. Soc.* **11**(1966) 9.

[Tal60] I. Talmi and I. Unna, *Phys. Rev. Lett.* **4**(1960) 469.

[Tan85] I. Tanihata et al., *Phys. Rev. Lett.* **55**(1985) 2676.

[Tho77] D.R. Thompson, M. LeMere, and Y.C. Tang, *Nucl. Phys.* A**286** (1977) 53.

[Tho06] I.J. Thompson, http://www.fresco.org.uk (2006)
Scattering, ed. E.R. Pike and P.C. Sabatier, Academic Press (2001) Methods of Direct Reaction Theories 1360-1372.
Computer Physics Reports **7** (1988) Coupled Channels Methods for Nuclear Physics 167-212.

[Til92] D.R. Tilley et al., *Nucl. Phys.* A**541**(1992) 1.

[Til02] D.R. Tilley et al., *Nucl. Phys.* A**708**(2002) 3.

[Tim02] N.K. Timofeyuk, *Phys. Rev.* C**65** (2002) 064306.

[Tim04] N.K. Timofeyuk, *Phys. Rev.* C**69** (2004) 034336.

[Tri05] http://www.triumf.info/public/

[Ven91] R. Veenhof, *CERN Programme Library* W5050. (1991) http://garfield.web.cern.ch/garfield

[Vil95] A.C.C. Villari et al., *Nucl. Phys.* A**588** (1995) 267c.

[Viy79] Y.P. Viyogi et al., *Phys. Rev. Lett.* **42** (1979) 33.

[Vol65] A.B. Volkov, *Nucl. Phys.* **74** (1965) 33.

[Wap03] A.H. Wapstra and C. Thibault, *Nucl. Phys.* A**729** (2003) 337.

[Wes79] G.D. Westfall et al., *Phys. Rev. Lett.* **43** (1979) 1859.

[Wur97] J. Wurzer and H. M. Hofmann, *Phys. Rev.* C**55** (1997) 688

[Yam79] N. Yamaguchi et al., *Prog. Theor. Phys.* **62** (1979) 1018.

[You68] P.G. Young et al., *Phys. Rev.* **173**(1968) 949.

[Zie99] J.F. Ziegler, *J. Appl. Phys./Rev. App. Phys.* **85** (1999) 1249.

[Zhu93] M.V. Zhukov et al., *Phys. Rep.* **231**(1993) 151.

Acknowledgements

Intro

So this is it, the end of four long years. Fighting with cables and numbers, hoping to see something at the end, and fearing to spend such a long time in an nonexistent physical being.

Of course, this was not a one-man task. Many people have contributed for having a positive result and, eventually they have helped me to extract a doctor out of myself. At this point it is worth[1] remarking everyone's help.

It is expected that one should be able to recognise all these contributions in their actual size and communicate them in an 'Acknowledgements' chapter. But how to measure the acknowledgement level? Normally the gratitude increases with the number of fruitful and appreciable actions, N. Since not all positive actions deserve the same level of gratitude, we can split the total number into additions of different types, N_i, weighted by different factors, μ_i, for each kind of action. Then the total number of appreciable actions results in:

$$N = \sum \mu_i N_i \tag{D.1}$$

Probably everybody has already realised that the relation between the gratitude and the number N_t is not linear. It is common to appreciate much more the initial actions than when an important amount begins to be accumulated. At some point the level of gratitude approximates a maximum that is never reached[2]. As a first approximation we can model this behaviour of gratitude, $\mathscr{G}$, as:

[1] and a question of justice

[2] at least, in the usual every-day life, we are not talking about life-or-death situations

$$\mathscr{G} \approx 1 - \exp\left(-N\right) \tag{D.2}$$

Within another description we can separate those contributions strictly related with the work, T_G, from those with a more personal-support meaning, P_G:

$$\mathscr{G} \approx 1 - \exp\left[-(N^T + N^P)\right] \tag{D.3}$$

The gratitude should not depend only on the number of actions since not all the people are in the same situation for performing these actions. We need to take into account that people with great responsibilities within the job of each case perform appreciable actions in a natural way, then $\mathscr{G}$ should be boosted for those far for those actions far from responsibilities. Another factor that may help to increase N is the interaction time. It is expected that N grows naturally with time, so high N's in short times need to be highlighted. In order to evaluate the level of gratitude we can define the quantity *Acknowledgement*, $\mathscr{A}$, as:

$$\mathscr{A} = \int \left(\frac{\partial \mathscr{G}}{\partial t} - \frac{\partial \mathscr{G}}{\partial R} \right) \mathrm{d}t \tag{D.4}$$

where t is the interaction time and $R(t)$ the level of responsibility in each time[3]. At this point it is worthy to notice that $N^T = f(t, R)$ but $N^P = f(t)$.

Formula D.4 allow us to distinguish three different cases. Assuming that both partials are positive we may have:

- $\mathscr{A} > 0$ for those cases where positive actions exceed responsibility
- $\mathscr{A} = 0$ with two different cases:
  - $\partial_t, \partial_R > 0$ positive actions balance with responsibility[4]
  - $\partial_t, \partial_R = 0$ where absence of positive actions appears along absence of responsibility
- $\mathscr{A} < 0$ for those cases where the existence of certain responsibility lacks for positive actions

[3] notice that $\mathscr{G}$ is an always-rising function and therefore its partials are usually positive, except in those extraordinary cases where N is negative

[4] corresponding to the most expectable situation

Strategy

Then, at this step, is where the different strategies appear. A quite straight-forward way is the usual all-names list with a funny or respectable[5] sentence. Within this approach one can include different appreciations of people smoothing the differences among them, and resulting in a quite polite and politically correct solution. Another characteristic of this approach consists in the absorption of the whole responsibility and consequences by the author in recognising the contributions[6].

Another approach may consist in leaving the task of classify the contributions to the readers. This interactive way helps to reveal more clearly the disposition of each reader to recognise himself in the acknowledgements[7], being closer to the truth of his actions without a public access to this information. In such approximation, the responsibility of the author is to give enough information for making an accurate classification[8].

Let me make something in the middle. There it goes.

The history so far

Every history has a background in some way. That for this one is placed in the Universidade de Santiago, in the group GENP[9], where Nacho, Pepe and Lola drive the future of young students. After finishing a diploma thesis with Dolores Cortina (Lola, from now on) she told me about an opportunity to work at GANIL with a new device called MAYA and to build a thesis around. And so we did.

During April 2002 I arrived for the first time at GANIL. There I started to realise about the enormous love french people has to their language, and their sense of social behaviour. The very first people I met at GANIL were Patricia and Charled. Afterwards Herve and Wolfi appeared.

Those first days where related with the experiment for the thesis of Charled, in addition to the construction of MAYA with Wolfi, so we worked together while I was learning about the detector. He also helped me to pass my days in Caen with

[5] depending on the personal relation

[6] which is, probably, the reason for the politically correct form at the end

[7] gnostic te autvn

[8] but this is neither an easy task, it depends on the author filters, nobody's perfect and this is a joke

[9] Grupo Experimental de Núcleos y Partículas

long conversations. The guidelines and support of my activity there were nicely covered by Herve as my official supervisor[10]. So we did the experiment of Charled, I borrowed some data, and once in Santiago Lola and me played a little with those number to be ready for the big moment.

The big moment was born from the idea of Herve to detect ^{7}H with MAYA. When the time has come we discussed with Wolfi on how we can perform the experiment, and once we have a plan we start to mount the experimental setup. Those were two months of living in the experimental cave fighting with cables, electronics, stealing modules, and asking once and back again for the help of the technicians to fix those things we had broken or misconfigured. Herve, Maurycy and myself proved once again that nothing works until 2 μs before the experiment begins.

And the experiment begun. And almost at the same time it ended. We accumulate a good number of mistakes that along the failure in delivering the ^{8}He beam forced us to think in a later attempt. We received support from many people[11] during this first time and in the sequel. I can remember[12] Bea, Bea, Belén, Fanny, Alain, Alexandre, Oleg, Roi, Marielle and also Antonio, apart, of course, the technical help from Jean-Francoise and Patrice[13].

The sequel was performed some months after, and at that time everything was right thanks to what we learnt and, more in particular, to those Gardfield simulations made by Oleg. I passed more funny days at GANIL, when even with the good company of Bea and Charled I received nice names as "Pitufo gruñón" or even "Hitler" for those people supporting my bad mood. Finally we stored THE data and I came back to Santiago. And the time for analysis begun.

That was a hard time. Extracting results from a new detector in an experiment with non-standard techniques needed the development of new methods. From time to time I needed support to front the possibility of a complete failure of the analysis. The optimistic point of view of Lola used to balance my "por qué es todo tan difícil?"[14]. And with help from people like Carlos and Quique everything was smoother.

At this point I have to mention those people that supported me from the beginning to the end, with a big zero in their ∂_R partial. In the case of my father it was even before the beginning, and probably it will never reach an end. It would be also impossible to describe the support from Tona in less than ten times the size of this

[10] and usually finding tons of money for paying my stays!
[11] even if not everybody was convinced that ^{7}H will appear at the end
[12] in no particular order
[13] i still owe you those 40 cents for the stopper
[14] why is it everything so difficult?

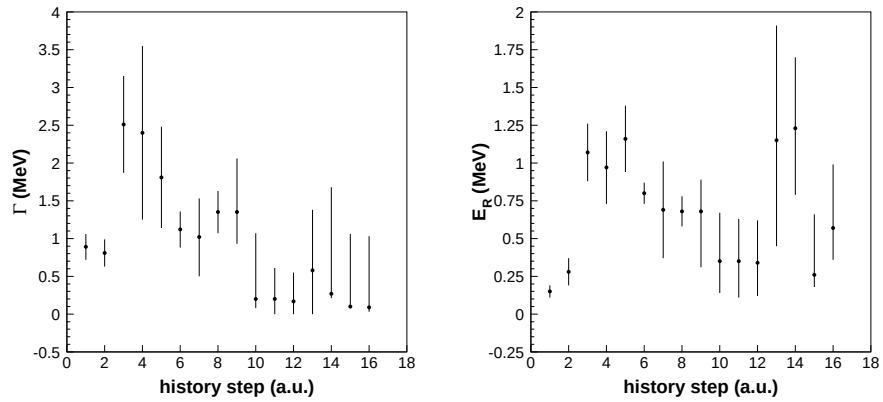

Figure D.1: *Evolution of* Γ *(left panel) and* E_R *(right panel) throughout the analysis. The history steps are arbitrary units corresponding to changes and corrections during the analysis.*

thesis so I'm still writing that volume for her. The situation is quite close with Javi, both of who have to listen hours and hours of something that they do not care at all, but they did. A couple of points of support, Edu and Jorge, were interrupted by those stupid jokes of life, becoming intermittent[15] but still necessary, let's see what will follow[16]. And with Noe the stupid joke of life was my fault.

But life went on, and so the analysis. Long, long, very long discussions were needed, and they saved the process many times. Critical points appear with the discussions with Nacho[17], who saved the analysis a couple of times, with Diego, who saved it at least three times, and with Wolfi, who... buf, whatever... at some point I ask myself what the hell was my contribution. Of course, from time to time visits to GANIL, where the extraordinary comprehension of Sophie helped me to overcome the different problems associated with any visit, allowed me to exchange impressions with Herve, until he left to Vancouver[18], while Wolfi left to Japan. And if that was not enough, Lola needed to stretch time due to something Pepe did[19].

Once we had results (see Figure D.1 for a graphical view of their evolution) there were a couple of main tasks: Writing the associated papers, and writing the associated thesis. The papers were (are) being written with many inputs from the people involved in the experiment, and discussed among Lola, Wolfi, Patricia

[15] one more than the other, it is impressive what the Atlantic Ocean can influence the Internet communications

[16] at this moment Edu is still bringing creativeness to life for me

[17] from 22:00 h and on

[18] again, the effect of the Atlantic Ocean on communications appeared

[19] later he was called Marcos

and me, who, in addition, put their experience in publishing. The natural end arrived with the thesis manuscript. All my long, complex and subordinate sentences in passive subject and impossible-to-understand explanations were normalized and translated for the rest of the world thanks to the filtering by Lola (and further corrected by Herve). And also the presentations, including the thesis, were smoothed by her advices.

The last chapter started with the selection of the jury for the defense of the thesis. I was privileged with the assistance of Pierre, Ismael and Wilton along with Nacho and Wolfi[20] as the president (of course). I was gifted with interesting questions and remarks, and even memorable "dylanesque" quotes[21]. And this last chapter ended with their approval[22].

And also every history has a foreground in some way. This is, again, GANIL. Fanny kindly accepted to be my boss in the next two years.

That was nearly all. Some things remain unfinished, but that is another history.

Finally, if you cannot find yourself in this chapter it is possibly because of two main reasons: Either I have forgotten you[23], or both of your partials in Formula D.4 were null. Feel free to choose the reason you are more comfortable with.

[20] directly from Japan
[21] See Chapter 4
[22] and a bottle of sake, directly from Japan
[23] then please accept my regrets